Time of Flight Cameras: Principles, Methods, and Applications

Miles Hansard, Seungkyu Lee, Ouk Choi, Radu Horaud

▶ To cite this version:

HAL Id: hal-00725654
https://inria.hal.science/hal-00725654

Miles Hansard · Seungkyu Lee
Ouk Choi · Radu Horaud

Time-of-Flight Cameras

Principles, Methods and Applications

Springer

Miles Hansard
Seungkyu Lee
Ouk Choi
Radu Horaud

Time-of-Flight Cameras: Principles, Methods and Applications

Acknowledgements

Contents

Chapter 1
Characterization of Time-of-Flight Data

Abstract This chapter introduces the principles and difficulties of time-of-flight depth measurement. The depth-images that are produced by time-of-flight cameras suffer from characteristic problems, which are divided into the following two classes. Firstly there are systematic errors, such as noise and ambiguity, which are directly related to the sensor. Secondly, there are non-systematic errors, such as scattering and motion blur, which are more strongly related to the scene-content. It is shown that these errors are often quite different from those observed in ordinary color images. The case of motion blur, which is particularly problematic, is examined in detail. A practical methodology for investigating the performance of depth-cameras is presented. Time-of-flight devices are compared to structured-light systems, and the problems posed by specular and translucent materials are investigated.

1.1 Introduction

Time-of-Flight (ToF) cameras produce a *depth image*, each pixel of which encodes the distance to the corresponding point in the scene. These cameras can be used to estimate 3D structure directly, without the help of traditional computer-vision algorithms. There are many practical applications for this new sensing modality, including robot navigation [119, 98, 82], 3D reconstruction [57] and human-machine interaction [32, 107]. ToF cameras work by measuring the phase-delay of reflected infrared (IR) light. This is not the only way to estimate depth; for example, an IR *structured-light* pattern can be projected onto the scene, in order to facilitate visual triangulation [106]. Devices of this type, such as the Kinect [39], share many applications with ToF cameras [88, 105, 90, 28, 97].

The unique sensing architecture of the ToF camera means that a raw depth image contains both systematic and non-systematic bias that has to be resolved for robust depth imaging [37]. Specifically, there are problems of low depth precision and low spatial resolution, as well as errors caused by radiometric, geometric and illumina-

tion variations. For example, measurement accuracy is limited by the power of the emitted IR signal, which is usually rather low compared to daylight, such that the latter contaminates the reflected signal. The amplitude of the reflected IR also varies according to the material and color of the object surface.

Another critical problem with ToF depth images is *motion blur*, caused by either camera or object motion. The motion blur of ToF data shows unique characteristics, compared to that of conventional color cameras. Both the depth accuracy and the frame rate are limited by the required integration time of the depth camera. Longer integration time usually allows higher accuracy of depth measurement. For static objects, we may therefore want to decrease the frame rate in order to obtain higher measurement accuracies from longer integration times. On the other hand, capturing a moving object at fixed frame rate imposes a limit on the integration time.

In this chapter, we discuss depth-image noise and error sources, and perform a comparative analysis of ToF and structured-light systems. Firstly, the ToF depth-measurement principle will be reviewed.

1.2 Principles of Depth Measurement

Figure 1.1 illustrates the principle of ToF depth sensing. An IR wave indicated in red is directed to the target object, and the sensor detects the reflected IR component. By measuring the phase difference between the radiated and reflected IR waves, we can calculate the distance to the object. The phase difference is calculated from the relation between four different electric charge values as shown in fig. 1.2. The four
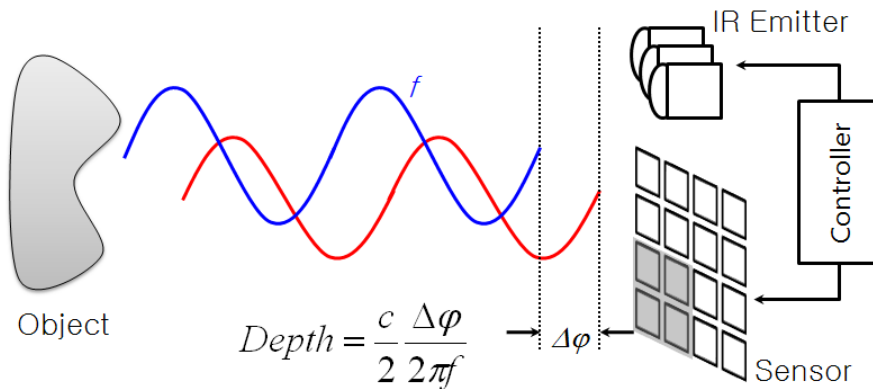
Fig. 1.1 The principle of ToF depth camera [37, 71, 67]: The phase delay between emitted and reflected IR signals are measured to calculate the distance from each sensor pixel to target objects.

phase control signals have 90 degree phase delays from each other. They determine the collection of electrons from the accepted IR. The four resulting electric charge

values are used to estimate the phase-difference t_d as

$$t_d = \arctan\left(\frac{Q_3 - Q_4}{Q_1 - Q_2}\right) \tag{1.1}$$

where Q_1 to Q_4 represent the amount of electric charge for the control signals C_1 to C_4 respectively [37, 71, 67]. The corresponding distance d can then be calculated, using c the speed of light and f the signal frequency:

$$d = \frac{c}{2f}\frac{t_d}{2\pi}. \tag{1.2}$$

Here the quantity $c/(2f)$ is the maximum distance that can be measured without ambiguity, as will be explained in chapter 2.
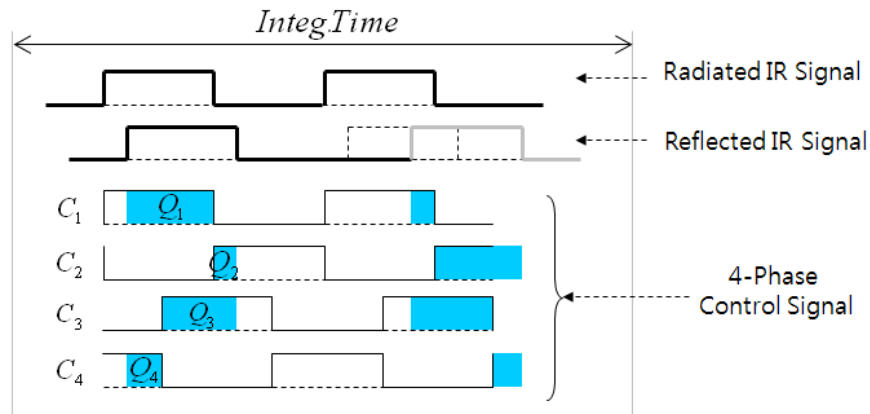
Fig. 1.2 Depth can be calculated by measuring the phase delay between radiated and reflected IR signals. The quantities Q_1 to Q_4 represent the amount of electric charge for control signals C_1 to C_4 respectively.

1.3 Depth Image Enhancement

This section describes the characteristic sources of error in ToF imaging. Some methods for reducing these errors are discussed. The case of motion blur, which is particularly problematic, is considered in detail.

1.3.1 Systematic Depth Error

From the principle and architecture of TOF sensing, depth cameras suffer from several systematic errors such as IR demodulation error, integration time error, amplitude ambiguity and temperature error [37]. As shown in fig. 1.3 (a), longer integration increases signal to noise ratio, which, however, is also related to the frame rate. Figure 1.3 (b) shows that the amplitude of the reflected IR signal varies according to the color of the target object as well as the distance from the camera. The ambiguity of IR amplitude introduces noise into the depth calculation.
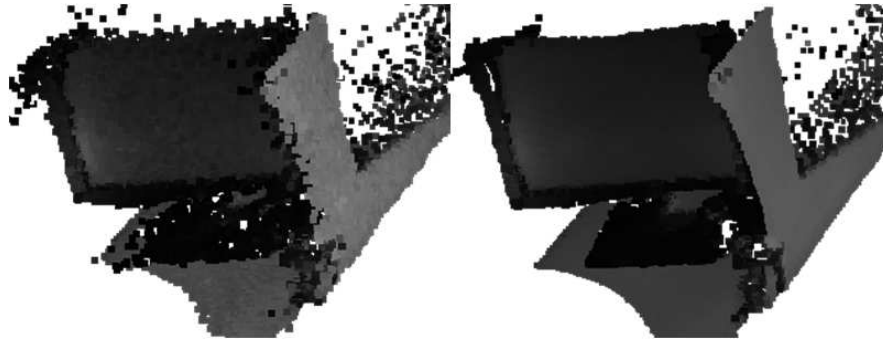
(a) Integration Time Error: Longer integration time shows higher depth accuracy (right) than shorter integration time (left).

(b) IR Amplitude Error: 3D points of the same depth (chessboard on the left) show different IR amplitudes (chessboard on the right) according to the color of the target object.

Fig. 1.3 Systematic noise and error: These errors come from the TOF principle of depth measurement.

1.3.2 Non-Systematic Depth Error

Light scattering [86] gives rise to artifacts in the depth image, due to the low sensitivity of the device. As shown in fig. 1.4 (a), close objects (causing IR saturation) in the lower-right part of the depth image introduce depth distortion in other regions, as indicated by dashed circles. Multipath error [41] occurs when a depth calculation in a sensor pixel is an superposition of multiple reflected IR signals. This effect becomes serious around the concave corner region as shown in fig. 1.4 (b). Object boundary ambiguity [95] becomes serious when we want to reconstruct a 3D scene based on the depth image. Depth pixels near boundaries fall in between foreground and background, giving rise to 3D structure distortion.

1.3.3 Motion Blur

Motion blur, caused by camera or target object motions, is a critical error source for on-line 3D capturing and reconstruction with ToF cameras. Because the 3D depth measurement is used to reconstruct the 3D geometry of scene, blurred regions in a depth image lead to serious distortions in the subsequent 3D reconstruction. In this section, we study the theory of ToF depth sensors and analyze how motion blur occurs, and what it looks like. Due the its unique sensing architecture, motion blur in the ToF depth camera is quite different from that of color cameras, which means that existing deblurring methods are inapplicable.

The motion blur observed in a depth image has a different appearance from that in a color image. Color motion blur shows smooth color transitions between foreground and background regions [109, 115, 121]. On the other hand, depth motion blur tends to present overshoot or undershoot in depth-transition regions. This is due to the different sensing architecture in ToF cameras, as opposed to conventional color cameras. The ToF depth camera emits an IR signal of a specific frequency, and measures the phase difference between the emitted and reflected IR signals to obtain the depth from the camera to objects. While calculating the depth value from the IR measurements, we need to perform a non-linear transformation. Due to this architectural difference, the smooth error in phase measurement can cause uneven error terms, such as overshoot or undershoot. As a result, such an architectural difference between depth and color cameras makes the previous color image deblurring algorithms inapplicable to depth images.

Special cases of this problem have been studied elsewhere. Hussmann et al. [61] introduce a motion blur detection technique on a conveyor belt, in the presence of a single directional motion. Lottner et al. [79] propose an internal sensor control-signal based blur detection method that is not appropriate in general settings. Lindner et al. [76] model the ToF motion blur in the depth image, to compensate for the artifact. However, they introduce a simple blur case without considering the ToF principle of depth sensing. Lee et al. [73, 74] examine the principle of ToF depth blur artifacts, and propose systematic blur-detection and deblurring methods.
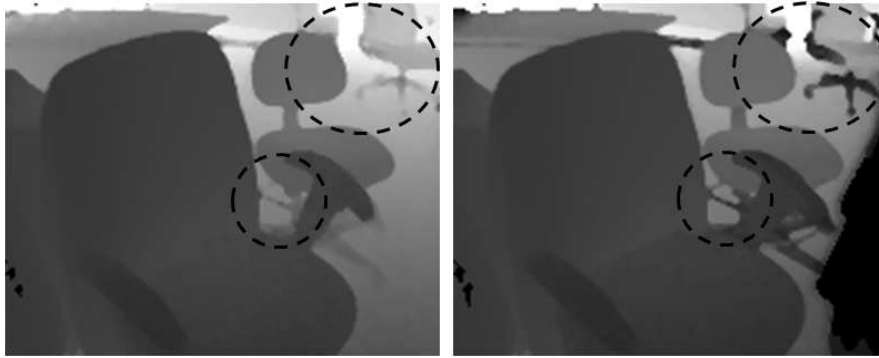
(a) Light Scattering: IR saturation in the lower-right part of the depth image causes depth distortion in other parts, as indicated by dashed circles.
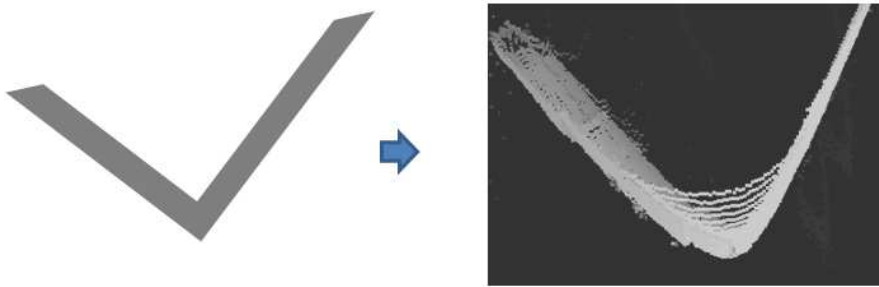
(b) Multipath Error: The region inside the concave corner is affected, and shows distorted depth measurements.
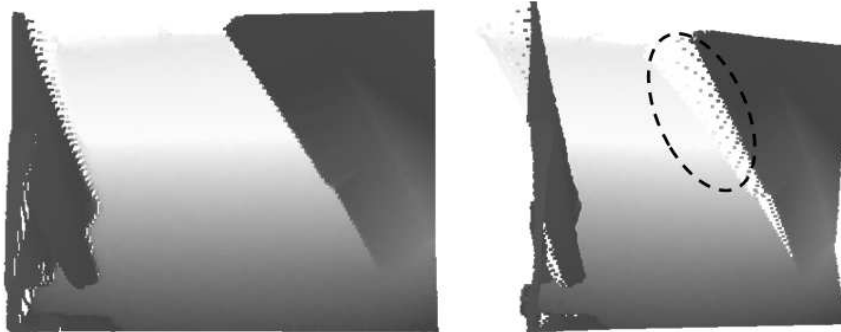
(c) Object Boundary Ambiguity: Several depth points on an object boundary are located in between foreground and background, resulting in 3D structure distortion.

Fig. 1.4 Non-systematic noise and error: Based on the depth-sensing principle, scene-structure may cause characteristic errors.

Based on the depth sensing principle, we will investigate how motion blur occurs, and what are its characteristics. Let's assume that any motion from camera

or object occurs during the integration time, which changes the phase difference of the reflected IR as indicated by the gray color in fig. 1.2. In order to collect enough electric charge Q_1 to Q_4 to calculate depth (1.1), we have to maintain a sufficient integration time. According to the architecture type, integration time can vary, but the integration time is the major portion of the processing time. Suppose that n cycles are used for the depth calculation. In general, we repeat the calculation n times during the integration time to increase the signal-to-noise ratio, and so

$$t_d = \arctan\left(\frac{nQ_3 - nQ_4}{nQ_1 - nQ_2}\right) \tag{1.3}$$

where Q_1 to Q_4 represent the amount of electric charge for the control signals C_1 to C_4 respectively (cf. eqn. 1.1 and fig. 1.2). The depth calculation formulation 1.3 ex-
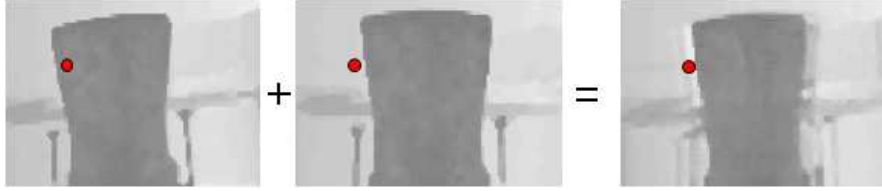
Fig. 1.5 ToF depth motion-blur due to movement of the target object.

pects that the reflected IR during the integration time comes from a single 3D point of the scene. However, if there is any camera or object motion during the integration time, the calculated depth will be corrupted. Figure 1.5 shows an example of this situation. The red dot represents a sensor pixel of the same location. Due the the motion of the chair, the red dot sees both foreground and background sequentially within its integration time, causing a false depth calculation as shown in the third image in fig. 1.5. The spatial collection of these false-depth points looks like blur around moving object boundaries, where significant depth changes are present.

Figure 1.6 illustrates what occurs at motion blur pixels in the '2-tab' architecture, where only two electric charge values are available. In other words, only $Q_1 - Q_2$ and $Q_3 - Q_4$ values are stored, instead of all separate Q values. Figure 1.6 (a) is the case where no motion blur occurs. In the plot of $Q_1 - Q_2$ versus $Q_3 - Q_4$ in the third column, all possible regular depth values are indicated by blue points, making a diamond shape. If there is a point deviating from it, as an example shown in fig. 1.6 (b), it means that their is a problem in between the charge values Q_1 to Q_4. As we already explained in fig. 1.2, this happens when there exist multiple reflected signals with different phase values. Let's assume that a new reflected signal, of a different phase value, comes in from the mth cycle out of a total of n cycles during the first half *or* second half of the integration time. A new depth is then obtained as

$$t_d(m) = \arctan\left(\frac{n\hat{Q}_3 - n\hat{Q}_4}{(mQ_1 + (n-m)\hat{Q}_1) - (mQ_2 + (n-m)\hat{Q}_2)}\right) \tag{1.4}$$

$$t_d = \arctan\left(\frac{nQ_3 - nQ_4}{nQ_1 - nQ_2}\right)$$

(a)

$$t_d(m) = \arctan\left(\frac{n\hat{Q}_3 - n\hat{Q}_4}{(mQ_1 + (n-m)\hat{Q}_1) - (mQ_2 + (n-m)\hat{Q}_2)}\right)$$

(b)
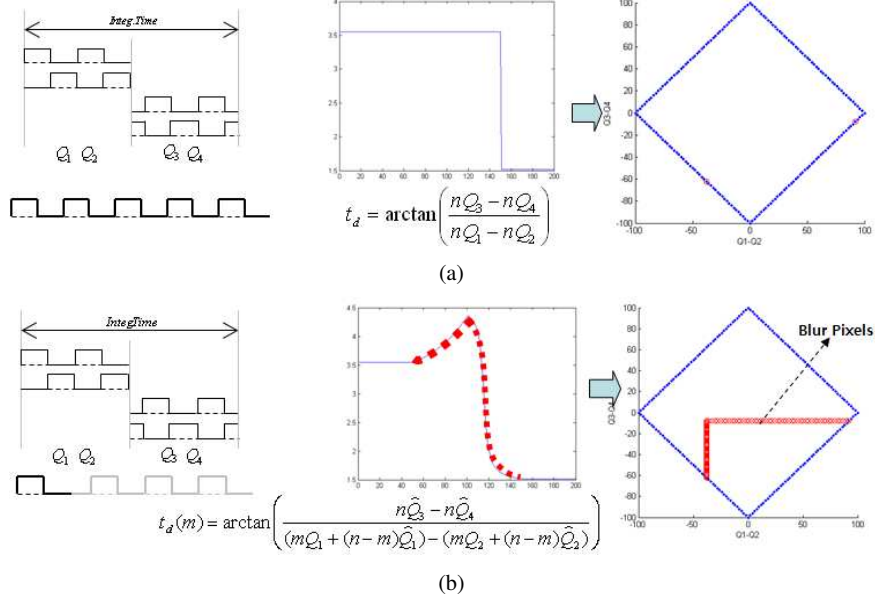
Fig. 1.6 ToF depth sensing and temporal integration.

$$t_d(m) = \arctan\left(\frac{(mQ_3 + (n-m)\hat{Q}_3) - (mQ_4 + (n-m)\hat{Q}_4)}{n\hat{Q}_1 - n\hat{Q}_2}\right) \qquad (1.5)$$

in the first or second-half of the integration time, respectively. Using the depth calculation formulation (eq 1.1), we simulate all possible blur models. Figure 1.7 illustrates several examples of depth images taken by ToF cameras, having depth value transitions in motion blur regions. Actual depth values along the blue and red cuts in each image are presented in the following plots. The motion blurs of depth images in the middle show unusual peaks (blue cut) which cannot be observed in conventional color motion blur. Figure 1.8 shows how motion blur appears in 2-tap case. In the second phase where control signals C_3 and C_4 collect electric charges, the reflected IR signal is a mixture of background and foreground. Unlike color motion blurs, depth motion blurs often show overshoot or undershoot in their transition between foreground and background regions. This means that motion blurs result in higher or lower calculated depth than all near foreground and background depth values, as demonstrated in fig. 1.9.

In order to verify this characteristic situation, we further investigate the depth calculation formulation in equation 1.5. Firstly we re-express equation 1.4 as

$$t_d(m) = \arctan\left(\frac{n\hat{Q}_3 - n\hat{Q}_4}{m(Q_1 - \hat{Q}_1 - Q_2 + \hat{Q}_2) + n(\hat{Q}_1 - \hat{Q}_2)}\right) \qquad (1.6)$$
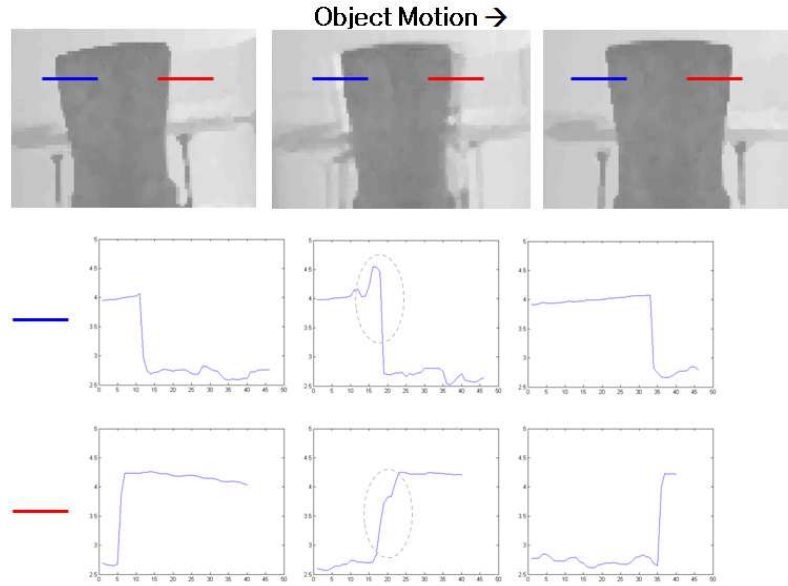
Fig. 1.7 Sample depth value transitions from depth motion blur images captured by an SR4000 TOF camera.
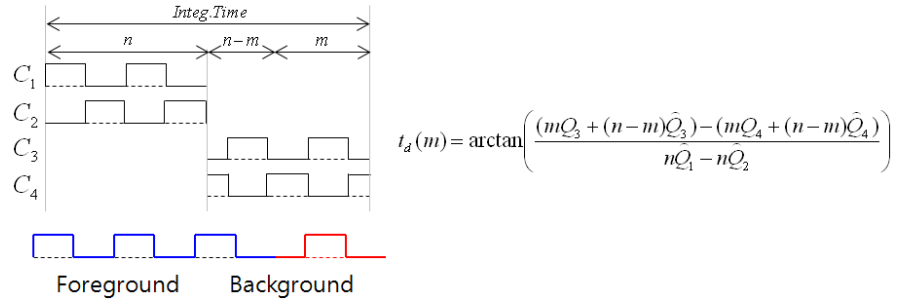
Fig. 1.8 Depth motion blur in 2-tap case.

The first derivative of the equation 1.6 is zero, meaning local maxima or local minima, under the following conditions:

$$t_d'(m) = \frac{1}{1 + \left(\frac{n\hat{Q}_3 - n\hat{Q}_4}{m(Q_1 - \hat{Q}_1 - Q_2 + \hat{Q}_2) + n(\hat{Q}_1 - \hat{Q}_2)} \right)^2} \tag{1.7}$$

$$= \frac{(m(Q_1 - \hat{Q}_1 - Q_2 + \hat{Q}_2) + n(\hat{Q}_1 - \hat{Q}_2))^2}{(n\hat{Q}_3 - n\hat{Q}_4)^2 + (m(Q_1 - \hat{Q}_1 - Q_2 + \hat{Q}_2) + n(\hat{Q}_1 - \hat{Q}_2))^2} = 0$$
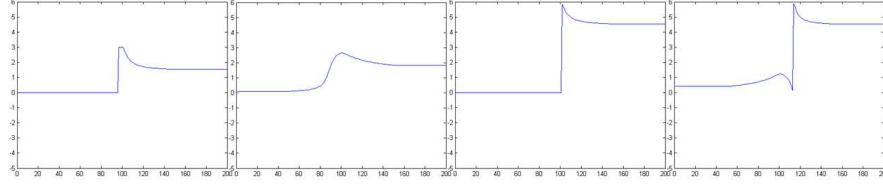
Fig. 1.9 TOF depth motion blur simulation results.

$$m = n\frac{\hat{Q}_2 - \hat{Q}_1}{Q_1 - \hat{Q}_1 - Q_2 + \hat{Q}_2} = n\frac{1 - 2\hat{Q}_1}{2Q_1 - 2\hat{Q}_1} \tag{1.8}$$
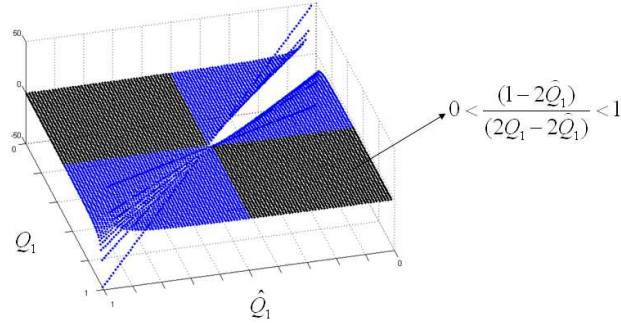
Fig. 1.10 Half of the all motion blur cases make local peaks.

Figure 1.10 shows that statistically half of all cases have overshoots or undershoots. In a similar manner, the motion blur model of 1-tap (eqn. 1.9) and 4-tap (eqn. 1.10) cases can be derived. Because a single memory is assigned for recording the electric charge value of four control signals, the 1-tap case has four different formulations upon each phase transition:

$$t_d(m) = \arctan\left(\frac{n\hat{Q}_3 - n\hat{Q}_4}{(mQ_1 + (n-m)\hat{Q}_1) - n\hat{Q}_2}\right)$$

$$t_d(m) = \arctan\left(\frac{n\hat{Q}_3 - n\hat{Q}_4}{nQ_1 - (mQ_2 + (n-m)\hat{Q}_2)}\right)$$

$$t_d(m) = \arctan\left(\frac{(mQ_3 + (n-m)\hat{Q}_3) - n\hat{Q}_4}{n\hat{Q}_1 - n\hat{Q}_2}\right)$$

$$t_d(m) = \arctan\left(\frac{nQ_3 - (mQ_4 + (n-m)\hat{Q}_4)}{n\hat{Q}_1 - n\hat{Q}_2}\right) \tag{1.9}$$

On the other hand, the 4-tap case only requires a single formulation, which is:

$$t_d(m) = \arctan\left(\frac{(mQ_3 + (n-m)\hat{Q}_3) - (mQ_4 + (n-m)\hat{Q}_4)}{(mQ_1 + (n-m)\hat{Q}_1) - (mQ_2 + (n-m)\hat{Q}_2)}\right) \tag{1.10}$$

Now, by investigating the relation between control signals, any corrupted depth easily can be identified. From the relation between Q_1 and Q_4, we find the following relation:

$$Q_1 + Q_2 = Q_3 + Q_4 = K. \tag{1.11}$$

Let's call this the *Plus Rule*, where K is the total amount of charged electrons. Another relation is the following formulation, called the *Minus Rule*:

$$|Q_1 - Q_2| + |Q_3 - Q_4| = K. \tag{1.12}$$

In fact, neither formulation exclusively represents motion blur. Any other event that can break the relation between the control signals, and can be detected by one of the rules, is an error which must be detected and corrected. We conclude that TOF motion blur can be detected by one or more of these rules.

(a) Depth images with motion blur

(b) Intensity images with detected motion blur regions (indicated by white color)
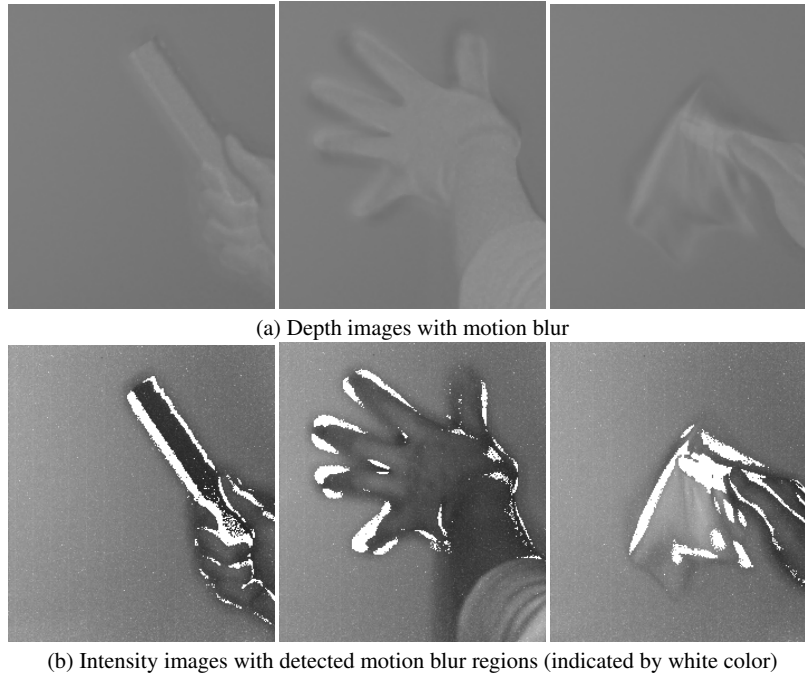
Fig. 1.11 Depth image motion blur detection results by the proposed method.

Figure 1.11 (a) shows depth image samples with motion blur artifacts due to various object motions such as rigid body, multiple body and deforming body motions respectively. Motion blur occurs not just around object boundaries; inside an object,

any depth differences that are observed within the integration time will also cause motion blur. Figure 1.11 (b) shows detected motion blur regions indicated by white color on respective depth and intensity images, by the method proposed in [73]. This is very straightforward but effective and fast method, which is fit for hardware implementation without any additional frame memory or processing time.

1.4 Evaluation of Time-of-Flight and Structured-Light Data

The enhancement of ToF and structured light (e.g. Kinect [106]) data is an important topic, owing to the physical limitations of these devices (as described in sec. 1.3). The characterization of depth-noise, in relation to the particular sensing architecture, is a major issue. This can be addressed using bilateral [118] or non-local [60] filters, or in wavelet-space [34], using prior knowledge of the spatial noise distribution. Temporal filtering [81] and video-based [28] methods have also been proposed.

The upsampling of low resolution depth images is another critical issue. One approach is to apply color super-resolution methods on ToF depth images directly [102]. Alternatively, a high resolution color image can be used as a reference for depth super-resolution [117, 3]. The denoising and upsampling problems can also be addressed together [15], and in conjunction with high-resolution monocular [90] or binocular [27] color images.

It is also important to consider the motion artifacts [79] and multipath [41] problems which are characteristic of ToF sensors. The related problem of ToF depth-confidence has been addressed using random-forest methods [95]. Other issues with ToF sensors include internal and external calibration [42, 77, 52], as well as range ambiguity [18]. In the case of Kinect, a unified framework of dense depth data extraction and 3D reconstruction has been proposed [88].

Despite the increasing interest in active depth-sensors, there are many unresolved issues regarding the data produced by these devices, as outlined above. Furthermore, the lack of any standardized data sets, with ground truth, makes it difficult to make quantitative comparisons between different algorithms.

The Middlebury stereo [99], multiview [103] and Stanford 3D scan [21] data set have been used for the evaluation of depth image denoising, upsampling and 3D reconstruction methods. However, these data sets do not provide real depth images taken by either ToF or structured-light depth sensors, and consist of illumination controlled diffuse material objects. While previous depth accuracy enhancement methods demonstrate their experimental results on their own data set, our understanding of the performance and limitations of existing algorithms will remain partial without any quantitative evaluation against a standard data set. This situation hinders the wider adoption and evolution of depth-sensor systems.

In this section, we propose a performance evaluation framework for both ToF and structured-light depth images, based on carefully collected depth-maps and their ground truth images. First, we build a standard depth data set; calibrated depth images captured by a ToF depth camera and a structured light system. Ground truth

depth is acquired from a commercial 3D scanner. The data set spans a wide range of objects, organized according to geometric complexity (from smooth to rough), as well as radiometric complexity (diffuse, specular, translucent and subsurface scattering). We analyze systematic and non-systematic error sources, including the accuracy and sensitivity with respect to material properties. We also compare the characteristics and performance of the two different types of depth sensors, based on extensive experiments and evaluations. Finally, to justify the usefulness of the data set, we use it to evaluate simple denoising, super-resolution and inpainting algorithms.

1.4.1 Depth Sensors

As described in section 1.2, the ToF depth sensor emits IR waves to target objects, and measures the phase delay of reflected IR waves at each sensor pixel, to calculate the distance travelled. According to the color, reflectivity and geometric structure of the target object, the reflected IR light shows amplitude and phase variations, causing depth errors. Moreover, the amount of IR is limited by the power consumption of the device, and therefore the reflected IR suffers from low signal-to-noise ratio (SNR). To increase the SNR, ToF sensors bind multiple sensor pixels to calculate a single depth pixel value, which decreases the effective image size. Structured light depth sensors project an IR pattern onto target objects, which provides a unique illumination code for each surface point observed at by a calibrated IR imaging sensor. Once the correspondence between IR projector and IR sensor is identified by stereo matching methods, the 3D position of each surface point can be calculated by triangulation.

In both sensor types, reflected IR is not a reliable cue for all surface materials. For example, specular materials cause mirror reflection, while translucent materials cause IR refraction. Global illumination also interferes with the IR sensing mechanism, because multiple reflections cannot be handled by either sensor type.

1.4.2 Standard Depth Data Set

A range of commercial ToF depth cameras have been launched in the market, such as PMD, PrimeSense, Fotonic, ZCam, SwissRanger, 3D MLI, and others. Kinect is the first widely successful commercial product to adopt the IR structured light principle. Among many possibilities, we specifically investigate two depth cameras: a ToF type SR4000 from MESA Imaging [80], and a structured light type Microsoft Kinect [105]. We select these two cameras to represent each sensor since they are the most popular depth cameras in the research community, accessible in the market and reliable in performance.

Heterogeneous Camera Set

We collect the depth maps of various real objects using the SR4000 and Kinect sensors. To obtain the ground truth depth information, we use a commercial 3D scanning device. As shown in fig. 1.12, we place the camera set approximately 1.2 meters away from the object of interest. The wall behind the object is located about 1.5 meters away from the camera set. The specification of each device is as follows.
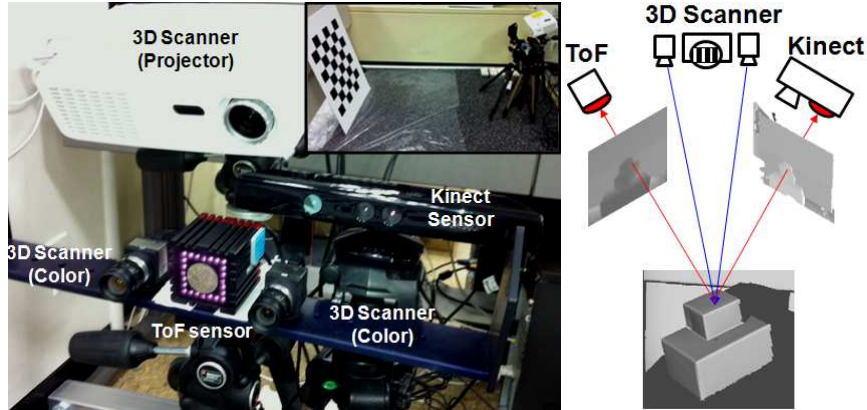
Fig. 1.12 Heterogeneous camera setup for depth sensing.

Mesa SR4000. This is a TOF type depth sensor producing a depth map and amplitude image at the resolution of 176×144 with 16 bit floating-point precision. The amplitude image contains the reflected IR light corresponding to the depth map. In addition to the depth map, it provides $\{x, y, z\}$ coordinates, which correspond to each pixel in the depth map. The operating range of the SR4000 is 0.8 meters to 10.0 meters, depending on the modulation frequency. The field of view (FOV) of this device is 43×34 degrees.

Kinect. This is a structured IR light type depth sensor, composed of an IR emitter, IR sensor and color sensor, providing the IR amplitude image, the depth map and the color image at the resolution of 640×480 (maximum resolution for amplitude and depth image) or 1600×1200 (maximum resolution for RGB image). The operating range is between 0.8 meters to 3.5 meters, the spatial resolution is 3mm at 2 meters distance, and the depth resolution is 10mm at 2 meters distance. The FOV is 57×43 degrees.

FlexScan3D. We use a structured light 3D scanning system for obtaining ground truth depth. It consists of an LCD projector and two color cameras. The LCD projector illuminates coded pattern at 1024×768 resolution, and each color camera records the illuminated object at 2560×1920 resolution.

Capturing Procedure for Test Images

(a) GTD (b) ToFD (c) SLD

(d) Object (e) ToFI (f) SLC
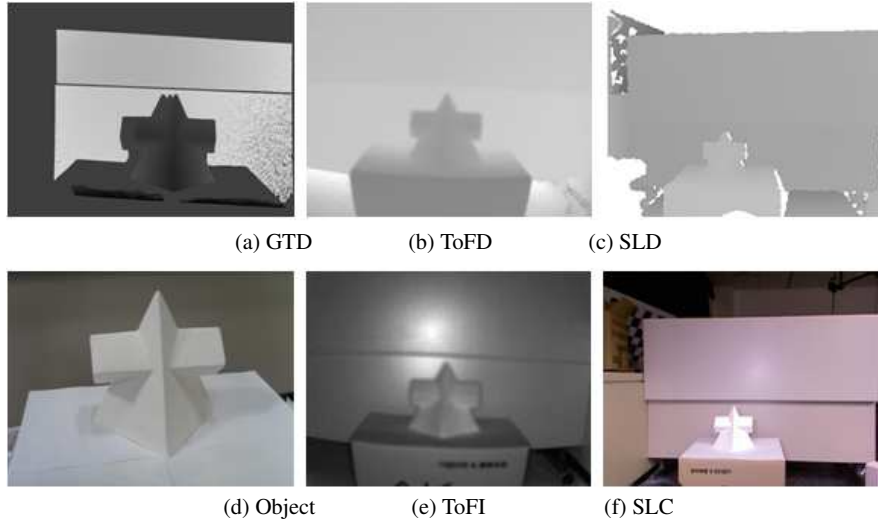
Fig. 1.13 Sample raw image set of depth and ground truth.

The important property of the data set is that the measured depth data is aligned with ground truth information, and with that of the other sensor. Each depth sensor has to be fully calibrated internally and externally. We employ a conventional camera calibration method [123] for both depth sensors and the 3D scanner. Intrinsic calibration parameters for the ToF sensors are known. Given the calibration parameters, we can transform ground truth depth maps onto each depth sensor space. Once the system is calibrated, we proceed to capture the objects of interest. For each object, we record depth (**ToFD**) and intensity (**ToFI**) images from the SR4000, plus depth (**SLD**) and color (**SLC**) from the Kinect. Depth captured by the FlexScan3D is used as ground truth (**GTD**), as explained in more detail below.

Data Set

We select objects that show radiometric variations (diffuse, specular and translucent), as well as geometric variations (smooth or rough). The total 36-item test set is divided into three sub categories: diffuse material objects (class A), specular material objects (class B) and translucent objects with subsurface scattering (class C), as in fig. 1.15. Each class demonstrates geometric variation from smooth to rough surfaces (a smaller label-number means a smoother surface).

From diffuse, through specular to translucent materials, the radiometric representation becomes more complex, requiring a high dimensional model to predict

the appearance. In fact, the radiometric complexity also increases the level of challenges in recovering its depth map. This is because the complex illumination interferes with the sensing mechanism of most depth devices. Hence we categorize the radiometric complexity by three classes, representing the level of challenges posed by material variation. From smooth to rough surfaces, the geometric complexity is increased, especially due to mesostructure scale variation.

Ground Truth

We use a 3D scanner for ground truth depth acquisition. The principle of this system is similar to [100]; using illumination patterns and solving correspondences and triangulating between matching points to compute the 3D position of each surface point. Simple gray illumination patterns are used, which gives robust performance in practice. However, the patterns cannot be seen clearly enough to provide correspondences for non-Lambertian objects [16]. Recent approaches [50] suggest new high-frequency patterns, and present improvement in recovering depth in the presence of global illumination. Among all surfaces, the performance of structured-light scanning systems is best for Lambertian materials.

Original objects   After matt spray
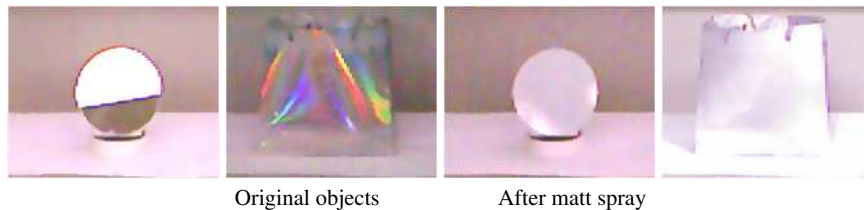
Fig. 1.14 We apply white matt spray on top of non-Lambertian objects for ground truth depth acquisition.

The data set includes non-Lambertian materials presenting various illumination effects; specular, translucent and subsurface scattering. To employ the 3D scanner system for ground truth depth acquisition of the data set, we apply white matt spray on top of each object surface, so that we can give each object a Lambertian surface while we take ground truth depth 1.14. To make it clear that the spray particles do not change the surface geometry, we have compared the depth maps captured by the 3D scanner before and after the spray on a Lambertian object. We observe that the thickness of spray particles is below the level of the depth sensing precision, meaning that the spray particles do not affect on the accuracy of the depth map in practice. Using this methodology, we are able to obtain ground truth depth for non-Lambertian objects. To ensure the level of ground truth depth, we capture the depth map of a white board. Then, we apply RANSAC to fit a plane to the depth map and measure the variation of scan data from the plane. We observe that the variation is less than 200 micrometers, which is negligible compared to depth sensor errors.

Finally, we adopt the depth map from the 3D scanner as the ground truth depth, for quantitative evaluation and analysis.
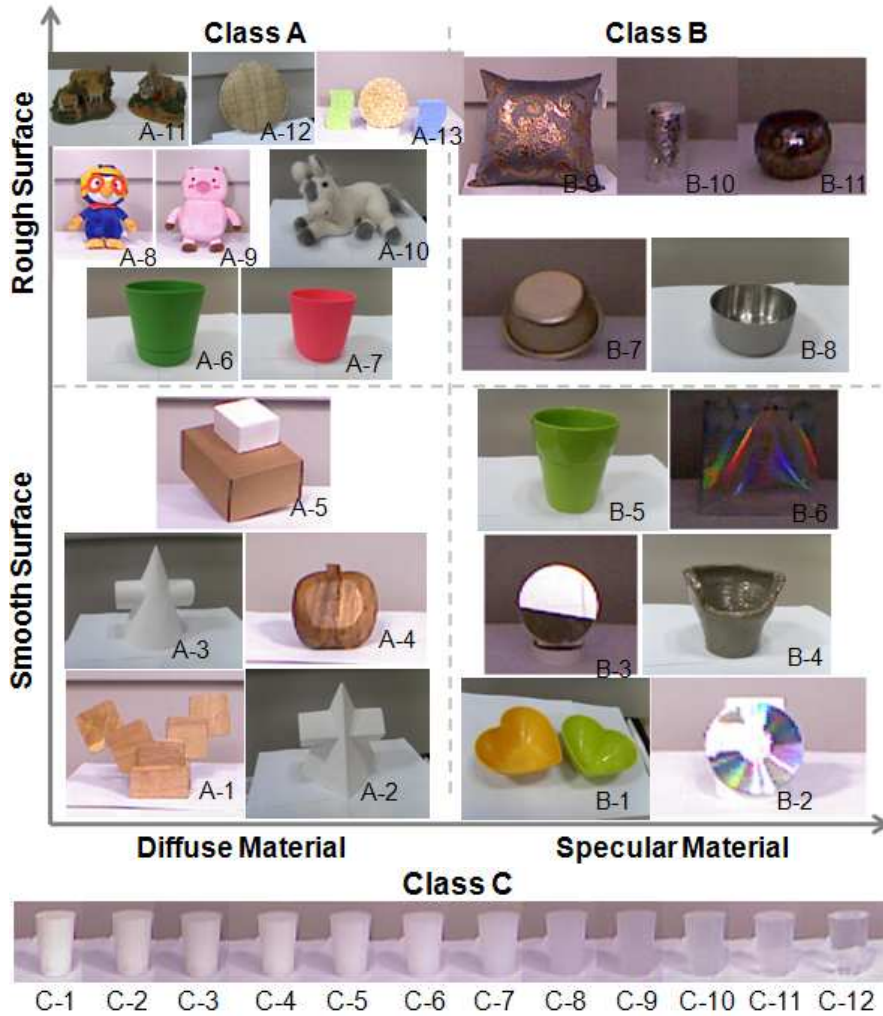
Fig. 1.15 Test images categorized by their radiometric and geometric characteristics: Class A diffuse material objects (13 images), class B specular material objects (11 images) and class C translucent objects with subsurface scattering (12 images).

1.4.3 Experiments and Analysis

In this section, we investigate the depth accuracy, the sensitivity to various different materials, and the characteristics of the two types of sensors.
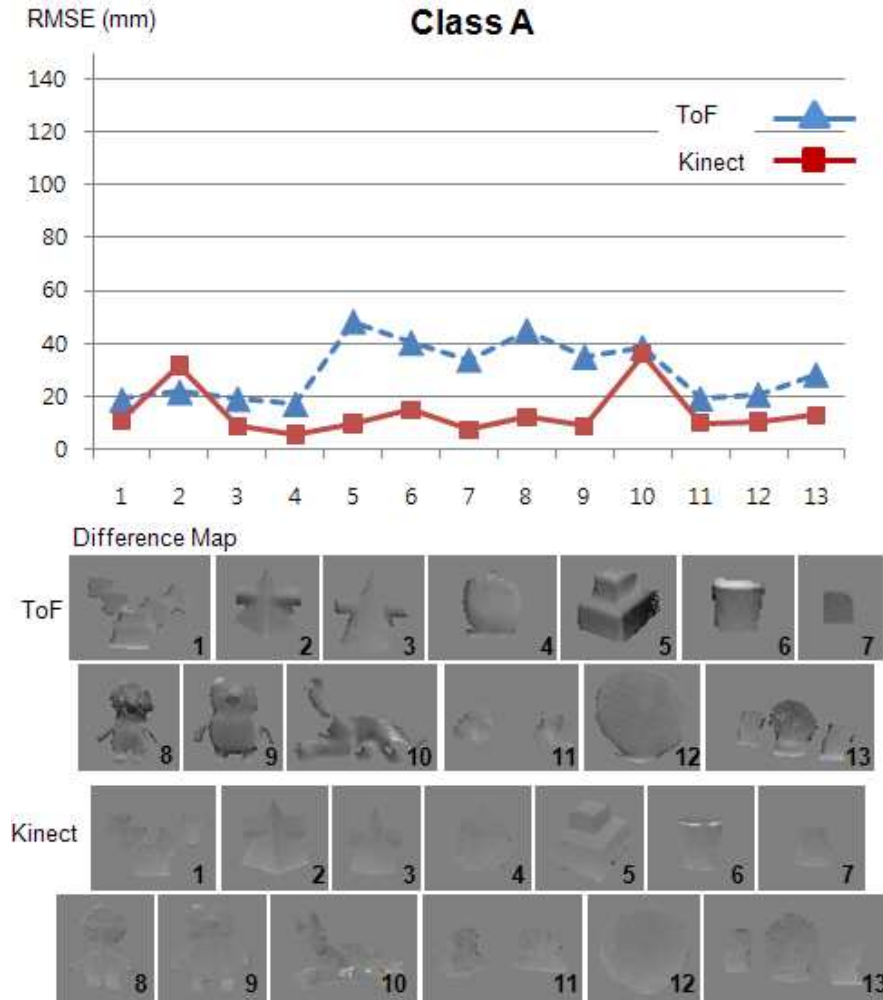
Fig. 1.16 ToF depth accuracy in RMSE (Root mean square) for class A. The RMSE values and their corresponding difference maps are illustrated. 128 in difference map represents zero difference while 129 represents the ground truth is 1 mm larger than the measurement. Likewise, 127 indicates that the ground truth is 1 mm smaller than the measurement.
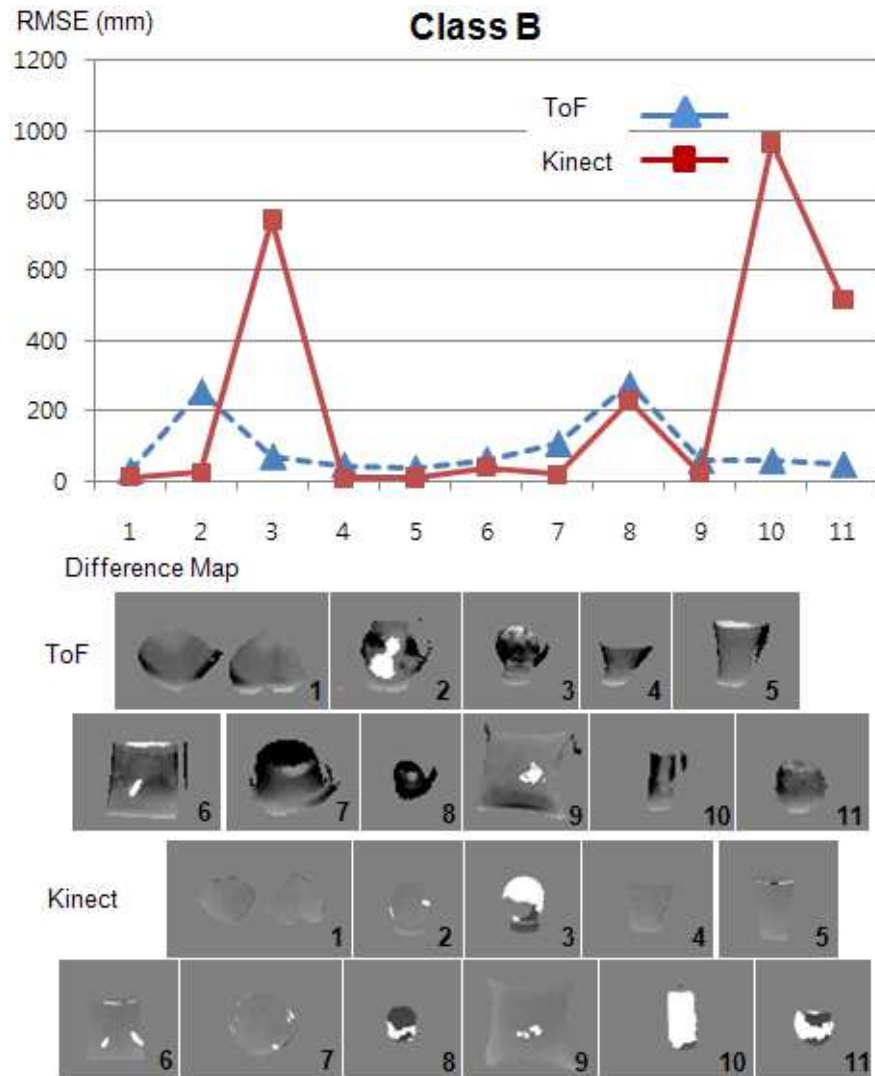
Fig. 1.17 ToF depth accuracy in RMSE (Root mean square) for class B. The RMSE values and their corresponding difference maps are illustrated.

Depth Accuracy and Sensitivity

Given the calibration parameters, we project the ground truth depth map onto each sensor space, in order to achieve viewpoint alignment (fig. 1.12). Due to the resolution difference, multiple pixels of the ground truth depth fall into each sensor pixel. We perform a bilinear interpolation to find corresponding ground truth depth for
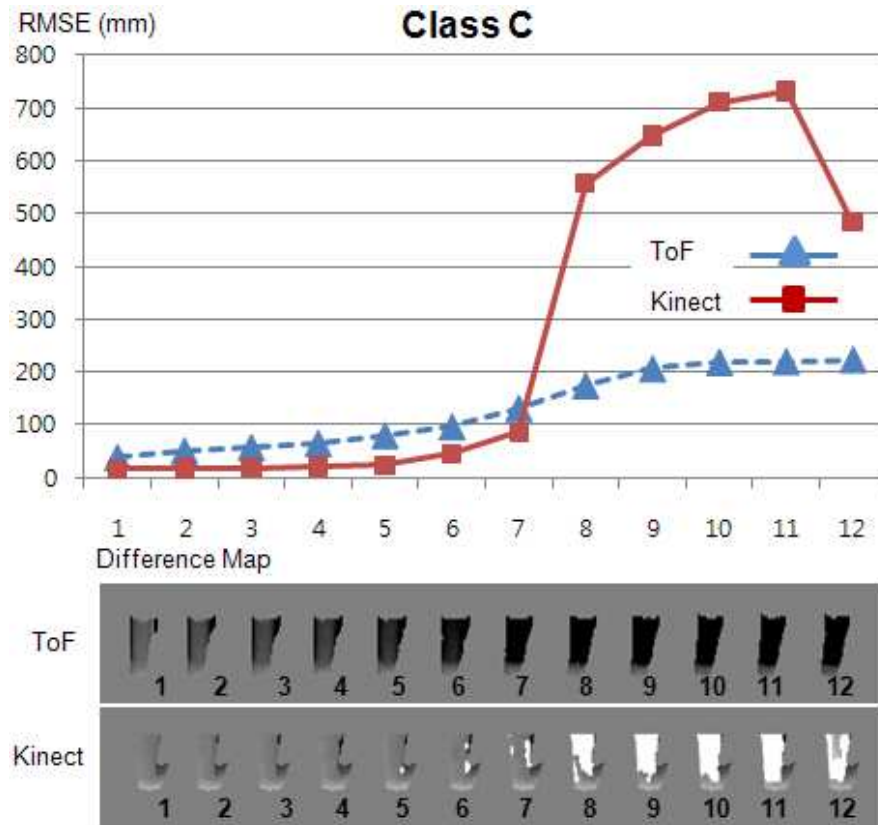
Fig. 1.18 ToF depth accuracy in RMSE (Root mean square) for class C. The RMSE values and their corresponding difference maps are illustrated.

each sensor pixel. Due to the difference of field of view and occluded regions, not all sensor pixels get corresponding ground truth depth. We exclude these pixels and occlusion boundaries from the evaluation.

According to previous work [104, 68] and manufacturer reports on the accuracy of depth sensors, the root mean square error (RMSE) of depth measurements is approximately 5–20mm at the distance of 1.5 meters. These figures cannot be generalized for all materials, illumination effects, complex geometry, and other factors. The use of more general objects and environmental conditions invariably results in higher RMSE of depth measurement than reported numbers. When we tested with a white wall, which is similar to the calibration object used in previous work [104], we obtain approximately 10.15mm at the distance of 1.5 meters. This is comparable to the previous empirical study and reported numbers.

Because only foreground objects are controlled, the white background is segmented-out for the evaluation. The foreground segmentation is straightforward because the

background depth is clearly separated from that of foreground. In figs. 1.16, 1.17 and 1.18, we plot depth errors (RMSE) and show difference maps (8 bit) between the ground truth and depth measurement. In the difference maps, gray indicates zero difference, whereas a darker (or brighter) value indicates that the ground truth is smaller (or larger) than the estimated depth. The range of difference map, $[0, 255]$, spans $[-128mm, 128mm]$ in RMSE.

	Overall	Class A	Class B	Class C
ToF	83.10	29.68	93.91	131.07
	(76.25)	(10.95)	(87.41)	(73.65)
Kinect	170.153	13.67	235.30	279.96
	(282.25)	(9.25)	(346.44)	(312.97)

* Root Mean Square Error (Standard Deviation) in (mm)

Table 1.1 Depth accuracy upon material properties. Class A: Diffuse, Class B: Specular, Class C: Translucent. See fig. 1.15 for illustration.

Several interesting observations can be made from the experiments. First, we observe that the accuracy of depth values varies substantially according to the material property. As shown in fig. 1.16, the average RMSE of class A is 26.80mm with 12.81mm of standard deviation, which is significantly smaller than the overall RMSE. This is expected, because class A has relatively simple properties, which are well-approximated by the Lambertian model. From fig. 1.17 for class B, we are unable to obtain the depth measurements on specular highlights. These highlights either prevent the IR reflection back to the sensor, or cause the reflected IR to saturate the sensor. As a result, the measured depth map shows holes, introducing a large amount of errors. The RMSE for class B is 110.79 mm with 89.07 mm of standard deviation. Class C is the most challenging subset, since it presents the subsurface scattering and translucency. As expected, upon the increase in the level of translucency, the measurement error is dramatically elevated as illustrated in fig. 1.18.

One thing to note is that the error associated with translucent materials differs from that associated with specular materials. We still observe some depth values for translucent materials, whereas the specular materials show holes in the depth map. The measurement on translucent materials is incorrect, often producing larger depth than the ground truth. Such a drift appears because the depth measurements on translucent materials are the result of both translucent foreground surface and the background behind. As a result, the corresponding measurement points lie somewhere between the foreground and the background surfaces.

Finally, the RMSE for class C is 148.51mm with 72.19mm of standard deviation. These experimental results are summarized in Table 1.1. Interestingly, the accuracy is not so much dependent on the geometric complexity of the object. Focusing on class A, although A-11, A-12 and A-13 possess complicated and uneven surface geometry, the actual accuracy is relatively good. Instead, we find that the error increases as the surface normal deviates from the optical axis of the sensor. In fact, a similar problem has been addressed by [69], in that the orientation is the source

of systematic error in sensor measurement. In addition, surfaces where the global illumination occurs due to multipath IR transport (such as the concave surfaces on A-5, A-6, A-10 of Class A) exhibit erroneous measurements.

Due to its popular application in games and human computer interaction, many researchers have tested and reported the result of Kinect applications. One of common observation is that the Kinect presents some systematic error with respect to distance. However, there has been no in-depth study on how the Kinect works on various surface materials. We measure the depth accuracy of Kinect using the data set, and illustrate the results in figs. 1.16, 1.17 and 1.18.

Overall RMSE is 191.69mm, with 262.19mm of standard deviation. Although the overall performance is worse than that of ToF sensor, it provides quite accurate results for class A. From the experiments, it is clear that material properties are strongly correlated with depth accuracy. The RMSE for class A is 13.67mm with 9.25mm of standard deviation. This is much smaller than the overall RMSE, 212.56mm. However, the error dramatically increases in class B (303.58mm with 249.26mm of deviation). This is because the depth values for specular materials causes holes in the depth map, similar to the behavior of the ToF sensor.

From the experiments on class C, we observe that the depth accuracy drops significantly upon increasing the level of translucency, especially starting at the object C-8. In the graph shown in fig. 1.18, one can observe that the RMSE is reduced with a completely transparent object (C-12, a pure water). It is because caustic effects appear along the object, sending back unexpected IR signals to the sensor. Since the sensor receives the reflected IR, RMSE improves in this case. However this does not always stand for a qualitative improvement. The overall RMSE for class C is 279.96mm with 312.97mm of standard deviation. For comparison, see table 1.1.

ToF vs Kinect Depth

In previous sections, we have demonstrated the performance of ToF and structured light sensors. We now characterize the error patterns of each sensor, based on the experimental results. For both sensors, we observe two major errors; data drift and data loss. It is hard to state which kind of error is most serious, but it is clear that both must be addressed. In general, the ToF sensor tends to show data drift, whereas the structured light sensor suffers from data loss. In particular, the ToF sensor produces a large offset in depth values along boundary pixels and transparent pixels, which correspond to data drift. Under the same conditions, the structured light sensor tends to produce holes, in which the depth cannot be estimated. For both sensors, specular highlights lead to data loss.

1.4.4 Enhancement

In this section we apply simple denoising, superresolution and inpainting algorithms on the data set, and report their performance. For denoising and superresolution, we test only on class A, because class B and C often suffer from significant data drift or data loss, which neither denoising nor superresolution alone can address.

By excluding class B and C, it is possible to precisely evaluate the quality gain due to each algorithm. On the other hand, we adopt the image inpainting algorithm on class B, because in this case the typical errors are holes, regardless of sensor type. Although the characteristics of depth images differ from those of color images, we apply color inpainting algorithms on depth images, to compensate for the data loss in class B. We then report the accuracy gain, after filling in the depth holes. Note that the aim of this study is not to claim any state-of-the art technique, but to provide baseline test results on the data set.

We choose a bilateral filter for denoising the depth measurements. The bilateral filter size is set to 3×3 (for ToF, 174×144 resolution) or 10×10 (for Kinect, 640×480 resolution). The standard deviation of the filter is set to 2 in both cases. We compute the RMSE after denoising and obtain 27.78mm using ToF, and 13.30mm using Kinect as demonstrated in tables 1.2 and 1.3. On average, the bilateral filter provides an improvement in depth accuracy; 1.98mm gain for ToF and 0.37mm for Kinect. Figure 1.19 shows the noise-removed results, with input depth.

| ToF | Kinect |
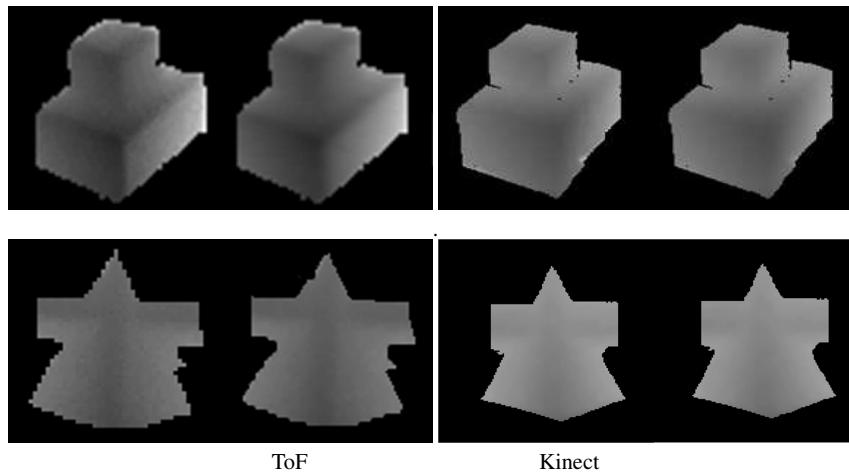
Fig. 1.19 Results before and after bilateral filtering (top) and bilinear interpolation (bottom).

We perform bilinear interpolation for superresolution, increasing the resolution twice per dimension (upsampling by a factor of four). We compute the RMSE before and after the superresolution process from the identical ground truth depth map. The depth accuracy is decreased after superresolution by 2.25mm (ToF) or 1.35mm

ToF   Kinect
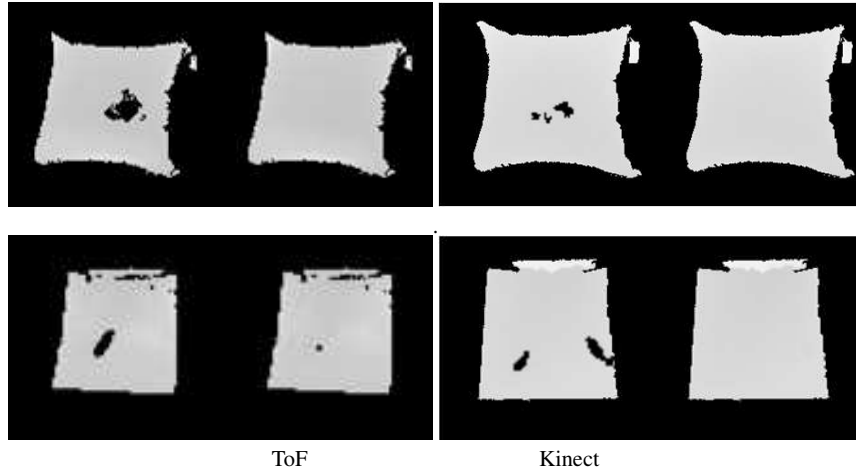
Fig. 1.20 Before and after inpainting

(Kinect). The loss of depth accuracy is expected, because the recovery of surface details from a single low resolution image is an ill-posed problem. The quantitative evaluation results for denoising and superresolution are summarized in tables 1.2 and 1.3.

For inpainting, we employ an exemplar-based algorithm [19]. Criminisi et al. design a fill-order to retain the linear structure of scene, and so their method is well-suited for depth images. For hole filling, we set the patch size to 3×3 for ToF and to 9×9 for Kinect, in order to account for the difference in resolution. Finally, we compute the RMSE after inpainting, which is 75.71mm for ToF and 125.73mm for Kinect. The overall accuracy has been improved by 22.30mm for ToF and 109.57mm for Kinect. The improvement for Kinect is more significant than ToF, because the data loss appears more frequently in Kinect than ToF. After the inpainting process, we obtain a reasonable quality improvement for class B.

	Original RMSE	Bilateral Filtering	Bilinear Interpolation
ToF	29.68	27.78	31.93
	(10.95)	(10.37)	(23.34)
Kinect	13.67	13.30	15.02
	(9.25)	(9.05)	(12.61)

* Root Mean Square Error (Standard Deviation) in mm

Table 1.2 Depth accuracy before/after bilateral filtering and superresolution for class A. See fig. 1.19 for illustration.

Based on the experimental study, we confirm that both depth sensors provide relatively accurate depth measurements for diffuse materials (class A). For specular

	Original RMSE	Example-based Inpainting
ToF	93.91	71.62
	(87.41)	(71.80)
Kinect	235.30	125.73
	(346.44)	(208.66)

* Root Mean Square Error (Standard Deviation) in mm

Table 1.3 Depth accuracy before/after inpainting for class B. See fig. 1.20 for illustration.

materials (class B), both sensors exhibit data loss appearing as holes in the measured depth. Such a data loss causes a large amount of error in the depth images. For translucent materials (class C), the ToF sensor shows non-linear data drift towards the background. On the other hand, the Kinect sensor shows data loss on translucent materials. Upon the increase of translucency, the performance of both sensors is degraded accordingly.

1.5 Conclusions

This chapter has reported both quantitative and qualitative experimental results for the evaluation of each sensor type. Moreover, we provide a well-structured standard data set of depth images from real world objects, with accompanying ground-truth depth. The data-set spans a wide variety of radiometric and geometric complexity, which is well-suited to the evaluation of depth processing algorithms. The analysis has revealed important problems in depth acquisition and processing, especially measurement errors due to material properties. The data-set will provide a standard framework for the evaluation of other denoising, super-resolution, interpolation and related depth-processing algorithms.

	Object	Ground Truth	ToF Depth	Kinect Depth
A-5				
A-10				
B-3				
B-7				
B-10				
C-12				
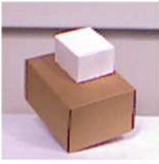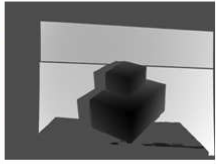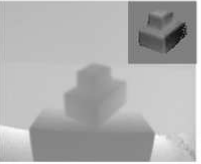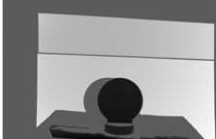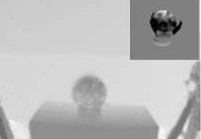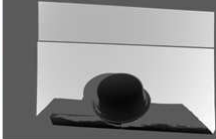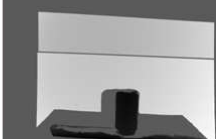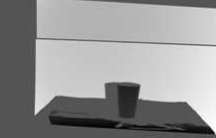
Fig. 1.21 Sample depth images and difference maps from the test image set.

Chapter 2
Disambiguation of Time-of-Flight Data

Abstract The maximum range of a time-of-flight camera is limited by the periodicity of the measured signal. Beyond a certain range, which is determined by the signal frequency, the measurements are confounded by phase-wrapping. This effect is demonstrated in real examples. Several phase-unwrapping methods, which can be used to extend the range of time-of-flight cameras, are discussed. Simple methods can be based on the measured amplitude of the reflected signal, which is itself related to the depth of objects in the scene. More sophisticated unwrapping methods are based on zero-curl constraints, which enforce spatial consistency on the phase measurements. Alternatively, if more than one depth-camera is used, then the data can be unwrapped by enforcing consistency between different views of the same scene point. The relative merits and shortcomings of these methods are evaluated, and the prospects for hardware-based approaches, involving frequency-modulation are discussed.

2.1 Introduction

Time-of-Flight cameras emit modulated infrared light and detect its reflection from the illuminated scene points. According to the ToF principle described in chapter 1, the detected signal is gated and integrated using internal reference signals, to form the tangent of the phase ϕ of the detected signal. Since the tangent of ϕ is a periodic function with a period of 2π, the value $\phi + 2n\pi$ gives exactly the same tangent value for any non-negative integer n.

Commercially available ToF cameras compute ϕ on the assumption that ϕ is within the range of $[0, 2\pi)$. For this reason, each modulation frequency f has its maximum range $d_{\max}$ corresponding to 2π, encoded without ambiguity:

$$d_{\max} = \frac{c}{2f},\qquad(2.1)$$

where c is the speed of light. For any scene points farther than $d_{\max}$, the measured distance d is much shorter than its actual distance $d + n d_{\max}$. This phenomenon is called *phase wrapping*, and estimating the unknown number of wrappings n is called *phase unwrapping*.

For example, the Mesa SR4000 [80] camera records a 3D point $\mathbf{X}_p$ at each pixel p, where the measured distance d_p equals $\|\mathbf{X}_p\|$. In this case, the unwrapped 3D point $\mathbf{X}_p(n_p)$ with number of wrappings n_p can be written as

$$\mathbf{X}_p(n_p) = \frac{d_p + n_p d_{\max}}{d_p} \mathbf{X}_p. \tag{2.2}$$

Figure 2.1(a) shows a typical depth map acquired by the SR4000 [80], and fig. 2.1(b) shows its unwrapped depth map. As shown in fig. 2.1(e), phase unwrapping is crucial for recovering large-scale scene structure.

To increase the usable range of ToF cameras, it is also possible to extend the maximum range $d_{\max}$ by decreasing the modulation frequency f. In this case, the integration time should also be extended, to acquire a high quality depth map, since the depth noise is inversely proportional to f. With extended integration time, moving objects are more likely to result in motion artifacts. In addition, we do not know at which modulation frequency phase wrapping does not occur, without exact knowledge regarding the scale of the scene.

If we can accurately unwrap a depth map acquired at a high modulation frequency, then the unwrapped depth map will suffer less from noise than a depth map acquired at a lower modulation frequency, integrated for the same time. Also, if a phase unwrapping method does not require exact knowledge on the scale of the scene, then the method will be applicable in more large-scale environments.

There exist a number of phase unwrapping methods [35, 93, 65, 18, 30, 29, 83, 17] that have been developed for ToF cameras. According to the number of input depth maps, the methods are categorized into two groups: those using a single depth map [93, 65, 18, 30, 83] and those using multiple depth maps [35, 92, 29, 17]. The following subsections introduce their principles, advantages and limitations.

2.2 Phase Unwrapping From a Single Depth Map

ToF cameras such as the SR4000 [80] provide an amplitude image along with its corresponding depth map. The amplitude image is encoded with the strength of the detected signal, which is inversely proportional to the squared distance. To obtain *corrected amplitude A'* [89], which is proportional to the reflectivity of a scene surface with respect to the infrared light, we can multiply amplitude A and its corresponding squared distance d^2:

$$A' = A d^2. \tag{2.3}$$

(a)   (b)   (c)

(d)   (e)
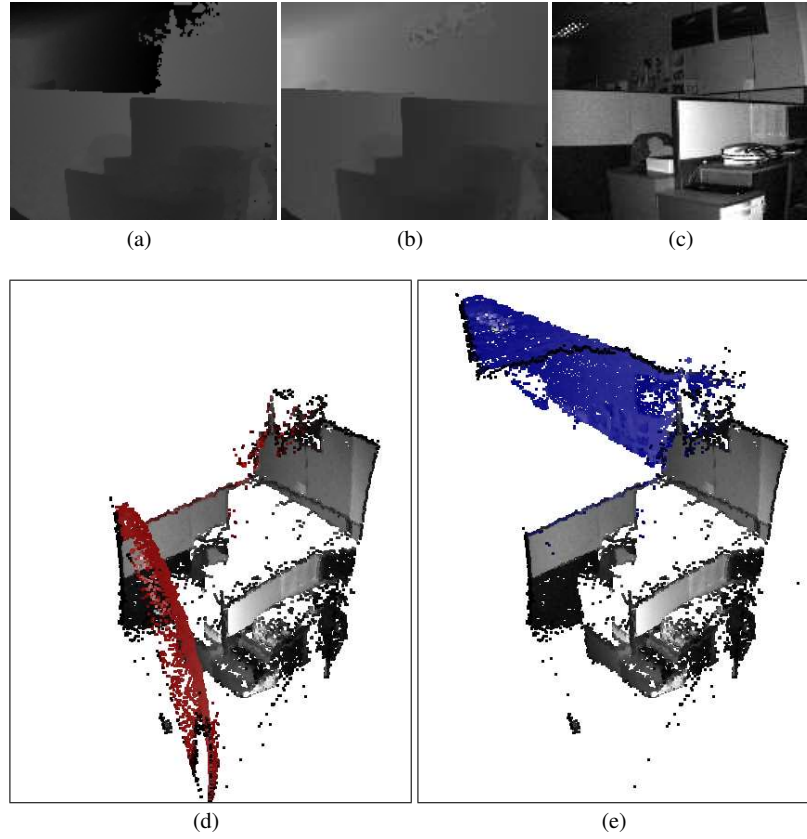
Fig. 2.1 Structure recovery through phase unwrapping. (a) Wrapped ToF depth map. (b) Unwrapped depth map corresponding to (a). Only the distance values are displayed in (a) and (b), to aid visibility. The intensity is proportional to the distance. (c) Amplitude image associated with (a). (d) and (e) display the 3D points corresponding to (a) and (b), respectively. (d) The wrapped points are displayed in red. (e) Their unwrapped points are displayed in blue. The remaining points are textured using the original amplitude image (c).

Figure 2.2 shows an example of amplitude correction. It can be observed from fig. 2.2(c) that the corrected amplitude is low in the wrapped region. Based on the assumption that the reflectivity is constant over the scene, the corrected amplitude values can play an important role in detecting wrapped regions [93, 18, 83].

Poppinga and Birk [93] use the following inequality for testing if the depth of pixel p has been wrapped:

$$A'_p \leq A_p^{\text{ref}} T, \tag{2.4}$$

where T is a manually chosen threshold, and A_p^{ref} is the reference amplitude of pixel p when viewing a white wall at one meter, approximated by

(a)   (b)   (c)
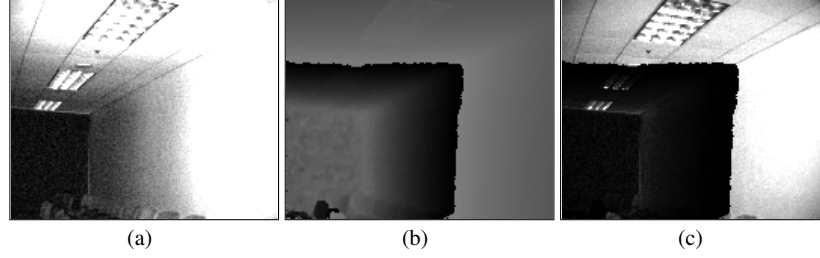
Fig. 2.2 Amplitude correction example. (a) Amplitude image. (b) ToF depth map. (c) Corrected amplitude image. The intensity in (b) is proportional to the distance. The lower-left part of (b) has been wrapped. Images courtesy of Choi *et al.* [18].

$$A_p^{\text{ref}} = B - \left((x_p - c_x)^2 + (y_p - c_y)^2\right), \tag{2.5}$$

where B is a constant. The image coordinates of p are (x_p, y_p), and (c_x, c_y) is approximately the image center, which is usually better illuminated than the periphery. A_p^{ref} compensates this effect by decreasing $A_p^{\text{ref}}T$ if pixel p is in the periphery.

After the detection of wrapped pixels, it is possible to directly obtain an unwrapped depth map by setting the number of wrappings of the wrapped pixels to 1 on the assumption that the maximum number of wrappings is 1.

The assumption on the constant reflectivity tends to be broken when the scene is composed of different objects with varying reflectivity. This assumption cannot be fully relaxed without detailed knowledge of scene reflectivity, which is hard to obtain in practice. To robustly handle varying reflectivity, it is possible to adaptively set the threshold for each image and to enforce spatial smoothness on the detection results.

Choi *et al.* [18] model the distribution of corrected amplitude values in an image using a mixture of Gaussians with two components, and apply expectation maximization [6] to learning the model:

$$p(A_p') = \alpha_H p(A_p'|\mu_H, \sigma_H^2) + \alpha_L p(A_p'|\mu_L, \sigma_L^2), \tag{2.6}$$

where $p(A_p'|\mu, \sigma^2)$ denotes a Gaussian distribution with mean μ and variance σ^2, and α is the coefficient for each distribution. The components $p(A_p'|\mu_H, \sigma_H^2)$ and $p(A_p'|\mu_L, \sigma_L^2)$ describe the distributions of high and low corrected amplitude values, respectively. Similarly, the subscripts H and L denote labels *high* and *low*, respectively. Using the learned distribution, it is possible to write a probabilistic version of eq. (2.4) as

$$P(H|A_p') < 0.5, \tag{2.7}$$

where $P(H|A_p') = \alpha_H p(A_p'|\mu_H, \sigma_H^2)/p(A_p')$.

To enforce spatial smoothness on the detection results, Choi *et al.* [18] use a segmentation method [96] based on Markov random fields (MRFs). The method finds the binary labels $n \in \{H, L\}$ or $\{0, 1\}$ that minimize the following energy:

$$E = \sum_p D_p(n_p) + \sum_{(p,q)} V(n_p, n_q), \qquad (2.8)$$

where $D_p(n_p)$ is a data cost that is defined as $1 - P(n_p|A'_p)$, and $V(n_p, n_q)$ is a discontinuity cost that penalizes a pair of adjacent pixels p and q if their labels n_p and n_q are different. $V(n_p, n_q)$ is defined in a manner of increasing the penalty if a pair of adjacent pixels have similar corrected amplitude values:

$$V(n_p, n_q) = \lambda \exp\left(-\beta(A'_p - A'_q)^2\right)\delta(n_p \neq n_q), \qquad (2.9)$$

where λ and β are constants, which are either manually chosen or adaptively determined. $\delta(x)$ is a function that evaluates to 1 if its argument is true and evaluates to zero otherwise.

(a)   (b)   (c)
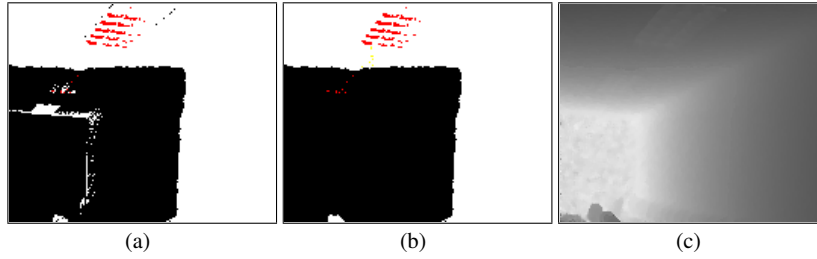
Fig. 2.3 Detection of wrapped regions. (a) Result obtained by expectation maximization. (b) Result obtained by MRF optimization. The pixels with labels L and H are colored in black and white, respectively. The red pixels are those with extremely high or low amplitude values, which are not processed during the classification. (c) Unwrapped depth map corresponding to fig. 2.2(b). The intensity is proportional to the distance. Images courtesy of Choi *et al.* [18].

Figure 2.3 shows the classification results obtained by Choi *et al.* [18] Because of varying reflectivity of the scene, the result in fig. 2.3(a) exhibits misclassified pixels in the lower-left part. The misclassification is reduced by applying the MRF optimization as shown in fig. 2.3(b). Figure 2.3(c) shows the unwrapped depth map obtained by Choi *et al.* [18], corresponding to fig. 2.2(b).

McClure *et al.* [83] also use a segmentation-based approach, in which the depth map is segmented into regions by applying the watershed transform [84]. In their method, wrapped regions are detected by checking the average corrected amplitude of each region.

On the other hand, depth values tend to be highly discontinuous across the wrapping boundaries, where there are transitions in the number of wrappings. For example, the depth maps in fig. 2.1(a) and fig. 2.2(b) show such discontinuities. On the assumption that the illuminated surface is smooth, the depth difference between adjacent pixels should be small. If the difference between measured distances is greater than $0.5d_{\max}$ for any adjacent pixels, say $d_p - d_q > 0.5d_{\max}$, we can set the number of relative wrappings, or, briefly, the shift $n_q - n_p$ to 1 so that the unwrapped

difference will satisfy $-0.5d_{max} \le d_p - d_q - (n_q - n_p)d_{max} < 0$, minimizing the discontinuity.

Figure 2.4 shows a one-dimensional phase unwrapping example. In fig. 2.4(a), the phase difference between pixels p and q is greater than 0.5 (or π). The shifts that minimize the difference between adjacent pixels are 1 (or, $n_q - n_p = 1$) for p and q, and 0 for the other pairs of adjacent pixels. On the assumption that n_p equals 0, we can integrate the shifts from left to right to obtain the unwrapped phase image in fig. 2.4(b).

| 0.6 | 0.8 | 0.9 | 0.1 | 0.2 | 0.3 | | 0.6 | 0.8 | 0.9 | 1.1 | 1.2 | 1.3 |

p q p q

(a)   (b)

Fig. 2.4 One-dimensional phase unwrapping example. (a) Measured phase image. (b) Unwrapped phase image where the phase difference between p and q is now less than 0.5. In (a) and (b), all the phase values have been divided by 2π. For example, the displayed value 0.1 corresponds to 0.2π.

0.0	0.1	0.2	0.3		1.0	1.1	0.2	0.3
0.0	0.0	0.3	0.4		1.0	1.0	0.3	0.4
0.9	0.8	0.6	0.5		0.9	0.8	0.6	0.5
0.8	0.8	0.7	0.6		0.8	0.8	0.7	0.6

(a)   (b)

1.0	1.1	1.2	1.3		1.0	1.1	1.2	1.3
1.0	1.0	1.3	1.4		1.0	1.0	1.3	1.4
0.9	0.8	0.6	0.5		0.9	0.8	1.6	1.5
0.8	0.8	0.7	0.6		0.8	0.8	1.7	1.6

(c)   (d)
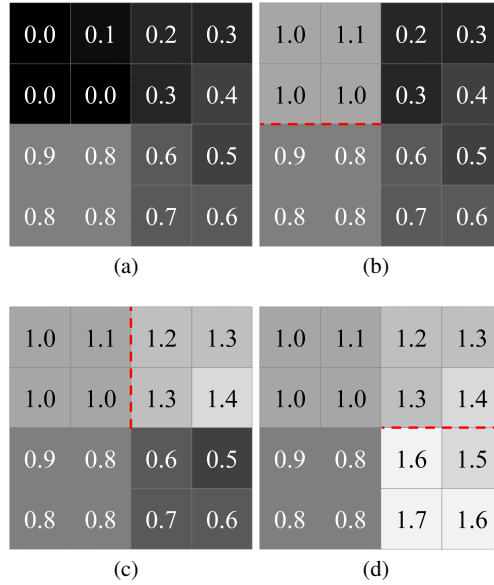
Fig. 2.5 Two-dimensional phase unwrapping example. (a) Measured phase image. (b–d) Sequentially unwrapped phase images where the phase difference across the red dotted line has been minimized. From (a) to (d), all the phase values have been divided by 2π. For example, the displayed value 0.1 corresponds to 0.2π.

Figure 2.5 shows a two-dimensional phase unwrapping example. From fig. 2.5(a) to (d), the phase values are unwrapped in a manner of minimizing the phase difference across the red dotted line. In this two-dimensional case, the phase differences greater than 0.5 never vanish, and the red dotted line cycles around the image center infinitely. This is because of the local phase error that causes the violation of the *zero-curl* constraint [46, 40].
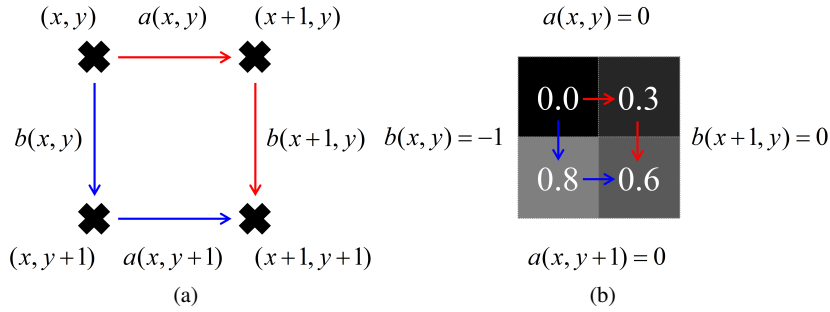
Fig. 2.6 Zero-curl constraint: $a(x,y)+b(x+1,y)=b(x,y)+a(x,y+1)$. (a) The number of relative wrappings between $(x+1,y+1)$ and (x,y) should be consistent regardless of its integrating paths. For example, two different paths (red and blue) are shown. (b) shows an example in which the constraint is not satisfied. The four pixels correspond to the four pixels in the middle of fig. 2.5(a).

Figure 2.6 illustrates the zero-curl constraint. Given four neighboring pixel locations (x,y), $(x+1,y)$, $(x,y+1)$, and $(x+1,y+1)$, let $a(x,y)$ and $b(x,y)$ denote the shifts $n(x+1,y)-n(x,y)$ and $n(x,y+1)-n(x,y)$, respectively, where $n(x,y)$ denotes the number of wrappings at (x,y). Then, the shift $n(x+1,y+1)-n(x,y)$ can be calculated in two different ways: either $a(x,y)+b(x+1,y)$ or $b(x,y)+a(x,y+1)$ following one of the two different paths shown in fig. 2.6(a). For any phase unwrapping results to be consistent, the two values should be the same, satisfying the following equality:

$$a(x,y)+b(x+1,y)=b(x,y)+a(x,y+1). \tag{2.10}$$

Because of noise or discontinuities in the scene, the zero-curl constraint may not be satisfied locally, and the local error is propagated to the entire image during the integration. There exist classical phase unwrapping methods [46, 40] applied in magnetic resonance imaging [75] and interferometric synthetic aperture radar (SAR) [63], which rely on detecting [46] or fixing [40] broken zero-curl constraints. Indeed, these classical methods [46, 40] have been applied to phase unwrapping for ToF cameras [65, 30].

2.2.1 Deterministic Methods

Goldstein *et al.* [46] assume that the shift is either 1 or -1 between adjacent pixels if their phase difference is greater than π, and assume that it is 0 otherwise. They detect cycles of four neighboring pixels, referred to as *plus and minus residues*, which do not satisfy the zero-curl constraint.

If any integration path encloses an unequal number of plus and minus residue, the integrated phase values on the path suffer from global errors. In contrast, if any integration path encloses an equal number of plus and minus residues, the global error is balanced out. To prevent global errors from being generated, Goldstein *et al.* [46] connect nearby plus and minus residues with *cuts*, which interdict the integration paths, such that no net residues can be encircled.

After constructing the cuts, the integration starts from a pixel p, and each neighboring pixel q is unwrapped relatively to p in a greedy and sequential manner if q has not been unwrapped and if p and q are on the same side of the cuts.

2.2.2 Probabilistic Methods

Frey *et al.* [40] propose a very loopy belief propagation method for estimating the shift that satisfies the zero-curl constraints. Let the set of shifts, and a measured phase image, be denoted by

$$S = \left\{ a(x,y),\ b(x,y)\ :\ x = 1,\ldots,N-1;\ y = 1,\ldots,M-1 \right\}$$
$$\text{and}$$
$$\Phi = \left\{ \phi(x,y)\ :\ 0 \le \phi(x,y) < 1,\ x = 1,\ldots,N;\ y = 1,\ldots,M \right\},$$

respectively, where the phase values have been divided by 2π. The estimation is then recast as finding the solution that maximizes the following joint distribution:

$$p(S,\Phi) \propto \prod_{x=1}^{N-1} \prod_{y=1}^{M-1} \delta(a(x,y) + b(x+1,y) - a(x,y+1) - b(x,y))$$
$$\times \prod_{x=1}^{N-1} \prod_{y=1}^{M} e^{-(\phi(x+1,y) - \phi(x,y) + a(x,y))^2 / 2\sigma^2} \times \prod_{x=1}^{N} \prod_{y=1}^{M-1} e^{-(\phi(x,y+1) - \phi(x,y) + b(x,y))^2 / 2\sigma^2}$$

where $\delta(x)$ evaluates to 1 if $x = 0$ and to 0 otherwise. The variance σ^2 is estimated directly from the wrapped phase image [40].

Frey *et al.* [40] construct a graphical model describing the factorization of $p(S,\Phi)$, as shown in fig. 2.7. In the graph, each shift node (white disc) is located between two pixels, and corresponds to either an x-directional shift (a's) or a y-directional shift (b's). Each constraint node (black disc) corresponds to a zero-curl constraint, and is connected to its four neighboring shift nodes. Every node passes
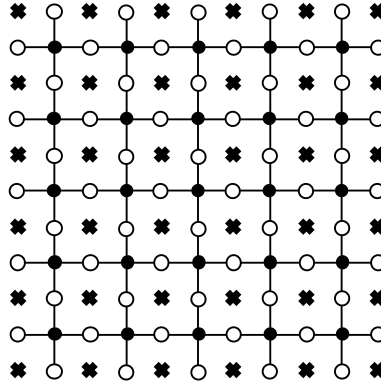
Fig. 2.7 Graphical model that describes the zero-curl constraints (black discs) between neighboring shift variables (white discs). 3-element probability vectors (μ's) on the shifts between adjacent nodes (-1, 0, or 1) are propagated across the network. The x marks denote pixels [40].

a message to its neighboring node, and each message is a 3-vector denoted by μ, whose elements correspond to the allowed values of shifts, -1, 0, and 1. Each element of μ can be considered as a probability distribution over the three possible values [40].
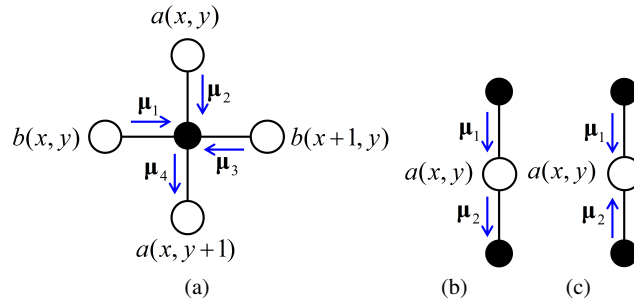
Fig. 2.8 (a) Constraint-to-shift vectors are computed from incoming shift-to-constraint vectors. (b) Shift-to-constraint vectors are computed from incoming constraint-to-shift vectors. (c) Estimates of the marginal probabilities of the shifts given the data are computed by combining incoming constraint-to-shift vectors [40].

Figure 2.8(a) illustrates the computation of a message μ_4 from a constraint node to one of its neighboring shift nodes. The constraint node receives messages μ_1, μ_2, and μ_3 from the rest of its neighboring shift nodes, and filters out the joint message elements that do not satisfy the zero-curl constraint:

$$\mu_{4i} = \sum_{j=-1}^{1} \sum_{k=-1}^{1} \sum_{l=-1}^{1} \delta(k+l-i-j)\mu_{1j}\mu_{2k}\mu_{3l}, \qquad (2.11)$$

where μ_{4i} denotes the element of μ_4, corresponding to shift value $i \in \{-1, 0, 1\}$.

Figure 2.8(b) illustrates the computation of a message μ_2 from a shift node to one of its neighboring constraint node. Among the elements of the message μ_1 from the other neighboring constraint node, the element, which is consistent with the measured shift $\phi(x,y) - \phi(x+1,y)$, is amplified:

$$\mu_{2i} = \mu_{1i} \exp\left(-\left(\phi(x+1,y) - \phi(x,y) + i\right)^2 / 2\sigma^2\right). \qquad (2.12)$$

After the messages converge (or, after a fixed number of iterations), an estimate of the marginal probability of a shift is computed by using the messages passed into its corresponding shift node, as illustrated in fig. 2.8(c):

$$\hat{P}\big(a(x,y) = i | \Phi\big) = \frac{\mu_{1i}\mu_{2i}}{\sum_j \mu_{1j}\mu_{2j}}. \qquad (2.13)$$

Given the estimates of the marginal probabilities, the most probable value of each shift node is selected. If some zero-curl constraints remain violated, a robust integration technique, such as least-squares integration [44] should be used [40].

2.2.3 Discussion

The aforementioned phase unwrapping methods using a single depth map [93, 65, 18, 30, 83] have an advantage that the acquisition time is not extended, keeping the motion artifacts at a minimum. The methods, however, rely on strong assumptions that are fragile in real world situations. For example, the reflectivity of the scene surface may vary in a wide range. In this case, it is hard to detect wrapped regions based on the corrected amplitude values. In addition, the scene may be discontinuous if it contains multiple objects that occlude one another. In this case, the wrapping boundaries tend to coincide with object boundaries, and it is often hard to observe large depth discontinuities across the boundaries, which play an important role in determining the number of relative wrappings.

The assumptions can be relaxed by using multiple depth maps at a possible extension of acquisition time. The next subsection introduces phase unwrapping methods using multiple depth maps.

2.3 Phase Unwrapping From Multiple Depth Maps

Suppose that a pair of depth maps M_1 and M_2 of a static scene are given, which have been taken at different modulation frequencies f_1 and f_2 from the same viewpoint. In this case, pixel p in M_1 corresponds to pixel p in M_2, since the corresponding region of the scene is projected onto the same location of M_1 and M_2. Thus the

unwrapped distances at those corresponding pixels should be consistent within the noise level.

Without prior knowledge, the noise in the unwrapped distance can be assumed to follow a zero-mean distribution. Under this assumption, the maximum likelihood estimates of the numbers of wrappings at the corresponding pixels should minimize the difference between their unwrapped distances. Let m_p and n_p be the numbers of wrappings at pixel p in M_1 and M_2, respectively. Then we can choose m_p and n_p that minimize $g(m_p, n_p)$ such that

$$g(m_p, n_p) = \left| d_p(f_1) + m_p d_{\max}(f_1) - d_p(f_2) - n_p d_{\max}(f_2) \right|, \qquad (2.14)$$

where $d_p(f_1)$ and $d_p(f_2)$ denote the measured distances at pixel p in M_1 and M_2 respectively, and $d_{\max}(f)$ denotes the maximum range of f.

The depth consistency constraint has been mentioned by Göktürk *et al.* [45] and used by Falie and Buzuloiu [35] for phase unwrapping of ToF cameras. The illuminating power of ToF cameras is, however, limited due to the eye-safety problem, and the reflectivity of the scene may be very low. In this situation, the amount of noise may be too large for accurate numbers of wrappings to minimize $g(m_p, n_p)$. For robust estimation against noise, Droeschel *et al.* [29] incorporate the depth consistency constraint into their earlier work [30] for a single depth map, using an auxiliary depth map of a different modulation frequency.

If we acquire a pair of depth maps of a dynamic scene sequentially and independently, the pixels at the same location may not correspond to each other. To deal with such dynamic situations, several approaches [92, 17] acquire a pair of depth maps simultaneously. These can be divided into single-camera and multi-camera methods, as described below.

2.3.1 Single-Camera Methods

For obtaining a pair of depth maps sequentially, four samples of integrated electric charge are required per each integration period, resulting in eight samples within a pair of two different integration periods. Payne *et al.* [92] propose a special hardware system that enables simultaneous acquisition of a pair of depth maps at different frequencies by dividing the integration period into two, switching between frequencies f_1 and f_2, as shown in fig. 2.9.

Payne *et al.* [92] also show that it is possible to obtain a pair of depth maps with only five or six samples within a combined integration period, using their system. By using fewer samples, the total readout time is reduced and the integration period for each sample can be extended, resulting in an improved signal-to-noise ratio.
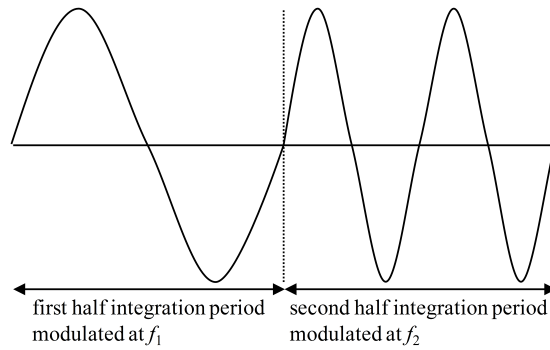
Fig. 2.9 Frequency modulation within an integration period. The first half is modulated at f_1, and the other half is modulated at f_2.

first half integration period modulated at f_1

second half integration period modulated at f_2

2.3.2 Multi-Camera Methods

Choi and Lee [17] use a *pair* of commercially available ToF cameras to simultaneously acquire a pair of depth maps from different viewpoints. The two cameras C_1 and C_2 are fixed to each other, and the mapping of a 3D point $\mathbf{X}$ from C_1 to its corresponding point $\mathbf{X}'$ from C_2 is given by $(\mathbf{R}, \mathbf{T})$, where $\mathbf{R}$ is a 3×3 rotation matrix, and $\mathbf{T}$ is a 3×1 translation vector. In [17], the extrinsic parameters $\mathbf{R}$ and $\mathbf{T}$ are assumed to have been estimated. Figure 2.10(a) shows the stereo ToF camera system.

(a)   (b) 31MHz   (c) 29MHz

(d)   (e)   (f)
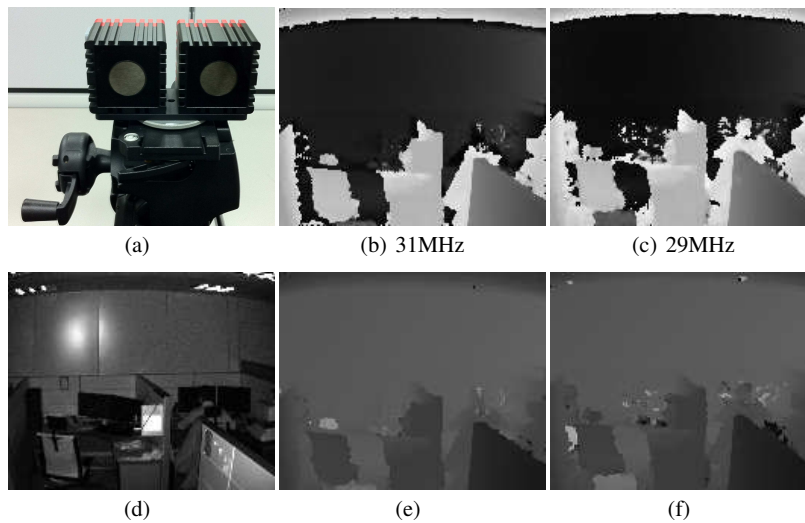
Fig. 2.10 (a) Stereo ToF camera system. (b, c) Depth maps acquired by the system. (d) Amplitude image corresponding to (b). (e, f) Unwrapped depth maps, corresponding to (b) and (c), respectively. The intensity in (b, c, e, f) is proportional to the depth. The maximum intensity (255) in (b, c) and (e, f) correspond to 5.2m and 15.6m, respectively. Images courtesy of Choi and Lee [17].

Denoting by M_1 and M_2 a pair of depth maps acquired by the system, a pixel p in M_1 and its corresponding pixel q in M_2 should satisfy:

$$\mathbf{X}'_q(n_q) = \mathbf{R}\mathbf{X}_p(m_p) + \mathbf{T}, \qquad (2.15)$$

where $\mathbf{X}_p(m_p)$ and $\mathbf{X}'_q(n_q)$ denote the unwrapped 3D points of p and q with their numbers of wrappings m_p and n_q, respectively.

Based on the relation in Eq. (2.15), Choi and Lee [17] generalize the depth consistency constraint in Eq. (2.14) for a single camera to those for the stereo camera system:

$$
\begin{aligned}
D_p(m_p) &= \min_{n_{q^\star} \in \{0,\dots,N\}} \left(\left\| \mathbf{X}'_{q^\star}(n_{q^\star}) - \mathbf{R}\mathbf{X}_p(m_p) - \mathbf{T} \right\| \right), \\
D_q(n_q) &= \min_{m_{p^\star} \in \{0,\dots,N\}} \left(\left\| \mathbf{X}_{p^\star}(m_{p^\star}) - \mathbf{R}^T(\mathbf{X}'_q(n_q) - \mathbf{T}) \right\| \right),
\end{aligned}
\qquad (2.16)
$$

where pixels $q^\star$ and $p^\star$ are the projections of $\mathbf{R}\mathbf{X}_p(m_p) + \mathbf{T}$ and $\mathbf{R}^T(\mathbf{X}'_q(n_q) - \mathbf{T})$ onto M_2 and M_1, respectively. The integer N is the maximum number of wrappings, determined by approximate knowledge on the scale of the scene.

To robustly handle with noise and occlusion, Choi and Lee [17] minimize the following MRF energy functions E_1 and E_2, instead of independently minimizing $D_p(m_p)$ and $D_q(m_q)$ at each pixel:

$$
\begin{aligned}
E_1 &= \sum_{p \in M_1} \hat{D}_p(m_p) + \sum_{(p,u)} V(m_p, m_u), \\
E_2 &= \sum_{q \in M_2} \hat{D}_q(n_q) + \sum_{(q,v)} V(n_q, n_v),
\end{aligned}
\qquad (2.17)
$$

where $\hat{D}_p(m_p)$ and $\hat{D}_q(n_q)$ are the data cost of assigning m_p and n_q to pixels p and q, respectively. Functions $V(m_p, m_u)$ and $V(n_q, n_v)$ determine the discontinuity cost of assigning (m_p, m_u) and (n_q, n_v) to pairs of adjacent pixels (p,u) and (q,v), respectively.

The data costs $\hat{D}_p(m_p)$ and $\hat{D}_q(n_q)$ are defined by truncating $D_p(m_p)$ and $D_q(n_q)$ to prevent their values from becoming too large, due to noise and occlusion:

$$\hat{D}_p(m_p) = \tau_\varepsilon(D_p(m_p)), \quad \hat{D}_q(n_q) = \tau_\varepsilon(D_q(n_q)), \qquad (2.18)$$

$$
\tau_\varepsilon(x) = \begin{cases} x, & \text{if } x < \varepsilon, \\ \varepsilon, & \text{otherwise,} \end{cases}
\qquad (2.19)
$$

where ε is a threshold proportional to the extrinsic calibration error of the system.

The function $V(m_p, m_u)$ is defined in a manner that preserves depth continuity between adjacent pixels. Choi and Lee [17] assume a pair of measured 3D points $\mathbf{X}_p$ and $\mathbf{X}_u$ to have been projected from close surface points if they are close to each other and have similar corrected amplitude values. The proximity is preserved by penalizing the pair of pixels if they have different numbers of wrappings:

$$
V(m_p, m_u) = \begin{cases} \frac{\lambda}{r_{pu}} \exp\left(-\frac{\Delta \mathbf{X}_{pu}^2}{2\sigma_{\mathbf{X}}^2}\right) \exp\left(-\frac{\Delta A_{pu}'^2}{2\sigma_{A'}^2}\right) & \text{if } \begin{cases} m_p \neq m_u & \text{and} \\ \Delta \mathbf{X}_{pu} < 0.5\, d_{\max}(f_1) \end{cases} \\ 0 & \text{otherwise.} \end{cases}
$$

where λ is a constant, $\Delta \mathbf{X}_{pu}^2 = \|\mathbf{X}_p - \mathbf{X}_u\|^2$, and $\Delta A_{pu}'^2 = \|A_p' - A_u'\|^2$. The variances $\sigma_{\mathbf{X}}^2$ and $\sigma_{A'}^2$ are adaptively determined. The positive scalar r_{pu} is the image coordinate distance between p and u for attenuation of the effect of less adjacent pixels. The function $V(n_q, n_v)$ is defined by analogy with $V(m_p, m_u)$.

Choi and Lee [17] minimize the MRF energies via the α-expansion algorithm [8], obtaining a pair of unwrapped depth maps. To enforce further consistency between the unwrapped depth maps, they iteratively update the MRF energy corresponding to a depth map, using the unwrapped depth of the other map, and perform the minimization until the consistency no longer increases. Figure 2.10(e) and (f) show examples of unwrapped depth maps, as obtained by the iterative optimizations. An alternative method for improving the depth accuracy using two ToF cameras is described in [11].

Methods	# Depth Maps	Cues	Approach	Maximum Range
Poppinga and Birk [93]	1	CA[a]	Thresholding	$2d_{\max}$
Choi *et al.* [18]	1	CA, DD[b]	Segmentation, MRF	$(N^d + 1)d_{\max}$
McClure *et al.* [83]	1	CA	Segmentation, Thresholding	$2d_{\max}$
Jutzi [65]	1	DD	Branch cuts, Integration	∞
Droeschel *et al.* [30]	1	DD	MRF, Integration	∞
Droeschel *et al.* [29]	2 (Multi-Freq.)	DD, DC[c]	MRF, Integration	∞
Payne *et al.* [92]	2 (Multi-Freq.)	DC	Hardware	$\frac{c}{2|f_1 - f_2|}$
Choi and Lee [17]	2 (Stereo)	DC	Stereo ToF, MRF	$(N + 1)d_{\max}$

[a] Corrected amplitude. [b] Depth discontinuity. [c] Depth consistency. [d] The maximum number of wrappings determined by the user.

Table 2.1 Summary of phase unwrapping methods

2.3.3 Discussion

Table 2.3.2 summarizes the phase unwrapping methods [93, 18, 83, 65, 30, 29, 92, 17] for ToF cameras. The last column of the table shows the extended maximum range, which can be theoretically achieved by the methods. The methods [65, 30, 29] based on the classical phase unwrapping methods [40, 46] deliver the widest maximum range. In [18, 17], the maximum number of wrappings can be determined by the user. It follows that the maximum range of the methods can also become sufficiently wide, by setting N to a large value. In practice, however, the limited illuminating power of commercially available ToF cameras prevents distant objects

from being precisely measured. This means that the phase values may be invalid, even if they can be unwrapped. In addition, the working environment may be physically confined. For the latter reason, Droeschel *et al.* [30, 29] limit the maximum range to $2d_{max}$.

2.4 Conclusions

Although the hardware system in [92] has not yet been established in commercially available ToF cameras, we believe that future ToF cameras will use such a frequency modulation technique for accurate and precise depth measurement. In addition, the phase unwrapping methods in [29, 17] are ready to be applied to a pair of depth maps acquired by such future ToF cameras, for robust estimation of the unwrapped depth values. We believe that a suitable combination of hardware and software systems will extend the maximum ToF range, up to a limit imposed by the illuminating power of the device.

Chapter 3
Calibration of Time-of-Flight Cameras

Abstract This chapter describes the metric calibration of a time-of-flight camera including the internal parameters, and lens-distortion. Once the camera has been calibrated, the 2D depth-image can be transformed into a range-map, which encodes the distance to the scene along each optical ray. It is convenient to use established calibration methods, which are based on images of a chequerboard pattern. The low-resolution of the amplitude image, however, makes it difficult to detect the board reliably. Heuristic detection methods, based on connected image-components, perform very poorly on this data. An alternative, geometrically-principled method is introduced here, based on the Hough transform. The Hough method is compared to the standard OpenCV board-detection routine, by application to several hundred time-of-flight images. It is shown that the new method detects significantly more calibration boards, over a greater variety of poses, without any significant loss of accuracy.

3.1 Introduction

Time-of-flight cameras can, in principle, be modelled and calibrated as pinhole devices. For example, if a known chequerboard pattern is detected in a sufficient variety of poses, then the internal and external camera parameters can be estimated by standard routines [124, 55]. This chapter will briefly review the underlying calibration model, before addressing the problem of chequerboard detection in detail. The latter is the chief obstacle to the use of existing calibration software, owing to the low resolution of the ToF images.

3.2 Camera Model

If the scene-coordinates of a point are $(X,Y,Z)^\top$, then the pinhole-projection can be expressed as $(x_p, y_p, 1)^\top \simeq \boldsymbol{R}(X,Y,Z)^\top + \boldsymbol{T}$ where the rotation matrix $\boldsymbol{R}$ and translation $\boldsymbol{T}$ account for the pose of the camera. The observed pixel-coordinates of the point are then modelled as

$$\begin{pmatrix} x \\ y \\ 1 \end{pmatrix} = \begin{pmatrix} fs_x & fs_\theta & x_0 \\ 0 & fs_y & y_0 \\ 0 & 0 & 1 \end{pmatrix} \begin{pmatrix} x_d \\ y_d \\ 1 \end{pmatrix} \tag{3.1}$$

where $(x_d, y_d)^\top$ results from lens-distortion of $(x_p, y_p)^\top$. The parameter f is the focal-length, (s_x, s_y) are the pixel-scales, and s_θ is the skew-factor [55], which is assumed to be zero here. The lens distortion may be modelled by a radial part d_1 and tangential part $\boldsymbol{d}_2$, so that

$$\begin{pmatrix} x_d \\ y_d \end{pmatrix} = d_1(r) \begin{pmatrix} x_p \\ y_p \end{pmatrix} + \boldsymbol{d}_2(x_p, y_p) \quad \text{where} \quad r = \sqrt{x_p^2 + y_p^2} \tag{3.2}$$

is the radial coordinate. The actual distortion functions are polynomials of the form

$$d_1(r) = 1 + a_1 r^2 + a_2 r^4 \quad \text{and} \quad \boldsymbol{d}_2(x,y) = \begin{pmatrix} 2xy & r^2 + 2x^2 \\ r^2 + 2y^2 & 2xy \end{pmatrix} \begin{pmatrix} a_3 \\ a_4 \end{pmatrix}. \tag{3.3}$$

The coefficients (a_1, a_2, a_3, a_4) must be estimated along with the other internal parameters (f, s_x, s_y) and (x_0, y_0) in 3.1. The standard estimation procedure is based on the projection of a known chequerboard pattern, which is viewed in many different positions and orientations. The external parameters $(\boldsymbol{R}, \boldsymbol{T})$, as well as the internal parameters can then be estimated as described by Zhang [124, 9], for example.

3.3 Board Detection

It is possible to find the chequerboard vertices, in ordinary images, by first detecting image-corners [53], and subsequently imposing global constraints on their arrangement [72, 114, 9]. This approach, however, is not reliable for low resolution images (e.g. in the range 100–500 px^2) because the local image-structure is disrupted by sampling artefacts, as shown in fig. 3.1. Furthermore, these artefacts become worse as the board is viewed in distant and slanted positions, which are essential for high quality calibration [23]. This is a serious obstacle for the application of existing calibration methods to new types of camera. For example, the amplitude signal from a typical time-of-flight camera [80] resembles an ordinary greyscale image, but is of very low spatial resolution (e.g. 176×144), as well as being noisy. It is, nonetheless,

necessary to calibrate these devices, in order to combine them with ordinary colour cameras, for 3-D modelling and rendering [33, 101, 125, 51, 70, 71, 52].

The method described here is based on the Hough transform [62], and effectively fits a *global* model to the lines in the chequerboard pattern. This process is much less sensitive to the resolution of the data, for two reasons. Firstly, information is integrated across the source image, because each vertex is obtained from the intersection of two fitted lines. Secondly, the structure of a straight edge is inherently simpler than that of a corner feature. However, for this approach to be viable, it is assumed that any lens distortion has been pre-calibrated, so that the images of the pattern contain straight lines. This is not a serious restriction, for two reasons. Firstly, it is relatively easy to find enough boards (by any heuristic method) to get adequate estimates of the internal and lens parameters. Indeed, this can be done from a single image, in principle [47]. The harder problems of reconstruction and relative orientation can then be addressed after adding the newly detected boards, ending with a bundle-adjustment that also refines the initial internal parameters. Secondly, the ToF devices used here have fixed lenses, which are sealed inside the camera body. This means that the internal parameters from previous calibrations can be re-used.

Another Hough-method for chequerboard detection has been presented by de la Escalera and Armingol [24]. Their algorithm involves a *polar* Hough transform of all high-gradient points in the image. This results in an array that contains a peak for each line in the pattern. It is not, however, straightforward to extract these peaks, because their location depends strongly on the unknown orientation of the image-lines. Hence all local maxima are detected by morphological operations, and a second Hough transform is applied to the resulting data in [24]. The true peaks will form two collinear sets in the first transform (cf. sec. 3.3.5), and so the final task is to detect two peaks in the second Hough transform [110].

The method described in this chapter is quite different. It makes use of the gradient *orientation* as well as magnitude at each point, in order to establish an axis-aligned coordinate system for each image of the pattern. Separate Hough transforms are then performed in the x and y directions of the local coordinate system. By construction, the slope-coordinate of any line is close to zero in the corresponding *Cartesian* Hough transform. This means that, on average, the peaks occur along a fixed axis of each transform, and can be detected by a simple sweep-line procedure. Furthermore, the known $\ell \times m$ structure of the grid makes it easy to identify the optimal sweep-line in each transform. Finally, the two optimal sweep-lines map directly back to pencils of ℓ and m lines in the original image, owing to the Cartesian nature of the transform. The principle of the method is shown in fig. 3.1.

It should be noted that the method presented here was designed specifically for use with ToF cameras. For this reason, the *range*, as well as intensity data is used to help segment the image in sec. 3.3.2. However, this step could easily be replaced with an appropriate background subtraction procedure [9], in which case the new method could be applied to ordinary RGB images. Camera calibration is typically performed under controlled illumination conditions, and so there would be no need for a dynamic background model.

3.3.1 Overview

The new method is described in section 3.3; preprocessing and segmentation are explained in sections 3.3.2 and 3.3.3 respectively, while sec. 3.3.4 describes the geometric representation of the data. The necessary Hough transforms are defined in sec. 3.3.5, and analyzed in sec. 3.3.6.

Matrices and vectors will be written in bold, e.g. $\boldsymbol{M}$, $\boldsymbol{v}$, and the Euclidean length of $\boldsymbol{v}$ will be written $|\boldsymbol{v}|$. Equality up to an overall nonzero-scaling will be written $\boldsymbol{v} \simeq \boldsymbol{u}$. Image-points and lines will be represented in homogeneous coordinates [55], with $\boldsymbol{p} \simeq (x, y, 1)^\top$ and $\boldsymbol{l} \simeq (\alpha, \beta, \gamma)$, such that $\boldsymbol{lp} = 0$ if $\boldsymbol{l}$ passes through $\boldsymbol{p}$. The intersection-point of two lines can be obtained from the cross-product $(\boldsymbol{l} \times \boldsymbol{m})^\top$. An assignment from variable a to variable b will be written $b \leftarrow a$. It will be convenient, for consistency with the pseudo-code listings, to use the notation $(m : n)$ for the sequence of integers from m to n inclusive. The 'null' symbol $\varnothing$ will be used to denote undefined or unused variables.

The method described here refers to a chequerboard of $(\ell + 1) \times (m + 1)$ squares, with $\ell < m$. It follows that the *internal* vertices of the pattern are imaged as the ℓm intersection-points

$$\boldsymbol{v}_{ij} = \boldsymbol{l}_i \times \boldsymbol{m}_j \quad \text{where} \quad \boldsymbol{l}_i \in \mathscr{L} \text{ for } i = 1 : \ell \quad \text{and} \quad \boldsymbol{m}_j \in \mathscr{M} \text{ for } j = 1 : m. \quad (3.4)$$

The sets $\mathscr{L}$ and $\mathscr{M}$ are *pencils*, meaning that $\boldsymbol{l}_i$ all intersect at a point $\boldsymbol{p}$, while $\boldsymbol{m}_j$ all intersect at a point $\boldsymbol{q}$. Note that $\boldsymbol{p}$ and $\boldsymbol{q}$ are the *vanishing points* of the grid-lines, which may be at infinity in the images.

It is assumed that the imaging device, such as a ToF camera, provides a range map D_{ij}, containing distances from the optical centre, as well as a luminance-like amplitude map A_{ij}. The images D and A are both of size $I \times J$. All images must be undistorted, as described in the section 3.3.

3.3.2 Preprocessing

The amplitude image A is roughly segmented, by discarding all pixels that correspond to very near or far points. This gives a new image B, which typically contains the board, plus the person holding it:

$$B_{ij} \leftarrow A_{ij} \text{ if } d_0 < D_{ij} < d_1, \qquad B_{ij} \leftarrow \varnothing \text{ otherwise.} \qquad (3.5)$$

The near-limit d_0 is determined by the closest position for which the board remains fully inside the field-of-view of the camera. The far-limit d_1 is typically set to a value just closer than the far wall of the scene. These parameters need only be set approximately, provided that the interval $d_1 - d_0$ covers the possible positions of the calibration board.
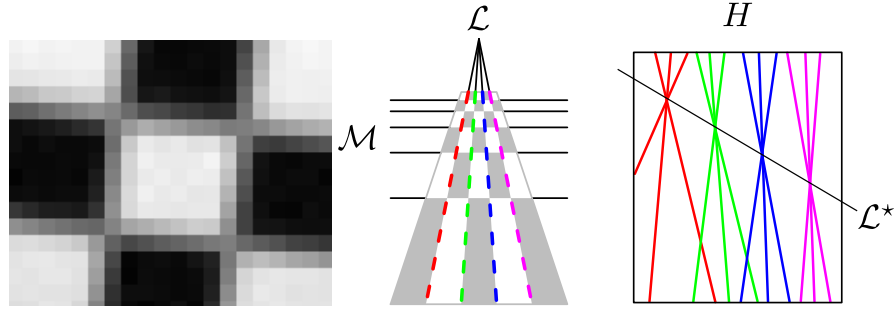
Fig. 3.1 **Left:** Example chequers from a ToF amplitude image. Note the variable appearance of the four junctions at this resolution, e.g. '×' at lower-left vs. '+' at top-right. **Middle:** A perspective image of a calibration grid is represented by line-pencils $\mathcal{L}$ and $\mathcal{M}$, which intersect at the $\ell \times m = 20$ internal vertices of this board. Strong image-gradients are detected along the dashed lines. **Right:** The Hough transform H of the image-points associated with $\mathcal{L}$. Each high-gradient point maps to a line, such that there is a pencil in H for each set of edge-points. The line $\mathcal{L}^\star$, which passes through the $\ell = 4$ Hough-vertices, is the Hough representation of the image-pencil $\mathcal{L}$.

It is useful to perform a morphological erosion operation at this stage, in order to partially remove the perimeter of the board. In particular, if the physical edge of the board is not white, then it will give rise to irrelevant image-gradients. The erosion radius need only be set approximately, assuming that there is a reasonable amount of white-space around the chessboard pattern. The gradient of the remaining amplitude image is now computed, using the simple kernel $\Delta = (-1/2, 0, 1/2)$. The horizontal and vertical components are

$$
\begin{aligned}
\xi_{ij} &\leftarrow (\Delta \star B)_{ij} \\
&= \rho \cos \theta
\end{aligned}
\quad \text{and} \quad
\begin{aligned}
\eta_{ij} &\leftarrow (\Delta^\top \star B)_{ij} \\
&= \rho \sin \theta
\end{aligned}
\tag{3.6}
$$

where $\star$ indicates convolution. No pre-smoothing of the image is performed, owing to the low spatial resolution of the data.

3.3.3 Gradient Clustering

The objective of this section is to assign each gradient vector (ξ_{ij}, η_{ij}) to one of three classes, with labels $\kappa_{ij} \in \{\lambda, \mu, \varnothing\}$. If $\kappa_{ij} = \lambda$ then pixel (i, j) is on one of the lines in $\mathcal{L}$, and (ξ_{ij}, η_{ij}) is perpendicular to that line. If $\kappa_{ij} = \mu$, then the analogous relations hold with respect to $\mathcal{M}$. If $\kappa_{ij} = \varnothing$ then pixel (i, j) does not lie on any of the lines.

The gradient distribution, after the initial segmentation, will contain two elongated clusters through the origin, which will be approximately orthogonal. Each *cluster* corresponds to a gradient orientation (mod π), while each *end* of a cluster corresponds to a gradient polarity (black/white vs. white/black). The distribu-
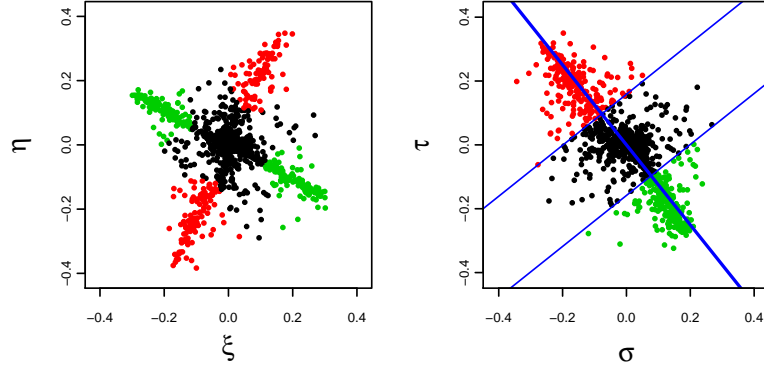
Fig. 3.2 Left: the cruciform distribution of image gradients, due to black/white and white/black transitions at each orientation, would be difficult to segment in terms of horizontal and vertical components (ξ, η). Right: the same distribution is easily segmented, by eigen-analysis, in the double-angle representation (3.7). The red and green labels are applied to the corresponding points in the original distribution, on the left.

tion is best analyzed after a double-angle mapping [49], which will be expressed as $(\xi, \eta) \mapsto (\sigma, \tau)$. This mapping results in a *single* elongated cluster, each *end* of which corresponds to a gradient orientation (mod π), as shown in fig. 3.2. The double-angle coordinates are obtained by applying the trigonometric identities $\cos(2\theta) = \cos^2 \theta - \sin^2 \theta$ and $\sin(2\theta) = 2 \sin \theta \cos \theta$ to the gradients (3.6), so that

$$\sigma_{ij} \leftarrow \frac{1}{\rho_{ij}} \left(\xi_{ij}^2 - \eta_{ij}^2 \right) \quad \text{and} \quad \tau_{ij} \leftarrow \frac{2}{\rho_{ij}} \xi_{ij} \eta_{ij} \quad \text{where} \quad \rho_{ij} = \sqrt{\xi_{ij}^2 + \eta_{ij}^2} \quad (3.7)$$

for all points at which the magnitude ρ_{ij} is above machine precision. Let the first unit-eigenvector of the (σ, τ) covariance matrix be $\big(\cos(2\phi), \sin(2\phi) \big)$, which is written in this way so that the angle ϕ can be interpreted in the original image. The cluster-membership is now defined by the projection

$$\pi_{ij} = \big(\sigma_{ij}, \tau_{ij} \big) \cdot \big(\cos(2\phi), \sin(2\phi) \big) \tag{3.8}$$

of the data onto this axis. The gradient-vectors (ξ_{ij}, η_{ij}) that project to either end of the axis are labelled as follows:

$$\kappa_{ij} \leftarrow \begin{cases} \lambda & \text{if } \pi_{ij} \geq \rho_{\min} \\ \mu & \text{if } \pi_{ij} \leq -\rho_{\min} \\ \varnothing & \text{otherwise.} \end{cases} \tag{3.9}$$

Strong gradients that are not aligned with either axis of the board are assigned to $\varnothing$, as are all weak gradients. It should be noted that the respective *identity* of classes λ

and μ has not yet been determined; the correspondence $\{\lambda,\mu\} \Leftrightarrow \{\mathcal{L},\mathcal{M}\}$ between labels and pencils will be resolved in section 3.3.6.

3.3.4 Local Coordinates

A coordinate system will now be constructed for each image of the board. The very low amplitudes $B_{ij} \approx 0$ of the *black* squares tend to be characteristic of the board (i.e. $B_{ij} \gg 0$ for both the white squares and for the rest of B). Hence a good estimate of the centre can be obtained by normalizing the amplitude image to the range $[0,1]$ and then computing a centroid using weights $(1 - B_{ij})$. The centroid, together with the angle ϕ from (3.8) defines the Euclidean transformation $(x,y,1)^\top = E(j,i,1)^\top$ into local coordinates, centred on and aligned with the board.

Let $(x_\kappa, y_\kappa, 1)^\top$ be the coordinates of point (i,j), after transformation by E, with the label κ inherited from κ_{ij}, and let $\mathcal{L}'$ and $\mathcal{M}'$ correspond to $\mathcal{L}$ and $\mathcal{M}$ in the new coordinate system. Now, by construction, any labelled point is hypothesized to be part of $\mathcal{L}'$ or $\mathcal{M}'$, such that that $l'(x_\lambda, y_\lambda, 1)^\top = 0$ or $m'(x_\mu, y_\mu, 1)^\top = 0$, where l' and m' are the local coordinates of the relevant lines l and m, respectively. These lines can be expressed as

$$l' \simeq (-1, \beta_\lambda, \alpha_\lambda) \quad \text{and} \quad m' \simeq (\beta_\mu, -1, \alpha_\mu) \tag{3.10}$$

with inhomogeneous forms $x_\lambda = \alpha_\lambda + \beta_\lambda y_\lambda$ and $y_\mu = \alpha_\mu + \beta_\mu x_\mu$, such that the slopes $|\beta_\kappa| \ll 1$ are *bounded*. In other words, the board is axis-aligned in local coordinates, and the perspective-induced deviation of any line is less than $45°$.

3.3.5 Hough Transform

The Hough transform, in the form used here, maps *points* from the image to *lines* in the transform. In particular, points along a line are mapped to lines through a point. This duality between collinearity and concurrency suggests that a *pencil* of n image-lines will be mapped to a *line* of n transform points, as in fig. 3.1.

The transform is implemented as a 2-D histogram $H(u,v)$, with horizontal and vertical coordinates $u \in [0, u_1]$ and $v \in [0, v_1]$. The point $(u_0, v_0) = \frac{1}{2}(u_1, v_1)$ is the centre of the transform array. Two transforms, H_λ and H_μ, will be performed, for points labelled λ and μ, respectively. The Hough variables are related to the image coordinates in the following way:

$$u_\kappa(x,y,v) = \begin{cases} u(x,y,v) & \text{if } \kappa = \lambda \\ u(y,x,v) & \text{if } \kappa = \mu \end{cases} \quad \text{where} \quad u(x,y,v) = u_0 + x - y(v - v_0). \tag{3.11}$$

Here $u(x,y,v)$ is the u-coordinate of a line (parameterized by v), which is the Hough-transform of an image-point (x,y). The Hough intersection point $(u^{\star}_{\kappa}, v^{\star}_{\kappa})$ is found by taking two points (x,y) and (x',y'), and solving $u_{\lambda}(x,y,v) = u_{\lambda}(x',y',v)$, with x_{λ} and x'_{λ} substituted according to (3.10). The same coordinates are obtained by solving $u_{\mu}(x,y,v) = u_{\mu}(x',y',v)$, and so the result can be expressed as

$$u^{\star}_{\kappa} = u_0 + \alpha_{\kappa} \quad \text{and} \quad v^{\star}_{\kappa} = v_0 + \beta_{\kappa} \tag{3.12}$$

with labels $\kappa \in \{\lambda, \mu\}$ as usual. A peak at $(u^{\star}_{\kappa}, v^{\star}_{\kappa})$ evidently maps to a line of intercept $u^{\star}_{\kappa} - u_0$ and slope $v^{\star}_{\kappa} - v_0$. Note that if the perspective distortion in the images is small, then $\beta_{\kappa} \approx 0$, and all intersection points lie along the horizontal midline (u, v_0) of the corresponding transform. The Hough intersection point $(u^{\star}_{\kappa}, v^{\star}_{\kappa})$ can be used to construct an image-line l' or m', by combining (3.12) with (3.10), resulting in

$$l' \leftarrow (-1, \, v^{\star}_{\lambda} - v_0, \, u^{\star}_{\lambda} - u_0) \quad \text{and} \quad m' \leftarrow (v^{\star}_{\mu} - v_0, \, -1, \, u^{\star}_{\mu} - u_0). \tag{3.13}$$

The transformation of these line-vectors, back to the original image coordinates, is given by the inverse-transpose of the matrix E, described in sec. 3.3.4.

The two Hough transforms are computed by the procedure in fig. 3.3. Let H_{κ} refer to H_{λ} or H_{μ}, according to the label κ of the ij-th point (x,y). For each accepted point, the corresponding line (3.11) intersects the top and bottom of the (u,v) array at points $(s,0)$ and (t,v_1) respectively. The resulting segment, of length w_1, is evenly sampled, and H_{κ} is incremented at each of the constituent points. The procedure in fig. 3.3 makes use of the following functions. Firstly, $\text{interp}_{\alpha}(p,q)$, with $\alpha \in [0,1]$, returns the affine combination $(1-\alpha)p + \alpha q$. Secondly, the 'accumulation' $H \oplus (u,v)$ is equal to $H(u,v) \leftarrow H(u,v) + 1$ if u and v are integers. In the general case, however, the four pixels closest to (u,v) are updated by the corresponding bilinear-interpolation weights (which sum to one).


```
for (i, j) in (0 : i_1) × (0 : j_1)
    if κ_ij ≠ ∅
        (x, y, κ) ← (x_ij, y_ij, κ_ij)
        s ← u_κ(x, y, 0)
        t ← u_κ(x, y, v_1)
        w_1 ← |(t, v_1) − (s, 0)|
        for w in (0 : floor(w_1))
            H_κ ← H_κ ⊕ interp((s,0), (t,v_1))
                                    w/w_1
        end
    endif
end
```
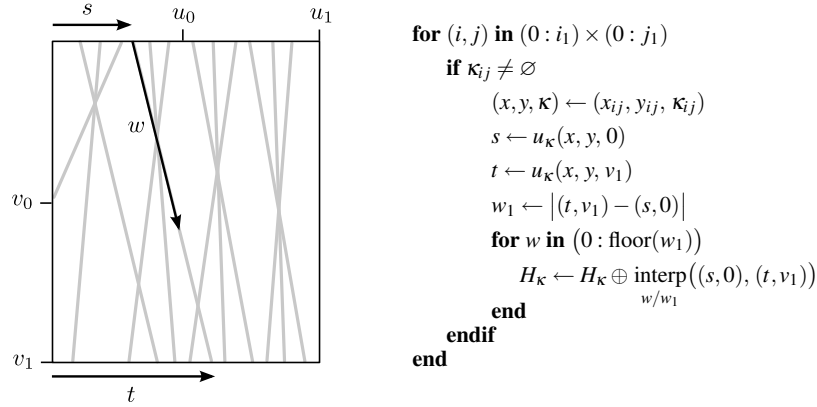
**Fig. 3.3** Hough transform. Each gradient pixel (x,y) labelled $\kappa \in \{\lambda, \mu\}$ maps to a line $u_{\kappa}(x,y,v)$ in transform H_{κ}. The operators $H \oplus p$ and $\text{interp}_{\alpha}(p,q)$ perform accumulation and linear interpolation, respectively. See section 3.3.5 for details.

3.3.6 Hough Analysis

The local coordinates defined in sec. 3.3.4 ensure that the two Hough transforms H_λ and H_μ have the same characteristic structure. Hence the subscripts λ and μ will be suppressed for the moment. Recall that each Hough cluster corresponds to a line in the image space, and that a collinear set of Hough clusters corresponds to a pencil of lines in the image space, as in fig 3.1. It follows that all lines in a pencil can be detected simultaneously, by *sweeping* the Hough space H with a line that cuts a 1-D slice through the histogram.

Recall from section 3.3.5 that the Hough peaks are most likely to lie along a horizontal axis (corresponding to a fronto-parallel pose of the board). Hence a suitable parameterization of the sweep-line is to vary one endpoint $(0, s)$ along the left edge, while varying the other endpoint (u_1, t) along the right edge, as in fig. 3.4. This scheme has the desirable property of sampling more densely around the midline (u, v_0). It is also useful to note that the sweep-line parameters s and t can be used to represent the apex of the corresponding pencil. The local coordinates p' and q' are $p' \simeq \left(l'_s \times l'_t \right)^\top$ and $q' \simeq \left(m'_s \times m'_t \right)^\top$ where l'_s and l'_t are obtained from (3.10) by setting $(u^\star_\lambda, v^\star_\lambda)$ to $(0, s)$ and (u_1, t) respectively, and similarly for m'_s and m'_t.

The procedure shown in fig. 3.4 is used to analyze the Hough transform. The sweep-line with parameters s and t has the form of a 1-D histogram $h^{st}_\kappa(w)$. The integer index $w \in (0 : w_1)$ is equal to the Euclidean distance $|(u, v) - (0, s)|$ along the sweep-line. The procedure shown in fig. 3.4 makes further use of the interpolation operator that was defined in section 3.3.5. Each sweep-line $h^{st}_\kappa(w)$, constructed by the above process, will contain a number of isolated clusters: $\text{count}(h^{st}_\kappa) \geq 1$. The clusters are simply defined as runs of non-zero values in $h^{st}_\kappa(w)$. The existence of separating zeros is, in practice, highly reliable when the sweep-line is close to the true solution. This is simply because the Hough data was thresholded in (3.9), and strong gradients are not found *inside* the chessboard squares. The representation of the clusters, and subsequent evaluation of each sweep-line, will now be described.

The label κ and endpoint parameters s and t will be suppressed, in the following analysis of a single sweep-line, for clarity. Hence let $w \in (a_c : b_c)$ be the interval that contains the c-th cluster in $h(w)$. The score and location of this cluster are defined as the mean value and centroid, respectively:

$$\text{score}_c(h) = \frac{\sum_{w=a_c}^{b_c} h(w)}{1 + b_c - a_c} \quad \text{and} \quad w_c = a_c + \frac{\sum_{w=a_c}^{b_c} h(w)\, w}{\sum_{w=a_c}^{b_c} h(w)} \qquad (3.14)$$

More sophisticated definitions are possible, based on quadratic interpolation around each peak. However, the mean and centroid give similar results in practice. A total score must now be assigned to the sweep-line, based on the scores of the constituent clusters. If n peaks are sought, then the total score is the sum of the highest n cluster-scores. But if there are fewer than n clusters in $h(w)$, then this cannot be a solution, and the score is zero:

```
for (s,t) in (0 : v₁) × (0 : v₁)
    w₁ = |(u₁,t) − (0,s)|
    for w in (0 : floor(w₁))
        (u,v) ← interp((0,s), (u₁,t))
                      w/w₁
        h_λ^st(w) ← H_λ(u,v)
        h_μ^st(w) ← H_μ(u,v)
    end
end
```
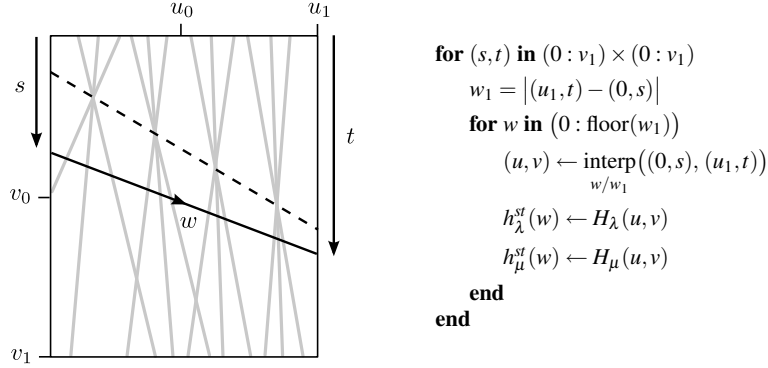
Fig. 3.4 A line $h_\kappa^{st}(w)$, with end-points $(0,s)$ and (u_1,t), is swept through each Hough transform H_κ. A total of $v_1 \times v_1$ 1-D histograms $h_\kappa^{st}(w)$ are computed in this way. See section 3.3.6 for details.

$$\Sigma^n(h) = \begin{cases} \sum_{i=1}^{n} \underset{c(i)}{\text{score}}(h) & \text{if } n \leq \text{count}(h) \\ 0 & \text{otherwise} \end{cases} \qquad (3.15)$$

where $c(i)$ is the index of the i-th highest-scoring cluster. The optimal clusters are those in the sweep-line that maximizes (3.15). Now, restoring the full notation, the score of the optimal sweep-line in the transform H_κ is

$$\Sigma_\kappa^n \leftarrow \max_{s,t} \underset{n}{\text{score}}(h_\kappa^{st}). \qquad (3.16)$$

One problem remains: it is not known in advance whether there should be ℓ peaks in H_λ and m in H_μ, or vice versa. Hence all four combinations, $\Sigma_\lambda^\ell, \Sigma_\mu^m, \Sigma_\mu^\ell, \Sigma_\lambda^m$ are computed. The ambiguity between pencils $(\mathcal{L},\mathcal{M})$ and labels (λ,μ) can then be resolved, by picking the solution with the highest *total* score:

$$(\mathcal{L},\mathcal{M}) \Leftrightarrow \begin{cases} (\lambda,\mu) & \text{if } \Sigma_\lambda^\ell + \Sigma_\mu^m > \Sigma_\mu^\ell + \Sigma_\lambda^m \\ (\mu,\lambda) & \text{otherwise.} \end{cases} \qquad (3.17)$$

Here, for example, $(\mathcal{L},\mathcal{M}) \Leftrightarrow (\lambda,\mu)$ means that there is a pencil of ℓ lines in H_λ and a pencil of m lines in H_μ. The procedure in (3.17) is based on the fact that the complete solution must consist of $\ell+m$ clusters. Suppose, for example, that there are ℓ good clusters in H_λ, and m good clusters in H_μ. Of course there are also ℓ good clusters in H_μ, because $\ell < m$ by definition. However, if only ℓ clusters are taken from H_μ, then an additional $m-\ell$ weak or non-existent clusters must be found in H_λ, and so the total score $\Sigma_\mu^\ell + \Sigma_\lambda^m$ would not be maximal.

It is straightforward, for each centroid w_c in the optimal sweep-line h_κ^{st}, to compute the 2-D Hough coordinates

$$\left(u_\kappa^\star, v_\kappa^\star\right) \leftarrow \underset{w_c/w_1}{\text{interp}}\big((0,s),\,(u_1,t)\big) \tag{3.18}$$

where w_1 is the length of the sweep-line, as in fig. 3.4. Each of the resulting ℓm points are mapped to image-lines, according to (3.13). The vertices $\mathbf{v}_{ij}$ are then be computed from (3.4). The order of intersections along each line is preserved by the Hough transform, and so the ij indexing is automatically consistent.

The final decision-function is based on the observation that cross-ratios of distances between consecutive vertices should be near unity (because the images are projectively related to a regular grid). In practice it suffices to consider simple ratios, taken along the first and last edge of each pencil. If all ratios are below a given threshold, then the estimate is accepted. This threshold was fixed once and for all, such that no false-positive detections (which are unacceptable for calibration purposes) were made, across *all* data-sets.

3.3.7 Example Results

The method was tested on five multi-camera data-sets, and compared to the standard OpenCV detector. Both the OpenCV and Hough detections were refined by the OpenCV subpixel routine, which adjusts the given point to minimize the discrepancy with the image-gradient around the chequerboard corner [9, 23]. Table 3.1 shows the number of true-positive detections by each method, as well as the number of detections common to both methods. The geometric error is the discrepancy from the 'ideal' board, after fitting the latter by the optimal (DLT+LM) homography [55]. This is by far the most useful measure, as it is directly related to the role of the detected vertices in subsequent calibration algorithms (and also has a simple interpretation in pixel-units). The photometric error is the gradient residual, as described in sec. 3.3.6. This measure is worth considering, because it is the criterion minimized by the subpixel optimization, but it is less interesting than the geometric error.

The Hough method detects 35% more boards than the OpenCV method, on average. There is also a slight reduction in average geometric error, even though the additional boards were more problematic to detect. The results should not be surprising, because the new method uses a very strong model of the global board-geometry (in fairness, it also benefits from the depth-thresholding in 3.3.2). There were zero false-positive detections (100% precision), as explained in sec. 3.3.6. The number of true-negatives is not useful here, because it depends largely on the configuration of the cameras (i.e. how many images show the back of the board). The false-negatives do not provide a very useful measure either, because they depend on an arbitrary judgement about which of the very foreshortened boards 'ought' to have been detected (i.e. whether an edge-on board is 'in' the image or not). Some example detections are shown in figs. 3.5–3.7, including some difficult cases.

	Number detected			Geometric error		Photometric error	
Set / Camera	OCV	HT	Both	OCV	HT	OCV	HT
1 / 1	19	34	13	0.2263	0.1506	0.0610	0.0782
1 / 2	22	34	14	0.1819	0.1448	0.0294	0.0360
1 / 3	46	33	20	0.1016	0.0968	0.0578	0.0695
1 / 4	26	42	20	0.2044	0.1593	0.0583	0.0705
2 / 1	15	27	09	0.0681	0.0800	0.0422	0.0372
2 / 2	26	21	16	0.0939	0.0979	0.0579	0.0523
2 / 3	25	37	20	0.0874	0.0882	0.0271	0.0254
3 / 1	14	26	11	0.1003	0.0983	0.0525	0.0956
3 / 2	10	38	10	0.0832	0.1011	0.0952	0.1057
3 / 3	25	41	21	0.1345	0.1366	0.0569	0.0454
3 / 4	18	23	10	0.1071	0.1053	0.0532	0.0656
4 / 1	16	21	14	0.0841	0.0874	0.0458	0.0526
4 / 2	45	53	29	0.0748	0.0750	0.0729	0.0743
4 / 3	26	42	15	0.0954	0.0988	0.0528	0.0918
5 / 1	25	37	18	0.0903	0.0876	0.0391	0.0567
5 / 2	20	20	08	0.2125	0.1666	0.0472	0.0759
5 / 3	39	36	24	0.0699	0.0771	0.0713	0.0785
5 / 4	34	35	19	0.1057	0.1015	0.0519	0.0528
6 / 1	29	36	20	0.1130	0.1203	0.0421	0.0472
6 / 2	35	60	26	0.0798	0.0803	0.0785	0.1067
Mean:	25.75	34.8	16.85	0.1157	0.1077	0.0547	0.0659

Table 3.1 Results over six multi-ToF camera-setups. Total detections for the OpenCV (515) vs. Hough Transform (696) method are shown, as well as the accuracy of the estimates. Geometric error is in pixels. The chief conclusion is that the HT method detects 35% more boards, and slightly reduces the average geometric error.
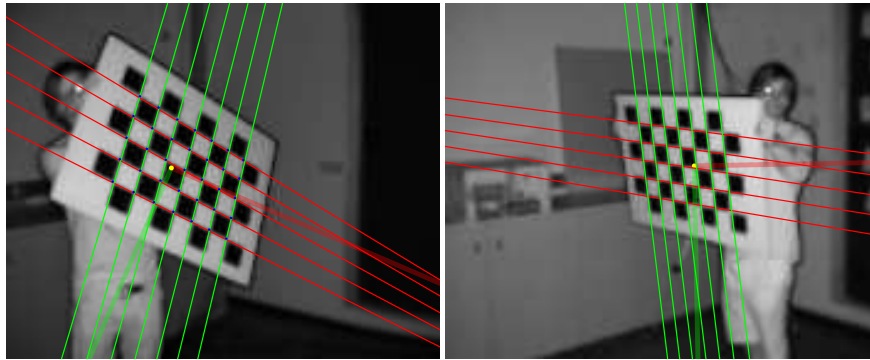
Fig. 3.5 Example detections in 176×144 ToF amplitude images. The yellow dot (one-pixel radius) is the estimated centroid of the board, and the attached thick translucent lines are the estimated axes. The board on the right, which is relatively distant and slanted, was not detected by OpenCV.

3.4 Conclusions

A new method for the automatic detection of calibration grids in time-of-flight images has been described. The method is based on careful reasoning about the
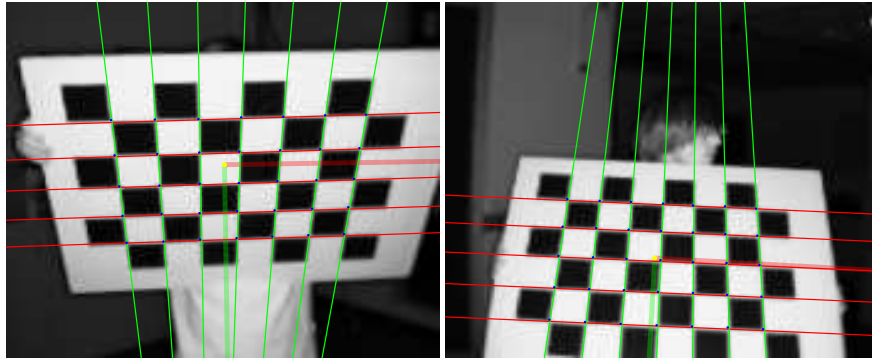
Fig. 3.6 Example detections (cf. fig. 3.5) showing significant perspective effects.
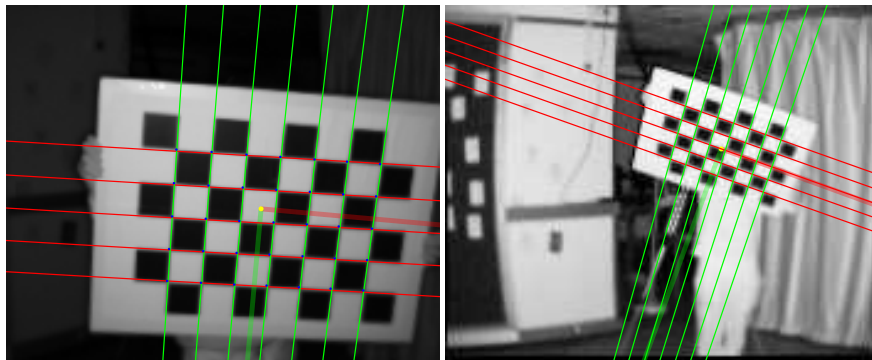
Fig. 3.7 Example detections (cf. fig. 3.5) showing significant scale changes. The board on the right, which is in an image that shows background clutter and lens distortion, was not detected by OpenCV.

global geometric structure of the board, before and after perspective projection. The method detects many more boards than existing heuristic approaches, which results in a larger and more complete data-set for subsequent calibration algorithms. Future work will investigate the possibility of making a global refinement of the pencils, in the geometric parameterization, by minimizing a photometric cost-function.

Chapter 4
Alignment of Time-of-Flight and Stereoscopic Data

Abstract An approximately Euclidean representation of the visible scene can be obtained directly from a time-of-flight camera. An uncalibrated binocular system, in contrast, gives only a projective reconstruction of the scene. This chapter analyzes the geometric mapping between the two representations, without requiring an intermediate calibration of the binocular system. The mapping can be found by either of two new methods, one of which requires point-correspondences between the range and colour cameras, and one of which does not. It is shown that these methods can be used to reproject the range data into the binocular images, which makes it possible to associate high-resolution colour and texture with each point in the Euclidean representation. The extension of these methods to multiple time-of-flight system is demonstrated, and the associated problems are examined. An evaluation metric, which distinguishes calibration error from combined calibration and depth error, is developed. This metric is used to evaluate a system that is based on three time-of-flight cameras.

4.1 Introduction

It was shown in the preceding chapter that time-of-flight cameras can be geometrically calibrated by standard methods. This means that each pixel records an estimate of the scene-distance (range) along the corresponding ray, according to the principles described in chapter 1. The 3-D structure of a scene can also be reconstructed from two or more ordinary images, via the *parallax* between corresponding image points. There are many advantages to be gained by combining the range and parallax data. Most obviously, each point in a parallax-based reconstruction can be mapped back into the original images, from which colour and texture can be obtained. Parallax-based reconstructions are, however, difficult to obtain, owing to the difficulty of putting the image points into correspondence. Indeed, it may be impossible to find any correspondences in untextured regions. Furthermore, if a Euclidean reconstruction is required, then the cameras must be calibrated. The accuracy of the

57

resulting reconstruction will also tend to decrease with the distance of the scene from the cameras [111].

The range data, on the other hand, are often very noisy (and, for very scattering surfaces, incomplete), as described in chapter 1. The spatial resolution of current TOF sensors is relatively low, the depth-range is limited, and the luminance signal may be unusable for rendering. It should also be recalled that time-of-flight cameras of the type used here [80] cannot be used in outdoor lighting conditions. These considerations lead to the idea of a *mixed* colour and time-of-flight system [78]. Such a system could, in principle, be used to make high-resolution Euclidean reconstructions, with full photometric information [71]. The task of camera calibration would be simplified by the TOF camera, while the visual quality of the reconstruction would be ensured by the colour cameras.
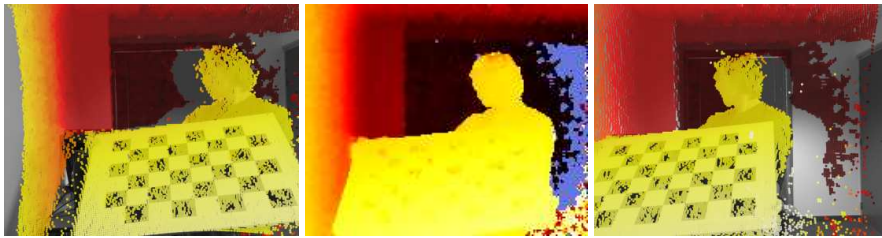
Fig. 4.1 The central panel shows a range image, colour-coded according to depth (the blue region is beyond the far-limit of the device). The left and right cameras were aligned to the TOF system, using the methods described here. Each 3-D range-pixel is reprojected into the high-resolution left and right images (untinted regions were occluded, or otherwise missing, from the range images). Note the large difference between the binocular views, which would be problematic for dense stereo-matching algorithms. It can also be seen that the TOF information is noisy, and of low resolution.

In order to make full use of a mixed range/parallax system, it is necessary to find the exact geometric relationship between the different devices. In particular, the reprojection of the TOF data, into the colour images, must be obtained. This chapter is concerned with the estimation of these geometric relationships. Specifically, the aim is to align the range and parallax reconstructions, by a suitable 3-D transformation. The alignment problem has been addressed previously, by fully calibrating the binocular system, and then aligning the two reconstructions by a rigid transformation [58, 122, 125, 33]. This approach can be extended in two ways. Firstly, it is possible to optimize over an explicit parameterization of the camera matrices, as in the work of Beder et al. [5] and Koch et al. [70]. The relative position and orientation of all cameras can be estimated by this method. Secondly, it is possible to minimize an intensity cost between the images and the luminance signal of the TOF camera. This method estimates the photometric, as well as geometric, relationships between the different cameras [59, 101, 116]. A complete calibration method, which incorporates all of these considerations, is described by Lindner et al. [78].

The approaches described above, while capable of producing good results, have some limitations. Firstly, there may be residual distortions in the range data, that make a rigid alignment impossible [69]. Secondly, these approaches require the binocular system to be fully calibrated, and re-calibrated after any movement of the cameras. This requires, for best results, many views of a known calibration object. Typical view-synthesis applications, in contrast, require only a weak calibration of the cameras. One way to remove the calibration requirement is to perform an essentially 2-D registration of the different images [3, 7]. This, however, can only provide an instantaneous solution, because changes in the scene-structure produce corresponding changes in the image-to-image mapping.

An alternative approach is proposed here. It is hypothesized that the TOF reconstruction is approximately Euclidean. This means that an *uncalibrated* binocular reconstruction can be mapped directly into the Euclidean frame, by a suitable 3-D projective transformation. This is a great advantage for many applications, because automatic uncalibrated reconstruction is relatively easy. Furthermore, although the projective model is much more general than the rigid model, it preserves many important relationships between the images and the scene (e.g. epipolar geometry and incidence of points on planes). Finally, if required, the projective alignment can be upgraded to a fully calibrated solution, as in the methods described above.
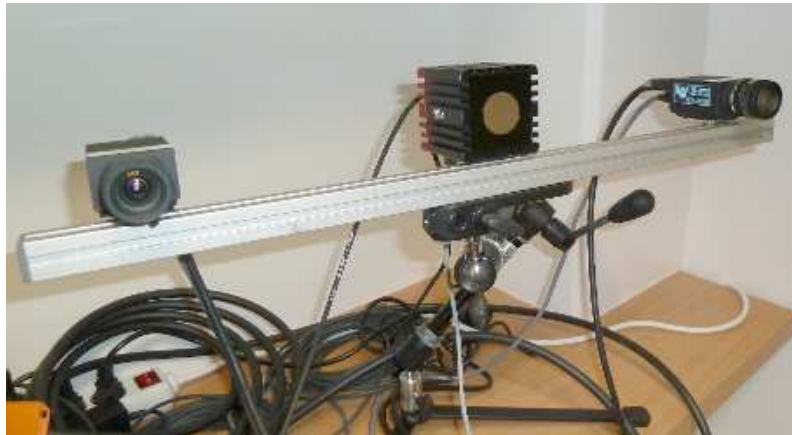
Fig. 4.2 A single TOF+2RGB system, as used in this chapter, with the TOF camera in the centre of the rail.

It is emphasized that the goal of this work is *not* to achieve the best possible photogrammetric reconstruction of the scene. Rather, the goal is to develop a practical way to associate colour and texture information to each range point, as in fig. 4.1. This output is intended for use in view-synthesis applications.

This chapter is organized as follows. Section 4.2.1 briefly reviews some standard material on projective reconstruction, while section 4.2.2 describes the representation of range data in the present work. The chief contributions of the subsequent

sections are as follows: Section **4.2.3** describes a *point-based* method that maps an ordinary *projective* reconstruction of the scene onto the corresponding range representation. This does not require the colour cameras to be calibrated (although it may be necessary to correct for lens distortion). Any planar object can be used to find the alignment, provided that image-features can be matched across all views (including that of the ToF camera). Section **4.2.4** describes a dual *plane-based* method, which performs the same projective alignment, but that does not require any point-matches between the views. Any planar object can be used, provided that it has a simple polygonal boundary that can be segmented in the colour and range data. This is a great advantage, owing to the very low resolution of the luminance data provided by the ToF camera (176×144 here). This makes it difficult to automatically extract and match point-descriptors from these images, as described in chapter 3. Furthermore, there are ToF devices that do not provide a luminance signal at all. Section **4.2.5** addresses the problem of multi-system alignment. Finally, section 4.3 describes the accuracy than can be achieved with a three ToF+2RGB system, including a new error-metric for ToF data in section **4.3.2**. Conclusions and future directions are discussed in section 4.4.

4.2 Methods

This section describes the theory of projective alignment, using the following notation. Bold type will be used for vectors and matrices. In particular, points $\boldsymbol{P}$, $\boldsymbol{Q}$ and planes $\boldsymbol{U}, \boldsymbol{V}$ in the 3-D scene will be represented by column-vectors of homogeneous coordinates, e.g.

$$\boldsymbol{P} = \begin{pmatrix} \boldsymbol{P}_\triangle \\ P_4 \end{pmatrix} \quad \text{and} \quad \boldsymbol{U} = \begin{pmatrix} \boldsymbol{U}_\triangle \\ U_4 \end{pmatrix} \tag{4.1}$$

where $\boldsymbol{P}_\triangle = (P_1, P_2, P_3)^\top$ and $\boldsymbol{U}_\triangle = (U_1, U_2, U_3)^\top$. The homogeneous coordinates are defined up to a nonzero scaling; for example, $\boldsymbol{P} \simeq (\boldsymbol{P}_\triangle / P_4, 1)^\top$. In particular, if $P_4 = 1$, then $\boldsymbol{P}_\triangle$ contains the ordinary space coordinates of the point $\boldsymbol{P}$. Furthermore, if $|\boldsymbol{U}_\triangle| = 1$, then U_4 is the signed perpendicular distance of the plane $\boldsymbol{U}$ from the origin, and $\boldsymbol{U}_\triangle$ is the unit normal. The point $\boldsymbol{P}$ is on the plane $\boldsymbol{U}$ if $\boldsymbol{U}^\top \boldsymbol{P} = 0$. The cross product $\boldsymbol{u} \times \boldsymbol{v}$ is often expressed as $(\boldsymbol{u})_\times \boldsymbol{v}$, where $(\boldsymbol{u})_\times$ is a 3×3 antisymmetric matrix. The column-vector of N zeros is written $\boldsymbol{0}_N$.

Projective cameras are represented by 3×4 matrices. For example, the range projection is

$$\boldsymbol{q} \simeq \boldsymbol{C}\boldsymbol{Q} \quad \text{where} \quad \boldsymbol{C} = (\boldsymbol{A}_{3\times3} \,|\, \boldsymbol{b}_{3\times1}). \tag{4.2}$$

The left and right colour cameras $\boldsymbol{C}_\ell$ and $\boldsymbol{C}_r$ are similarly defined, e.g. $\boldsymbol{p}_\ell \simeq \boldsymbol{C}_\ell \boldsymbol{P}$. Table 4.1 summarizes the geometric objects that will be aligned.

Points and planes in the two systems are related by the unknown 4×4 space-homography $\boldsymbol{H}$, so that

$$\boldsymbol{Q} \simeq \boldsymbol{H}\boldsymbol{P} \quad \text{and} \quad \boldsymbol{V} \simeq \boldsymbol{H}^{-\top} \boldsymbol{U}. \tag{4.3}$$

	Observed Points	Reconstructed Points	Planes
Binocular $\boldsymbol{C}_\ell,\boldsymbol{C}_r$	$\boldsymbol{p}_\ell, \boldsymbol{p}_r$	$\boldsymbol{P}$	$\boldsymbol{U}$
Range $\boldsymbol{C}$	$(\boldsymbol{q},\rho)$	$\boldsymbol{Q}$	$\boldsymbol{V}$

Table 4.1 Summary of notations in the left, right and range systems.

This model encompasses all rigid, similarity and affine transformations in 3-D. It preserves *collinearity* and *flatness*, and is linear in homogeneous coordinates. Note that, in the reprojection process, $\boldsymbol{H}$ can be interpreted as a modification of the camera matrices, e.g. $\boldsymbol{p}_\ell \simeq (\boldsymbol{C}_\ell \boldsymbol{H}^{-1})\boldsymbol{Q}$, where $\boldsymbol{H}^{-1}\boldsymbol{Q} \simeq \boldsymbol{P}$.

4.2.1 Projective Reconstruction

A projective reconstruction of the scene can be obtained from matched points $\boldsymbol{p}_{\ell k}$ and $\boldsymbol{p}_{rk}$, together with the fundamental matrix $\boldsymbol{F}$, where $\boldsymbol{p}_{rk}^\top \boldsymbol{F} \boldsymbol{p}_{\ell k} = 0$. The fundamental matrix can be estimated automatically, using the well-established RANSAC method. The camera matrices can then be determined, up to a four-parameter projective ambiguity [55]. In particular, from $\boldsymbol{F}$ and the epipole $\boldsymbol{e}_r$, the cameras can be defined as

$$\boldsymbol{C}_\ell \simeq (\boldsymbol{I}\,|\,\boldsymbol{0}_3) \quad \text{and} \quad \boldsymbol{C}_r \simeq \left((\boldsymbol{e}_r)_\times \boldsymbol{F} + \boldsymbol{e}_r \boldsymbol{g}^\top \,\middle|\, \gamma \boldsymbol{e}_r\right). \tag{4.4}$$

where $\gamma \neq 0$ and $\boldsymbol{g} = (g_1, g_2, g_3)^\top$ can be used to bring the cameras into a plausible form. This makes it easier to visualize the projective reconstruction and, more importantly, can improve the numerical conditioning of subsequent procedures.

4.2.2 Range Fitting

The TOF camera $\boldsymbol{C}$ provides the distance ρ of each scene-point from the camera-centre, as well as its image-coordinates $\boldsymbol{q} = (x, y, 1)$. The back-projection of this point into the scene is

$$\boldsymbol{Q}_\triangle = \boldsymbol{A}^{-1}\left((\rho/\alpha)\boldsymbol{q} - \boldsymbol{b}\right) \quad \text{where} \quad \alpha = \left|\boldsymbol{A}^{-1}\boldsymbol{q}\right|. \tag{4.5}$$

Hence the point $(\boldsymbol{Q}_\triangle, 1)^\top$ is at distance ρ from the optical centre $-\boldsymbol{A}^{-1}\boldsymbol{b}$, in the direction $\boldsymbol{A}^{-1}\boldsymbol{q}$. The scalar α serves to normalize the direction-vector. This is the standard pinhole model, as used in [4].

The range data are noisy and incomplete, owing to illumination and scattering effects. This means that, given a sparse set of features in the intensity image (of the TOF device), it is not advisable to use the back-projected point (4.5) directly. A better approach is to segment the image of the plane in each TOF camera (using the

the range and/or intensity data). It is then possible to back-project *all* of the enclosed points, and to robustly fit a plane V_j to the enclosed points Q_{ij}, so that $V_j^\top Q_{ij} \approx 0$ if point i lies on plane j. Now, the back-projection Q_π of each sparse feature point q can be obtained by intersecting the corresponding ray with the plane V, so that the new range estimate ρ^π is

$$\rho^\pi = \frac{V_\triangle^\top A^{-1} b - V_4}{(1/\alpha)\, V_\triangle^\top A^{-1} q} \tag{4.6}$$

where $|V_4|$ is the distance of the plane to the camera centre, and $V_\triangle$ is the unit-normal of the range plane. The new point Q^π is obtained by substituting ρ^π into (4.5).

The choice of plane-fitting method is affected by two issues. Firstly, there may be very severe outliers in the data, due to the photometric and geometric errors described in chapter 1. Secondly, the noise-model should be based on the pinhole model, which means that perturbations occur radially along visual directions, which are not (in general) perpendicular to the observed plane [56, 112]. Several plane-fitting methods, both iterative [66] and non-iterative [91] have been proposed for the pinhole model. The outlier problem, however, is often more significant. Hence, in practice, a RANSAC-based method is often the most effective.

4.2.3 Point-Based Alignment

It is straightforward to show that the transformation H in (4.3) could be estimated from five binocular points P_k, together with the corresponding range points Q_k. This would provide 5×3 equations, which determine the 4×4 entries of H, subject to an overall projective scaling. It is better, however, to use the 'Direct Linear Transformation' method [55], which fits H to *all* of the data. This method is based on the fact that if

$$P' = HP \tag{4.7}$$

is a perfect match for Q, then $\mu Q = \lambda P'$, and the scalars λ and μ can be eliminated between pairs of the four implied equations [20]. This results in $\binom{4}{2} = 6$ interdependent constraints per point. It is convenient to write these homogeneous equations as

$$\begin{pmatrix} Q_4 P'_\triangle - P'_4 Q_\triangle \\ Q_\triangle \times P'_\triangle \end{pmatrix} = \mathbf{0}_6. \tag{4.8}$$

Note that if P' and Q are normalized so that $P'_4 = 1$ and $Q_4 = 1$, then the magnitude of the top half of (4.8) is simply the distance between the points. Following Förstner [38], the left-hand side of (4.8) can be expressed as $(Q)_\wedge P'$ where

$$(Q)_\wedge = \begin{pmatrix} Q_4 I_3 & -Q_\triangle \\ (Q_\triangle)_\times & \mathbf{0}_3 \end{pmatrix} \tag{4.9}$$

is a 6×4 matrix, and $\left(\boldsymbol{Q}_\triangle\right)_\times \boldsymbol{P}_\triangle = \boldsymbol{Q}_\triangle \times \boldsymbol{P}_\triangle$, as usual. The equations (4.8) can now be written in terms of (4.7) and (4.9) as

$$\left(\boldsymbol{Q}\right)_\wedge \boldsymbol{H} \boldsymbol{P} = \boldsymbol{0}_6. \tag{4.10}$$

This system of equations is linear in the unknown entries of $\boldsymbol{H}$, the columns of which can be stacked into the 16×1 vector $\boldsymbol{h}$. The Kronecker product identity $\operatorname{vec}(\boldsymbol{XYZ}) = (\boldsymbol{Z}^\top \otimes \boldsymbol{X}) \operatorname{vec}(\boldsymbol{Y})$ can now be applied, to give

$$\left(\boldsymbol{P}^\top \otimes \left(\boldsymbol{Q}\right)_\wedge\right) \boldsymbol{h} = \boldsymbol{0}_6 \quad \text{where} \quad \boldsymbol{h} = \operatorname{vec}\left(\boldsymbol{H}\right). \tag{4.11}$$

If M points are observed on each of N planes, then there are $k = 1, \ldots, MN$ observed pairs of points, $\boldsymbol{P}_k$ from the projective reconstruction and $\boldsymbol{Q}_k$ from the range back-projection. The MN corresponding 6×16 matrices $\left(\boldsymbol{P}_k^\top \otimes (\boldsymbol{Q}_k)_\wedge\right)$ are stacked together, to give the complete system

$$\begin{pmatrix} \boldsymbol{P}_1^\top & \otimes & \left(\boldsymbol{Q}_1\right)_\wedge \\ & \vdots & \\ \boldsymbol{P}_{MN}^\top & \otimes & \left(\boldsymbol{Q}_{MN}\right)_\wedge \end{pmatrix} \boldsymbol{h} = \boldsymbol{0}_{6MN} \tag{4.12}$$

subject to the constraint $|\boldsymbol{h}| = 1$, which excludes the trivial solution $\boldsymbol{h} = \boldsymbol{0}_{16}$. It is straightforward to obtain an estimate of $\boldsymbol{h}$ from the SVD of the the $6MN \times 16$ matrix on the left of (4.12). This solution, which minimizes an *algebraic error* [55], is the singular vector corresponding to the smallest singular value of the matrix. In the minimal case, $M = 1, N = 5$, the matrix would be 30×16. Note that the point coordinates should be transformed, to ensure that (4.12) is numerically well-conditioned [55]. In this case the transformation ensures that $\sum_k \boldsymbol{P}_{k\triangle} = \boldsymbol{0}_3$ and $\frac{1}{MN} \sum_k |\boldsymbol{P}_{k\triangle}| = \sqrt{3}$, where $P_{k4} = 1$. The analogous transformation is applied to the range points $\boldsymbol{Q}_k$.

The DLT method, in practice, gives a good approximation $\boldsymbol{H}_{\text{DLT}}$ of the homography (4.3). This can be used as a starting-point for the iterative minimization of a more appropriate error measure. In particular, consider the *reprojection error* in the left image,

$$E_\ell(\boldsymbol{C}_\ell) = \sum_{k=1}^{MN} D\left(\boldsymbol{C}_\ell \boldsymbol{Q}_k, \boldsymbol{p}_{\ell k}\right)^2 \tag{4.13}$$

where $D(\boldsymbol{p}, \boldsymbol{q}) = |\boldsymbol{p}_\triangle / p_3 - \boldsymbol{q}_\triangle / q_3|$. A 12-parameter optimization of (4.13), starting with $\boldsymbol{C}_\ell \leftarrow \boldsymbol{C}_\ell \boldsymbol{H}_{\text{DLT}}^{-1}$, can be performed by the Levenberg-Marquardt algorithm [94]. The result will be the camera matrix $\boldsymbol{C}_\ell^\star$ that best reprojects the range data into the left image ($\boldsymbol{C}_r^\star$ is similarly obtained). The solution, provided that the calibration points adequately covered the scene volume, will remain valid for subsequent depth and range data.

Alternatively, it is possible to minimize the *joint* reprojection error, defined as the sum of left and right contributions,

$$E\left(\boldsymbol{H}^{-1}\right) = E_\ell\left(\boldsymbol{C}_\ell \boldsymbol{H}^{-1}\right) + E_r\left(\boldsymbol{C}_r \boldsymbol{H}^{-1}\right) \tag{4.14}$$

over the (inverse) homography H^{-1}. The 16 parameters are again minimized by the Levenberg-Marquardt algorithm, starting from the DLT solution H_{DLT}^{-1}.

The difference between the separate (4.13) and joint (4.14) minimizations is that the latter preserves the original epipolar geometry, whereas the former does not. Recall that C_ℓ C_r, H and F are all defined up to scale, and that F satisfies an additional rank-two constraint [55]. Hence the underlying parameters can be counted as $(12-1)+(12-1)=22$ in the separate minimizations, and as $(16-1)=15$ in the joint minimization. The fixed epipolar geometry accounts for the $(9-2)$ missing parameters in the joint minimization. If F is known to be very accurate (or must be preserved) then the joint minimization (4.14) should be performed. This will also preserve the original binocular triangulation, provided that a projective-invariant method was used [54]. However, if minimal reprojection error is the objective, then the cameras should be treated separately. This will lead to a new fundamental matrix $F^\star = (e_r^\star)_\times C_r^\star (C_\ell^\star)^+$, where $(C_\ell^\star)^+$ is the generalized inverse. The right epipole is obtained from $e_r^\star = C_r^\star d_\ell^\star$, where $d_\ell^\star$ represents the nullspace $C_\ell^\star d_\ell^\star = 0_3$.

4.2.4 Plane-Based Alignment

The DLT algorithm of section 4.2.3 can also be used to recover H from matched *planes*, rather than matched points. Equation (4.10) becomes

$$\left(V\right)_\wedge H^{-\top} U = 0_6 \tag{4.15}$$

where U and V represent the estimated coordinates of the same plane in the parallax and range reconstructions, respectively. The estimation procedure is identical to that in section 4.2.3, but with $\mathrm{vec}(H^{-\top})$ as the vector of unknowns.

This method, in practice, produces very poor results. The chief reason that obliquely-viewed planes are foreshortened, and therefore hard to detect/estimate, in the low-resolution ToF images. It follows that the calibration data-set is biased towards fronto-parallel planes.[1] This bias allows the registration to slip sideways, perpendicular to the primary direction of the ToF camera. The situation is greatly improved by assuming that the *boundaries* of the planes can be detected. For example, if the calibration object is rectangular, then the range-projection of the plane V is bounded by four edges $\bar{v}_i$, where $i = 1,\ldots 4$. Note that these are detected as *depth* edges, and so no luminance data are required. The edges, represented as lines $\bar{v}_i$, back-project as the faces of a pyramid,

$$\bar{V}_i = C^\top \bar{v}_i = \begin{pmatrix} \bar{V}_{i\triangle} \\ 0 \end{pmatrix}, \quad i = 1,\ldots L \tag{4.16}$$

---

[1] The point-based algorithm is unaffected by this bias, because the scene is ultimately 'filled' with points, regardless of the contributing planes.

where $L = 4$ in the case of a quadrilateral projection. These planes are linearly dependent, because they pass through the centre of projection; hence the fourth coordinates are all zero if, as here, the ToF camera is at the origin. Next, if the corresponding edges $\bar{u}_{\ell i}$ and $\bar{u}_{ri}$ can be detected in the binocular system, using both colour and parallax information, then the planes $\bar{U}_i$ can easily be constructed. Each calibration plane now contributes an additional $6L$ equations

$$\left(\bar{V}_i\right)_\wedge H^{-\top} \bar{U}_i = \mathbf{0}_6 \tag{4.17}$$

to the DLT system (4.12). Although these equations are quite redundant (any two planes span all possibilities), they lead to a much better DLT estimate. This is because they represent exactly those planes that are most likely to be missed in the calibration data, owing to the difficulty of feature-detection over surfaces that are extremely foreshortened in the image.

As in the point-based method, the plane coordinates should be suitably transformed, in order to make the numerical system (4.12) well-conditioned. The transformed coordinates satisfy the location constraint $\sum_k U_{k\triangle} = \mathbf{0}_3$, as well as the scale constraint $\sum_k |U_{k\triangle}|^2 = 3\sum_k U_{k4}^2$, where $U_{k\triangle} = (U_{k1}, U_{k2}, U_{k3})^\top$, as usual. A final renormalization $|U_k| = 1$ is also performed. This procedure, which is also applied to the V_k, is analogous to the treatment of line-coordinates in DLT methods [120].

The remaining problem is that the original reprojection error (4.13) cannot be used to optimize the solution, because no luminance features q have been detected in the range images (and so no 3-D points Q have been distinguished). This can be solved by reprojecting the physical edges of the calibration planes, after reconstructing them as follows. Each edge-plane $\bar{V}_i$ intersects the range plane V in a space-line, represented by the 4×4 Plücker matrix

$$W_i = V\bar{V}_i^\top - \bar{V}_i V^\top. \tag{4.18}$$

The line W_i reprojects to a 3×3 antisymmetric matrix [55]; for example

$$W_{\ell i} \simeq C_\ell W_i C_\ell^\top \tag{4.19}$$

in the left image, and similarly in the right. Note that $W_{\ell i} p_\ell = \mathbf{0}$ if the point p_ℓ is on the reprojected line [55]. The line-reprojection error can therefore be written as

$$E_\ell^\times(C_\ell) = \sum_{i=1}^{L} \sum_{j=1}^{N} D_\times \left(C_\ell W_i C_\ell^\top, \bar{u}_{\ell i j}\right)^2. \tag{4.20}$$

The function $D_\times(M, n)$ compares image-lines, by computing the sine of the angle between the two coordinate-vectors,

$$D_\times(M, n) = \frac{\sqrt{2}\,|Mn|}{|M|\,|n|} = \frac{|m \times n|}{|m|\,|n|}, \tag{4.21}$$

where $M = (m)_\times$, and $|M|$ is the Frobenius norm. It is emphasized that the coordinates *must* be normalized by a suitable transformations G_ℓ and G_r, as in the case of the DLT. For example, the line n should be fitted to points of the form Gp, and then M should be transformed as $G^{-\top}M$, before computing (4.21). The reprojection error (4.20) is numerically unreliable without this normalization.

The line-reprojection (4.21) can either be minimized separately for each camera, or jointly as

$$E^\times\left(H^{-1}\right) = E_\ell^\times\left(C_\ell H^{-1}\right) + E_r^\times\left(C_r H^{-1}\right) \tag{4.22}$$

by analogy with (4.14). Finally, it should be noted that although (4.21) is defined in the *image*, it is an *algebraic* error. However, because the errors in question are small, this measure behaves predictably.

4.2.5 Multi-System Alignment

The point-based and plane-based procedures, described in section 4.2.3 and 4.2.4 respectively, can be used to calibrate a single ToF+2RGB system. Related methods can be used for the joint calibration of several such systems, as will now be explained, using the *point-based* representation. In this section the notation P_i will be used for the binocular coordinates (with respect to the left camera) of a point in the i-th system, and likewise Q_i for the ToF coordinates of a point in the same system. Hence the i-th ToF, left and right RGB cameras have the form

$$C_i \simeq \left(A_i \,|\, 0_3\right), \quad C_{\ell i} \simeq \left(A_{\ell i} \,|\, 0_3\right) \quad \text{and} \quad C_{ri} \simeq \left(A_{ri} \,|\, b_{ri}\right) \tag{4.23}$$

where A_i and $A_{\ell i}$ contain only *intrinsic* parameters, whereas A_{ri} also encodes the relative orientation of C_{ri} with respect to $C_{\ell i}$. Each system has a transformation H_i^{-1} that maps ToF points Q_i into the corresponding RGB coordinate system of $C_{\ell i}$. Furthermore, let the 4×4 matrix G_{ij} be the transformation from system j, mapping *back* to system i. This matrix, in the calibrated case, would be a rigid 3-D transformation. However, by analogy with the ToF-to-RGB matrices, each G_{ij} is generalized here to a projective transformation, thereby allowing for spatial distortions in the data. The left and right cameras that project a scene-point P_j in coordinate system j to image-points $p_{\ell i}$ and p_{ri} in system i are

$$C_{\ell ij} = C_{\ell i}\, G_{ij} \quad \text{and} \quad C_{rij} = C_{ri}\, G_{ij}. \tag{4.24}$$

Note that if a single global coordinate system is chosen to coincide with the k-th RGB system, then a point P_k projects via $C_{\ell ik}$ and C_{rik}. These two cameras are respectively equal to $C_{\ell i}$ and C_{ri} in (4.23) only when $i = k$, such that $G_{ij} = I$ in (4.24). A typical three-system configuration is shown in fig. 4.3.

The transformation G_{ij} can only be estimated directly if there is a region of common visibility between systems i and j. If this is not the case (as when the systems face each other, such that the front of the calibration board is not simultaneously
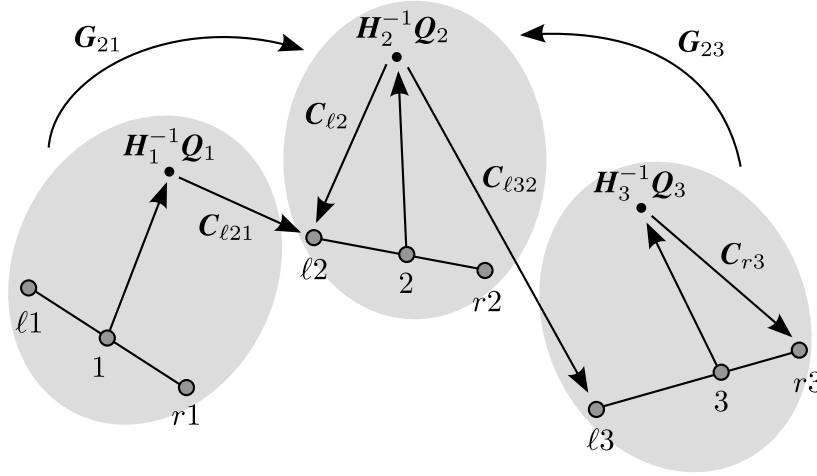
Fig. 4.3 Example of a three TOF+2RGB setup, with TOF cameras labelled 1,2,3. Each ellipse represents a separate system, with system 2 chosen as the reference. The arrows (with camera-labels) show some possible TOF-to-RGB projections. For example, a point $P_2 \simeq H_2^{-1}Q_2$ in the centre projects directly to RGB view $\ell 2$ via $C_{\ell 2}$, whereas the same point projects to $\ell 3$ via $C_{\ell 32} = C_{\ell 3}G_{32}$.

visible), then G_{ij} can be computed indirectly. For example, $G_{02} = G_{01}G_{12}$ where $P_2 = G_{12}^{-1}G_{01}^{-1}P_0$. Note that the stereo-reconstructed points P are used to estimate these transformations, as they are more reliable than the TOF points Q.

4.3 Evaluation

The following sections will describe the accuracy of a nine-camera setup, calibrated by the methods described above. Section 4.3.1 will evaluate *calibration* error, whereas section 4.3.2 will evaluate *total* error. The former is essentially a fixed function of the estimated camera matrices, for a given scene. The latter also includes the range-noise from the TOF cameras, which varies from moment to moment. The importance of this distinction will be discussed.

The setup consists of three rail-mounted TOF+2RGB systems, $i = 1\ldots 3$, as in fig. 4.3. The stereo baselines are 17cm on average, and the TOF cameras are separated by 107cm on average. The RGB images are 1624×1224, whereas the Mesa Imaging SR4000 TOF images are 176×144, with a depth range of 500cm. The three stereo systems are first calibrated by standard methods, returning a full Euclidean decomposition of $C_{\ell i}$ and C_{ri}, as well as the associated lens parameters. It was established in [52] that projective alignment is generally superior to similarity alignment, and so the transformations G_{ij} and H_j^{-1} will be 4×4 homographies. These transformations were estimated by the DLT method, and refined by LM-minimization of the joint geometric error, as in (4.14).

4.3.1 Calibration Error

The calibration error is measured by first taking TOF points Q_j^π corresponding to *vertices* on the reconstructed calibration plane π_j in system j, as described in section 4.2.2. These can then be projected into a pair of RGB images in system i, so that the error $E_{ij}^{cal} = \frac{1}{2}\left(E_{\ell ij}^{cal} + E_{rij}^{cal}\right)$ can be computed, where

$$E_{\ell ij}^{cal} = \frac{1}{|\pi|}\sum_{Q_j^\pi} D\left(C_{\ell ij}H_j^{-1}Q_j^\pi,\, p_{\ell i}\right) \tag{4.25}$$

and E_{rij}^{cal} is similarly defined. The function $D(\cdot,\cdot)$ computes the image-distance between inhomogenized points, as in (4.13), and the denominator corresponds to the number of vertices on the board, with $|\pi| = 35$ in the present experiments. The measure (4.25) can of course be averaged over all images in which the board is visible. The calibration procedure has an accuracy of around one pixel, as shown in fig. 4.4.
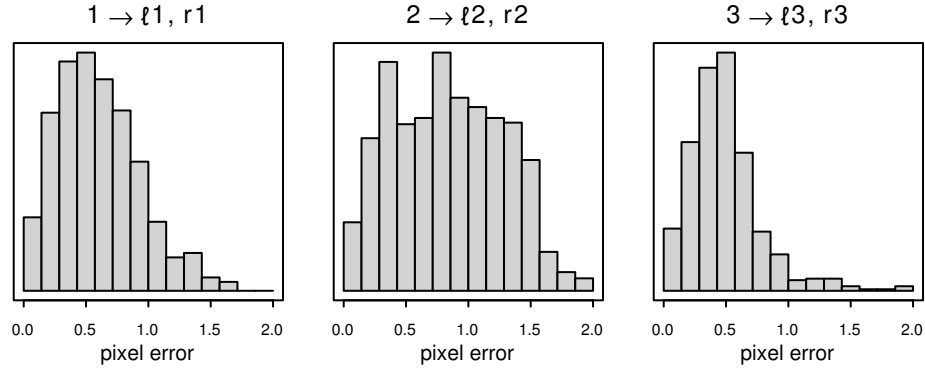

Fig. 4.4 Calibration error (4.25), measured by projecting the fitted TOF points Q^π to the left and right RGB images (1624×1224) in three separate systems. Each histogram combines left-camera and right-camera measurements from 15 views of the calibration board. Subpixel accuracy is obtained.

4.3.2 Total Error

The calibration error, as reported in the preceding section, is the natural way to evaluate the estimated cameras and homographies. It is not, however, truly representative of the 'live' performance of the complete setup. This is because the calibration error uses each estimated plane π_j to replace all vertices Q_j with the *fitted* versions

Q_j^π. In general, however, no surface model is available, and so the raw points Q_j must be used as input for meshing and rendering processes.

The total error, which combines the calibration and range errors, can be measured as follows. The i-th RGB views of plane π_j must be related to the TOF image-points q_j by the 2-D *transfer* homographies $T_{\ell i j}$ and $T_{r i j}$, where

$$p_{\ell i} \simeq T_{\ell i j} q_j \quad \text{and} \quad p_{r i} \simeq T_{r i j} q_j. \tag{4.26}$$

These 3×3 matrices can be estimated accurately, because the range-data itself is not required. Furthermore, let Π_j be the hull (i.e. bounding-polygon) of plane π_j as it appears in the TOF image. Any pixel q_j in the hull (including the original calibration vertices) can now be *re-projected* to the i-th RGB views via the 3-D point Q_j, or *transferred* directly by $T_{\ell i j}$ and $T_{r i j}$ in (4.26). The total error is the average difference between the reprojections and the transfers, $E_{ij}^{\text{tot}} = \frac{1}{2}\left(E_{\ell i j}^{\text{tot}} + E_{r i j}^{\text{tot}}\right)$, where

$$E_{\ell i j}^{\text{tot}} = \frac{1}{|\Pi_j|} \sum_{q_j \in \Pi_j} D\left(C_{\ell i j} H_j^{-1} Q_j, \; T_{\ell i j} q_j\right) \tag{4.27}$$

and $E_{r i j}^{\text{tot}}$ is similarly defined. The view-dependent denominator $|\Pi_j| \gg |\pi|$ is the number of pixels in the hull Π_j. Hence E_{ij}^{tot} is the total error, including range-noise, of TOF plane π_j as it appears in the i-th RGB cameras.

If the RGB cameras are not too far from the TOF camera, then the range errors tend to be cancelled in the reprojection. This is evident in fig. 4.5, although it is clear that the tail of each distribution is increased by the range error. However, if the RGB cameras belong to another system, with a substantially different location, then the range errors can be very large in the reprojection. This is clear from fig. 4.6, which shows that a substantial proportion of the TOF points reproject to the other systems with a total error in excess of ten pixels.
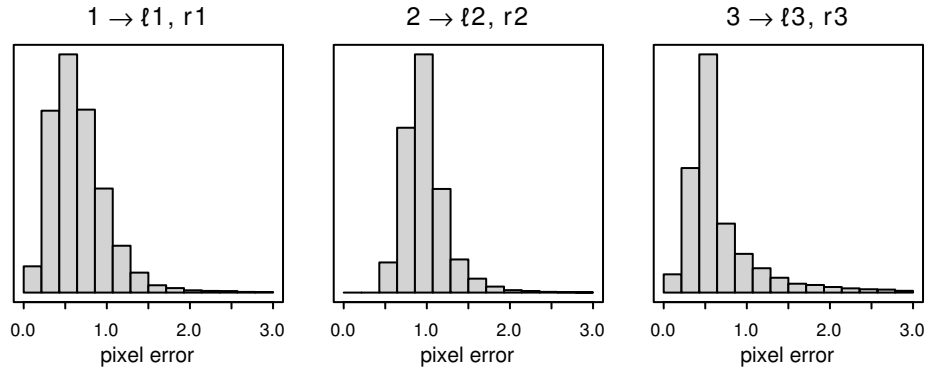

Fig. 4.5 Total error (4.27), measured by projecting the raw TOF points Q to the left and right RGB images (1624×1224) in three separate systems. These distributions have longer and heavier tails than those of the corresponding calibration errors, shown in fig. 4.4.

$2 \rightarrow \ell 1, r1$ $2 \rightarrow \ell 3, r3$

pixel error   pixel error
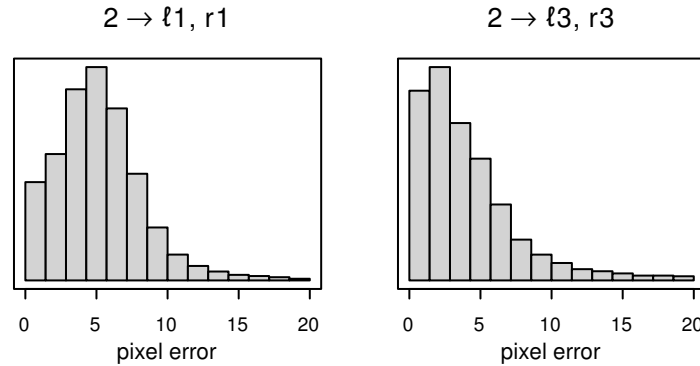
Fig. 4.6 Total error when reprojecting raw TOF points from system 2 to RGB cameras in systems 1 and 3 (left and right, respectively). The range errors are emphasized by the difference in viewpoints between the two systems. Average error is now around five pixels in the 1624×1224 images, and the noisiest TOF points reproject with tens of pixels of error.

It is possible to understand these results more fully by examining the distribution of the total error across individual boards. Figure 4.7 shows the distribution for a board reprojected to the same system (i.e. part of the data from fig. 4.5). There is a relatively smooth gradient of error across the board, which is attributable to errors in the fitting of plane π_j, and in the estimation of the camera parameters. The pixels can be divided into sets from the black and white squares, using the known board geometry and detected vertices. It can be seen in fig. 4.7 (right) that the total error for each set is comparable. However, when reprojecting to a different system, fig. 4.8 shows that the total error is correlated with the black and white squares on the board. This is due to significant absorption of the infrared signal by the black squares.
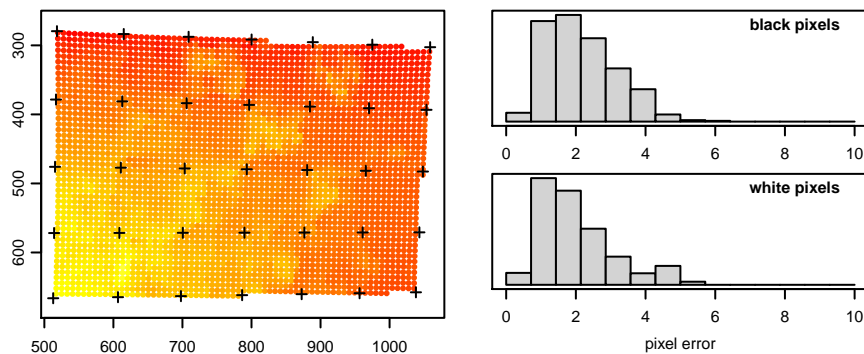

Fig. 4.7 Left: 3-D TOF pixels ($|\Pi| = 3216$), on a calibration board, reprojected to an RGB image in the *same* TOF+2RGB system. Each pixel is colour-coded by the total error (4.27). Black crosses are the detected vertices in the RGB image. Right: histograms of total error, split into pixels on black or white squares.
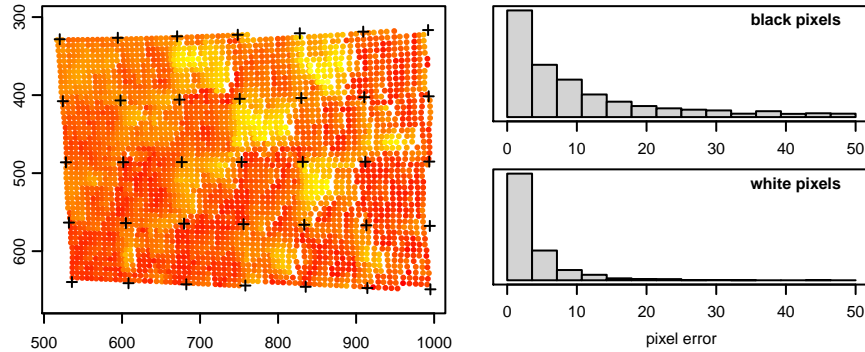
Fig. 4.8 Left: 3-D ToF pixels, as in fig. 4.7, reprojected to an RGB image in a *different* ToF+2RGB system. Right: histograms of total error, split into pixels on black or white squares. The depth of the black squares is much less reliable, which leads to inaccurate reprojection into the target system.

4.4 Conclusions

It has been shown that there is a projective relationship between the data provided by a ToF camera, and an uncalibrated binocular reconstruction. Two practical methods for computing the projective transformation have been introduced; one that requires luminance point-correspondences between the ToF and colour cameras, and one that does not. Either of these methods can be used to associate binocular colour and texture with each 3-D point in the range reconstruction. It has been shown that the point-based method can easily be extended to multiple-ToF systems, with calibrated or uncalibrated RGB cameras.

The problem of ToF-noise, especially when reprojecting 3-D points to a very different viewpoint, has been emphasized. This source of error can be reduced by application of the de-noising methods described in chapter 1. Alternatively, having aligned the ToF and RGB systems, it is possible to refine the 3-D representation by image-matching, as explained in chapter 5.

Chapter 5
A Mixed Time-of-Flight and Stereoscopic Camera System

Abstract Several methods that combine range and color data have been investigated and successfully used in various applications. Most of these systems suffer from the problems of noise in the range data and resolution mismatch between the range sensor and the color cameras. High-resolution depth maps can be obtained using stereo matching, but this often fails to construct accurate depth maps of weakly/repetitively textured scenes. Range sensors provide coarse depth information regardless of presence/absence of texture. We propose a novel ToF-stereo fusion method based on an efficient seed-growing algorithm which uses the ToF data projected onto the stereo image pair as an initial set of correspondences. These initial "seeds" are then propagated to nearby pixels using a matching score that combines an image similarity criterion with rough depth priors computed from the low-resolution range data. The overall result is a dense and accurate depth map at the resolution of the color cameras at hand. We show that the proposed algorithm outperforms 2D image-based stereo algorithms and that the results are of higher resolution than off-the-shelf RGB-D sensors, e.g., Kinect.

5.1 Introduction

Advanced computer vision applications require both depth and color information. Hence, a system composed of ToF and color cameras should be able to provide accurate *color and depth* information for each pixel and at high resolution. Such a *mixed* system can be very useful for a large variety of vision problems, e.g., for building dense 3D maps of indoor environments.

The 3D structure of a scene can be reconstructed from two or more 2D views via a *parallax* between corresponding image points. However, it is difficult to obtain accurate pixel-to-pixel matches for scenes of objects without textured surfaces, with repetitive patterns, or in the presence of occlusions. The main drawback is that stereo matching algorithms frequently fail to reconstruct indoor scenes composed

of untextured surfaces, e.g., walls, repetitive patterns and surface discontinuities, which are typical in man-made environments.

Alternatively, *active-light* range sensors, such as time-of-flight (ToF) or structured-light cameras (see chapter 1), can be used to directly measure the 3D structure of a scene at video frame-rates. However, the spatial resolution of currently available range sensors is lower than high-definition (HD) color cameras, the luminance sensitivity is poorer and the depth range is limited. The range-sensor data are often noisy and incomplete over extremely scattering parts of the scene, e.g., non-Lambertian surfaces. Therefore it is not judicious to rely solely on range-sensor estimates for obtaining 3D maps of complete scenes. Nevertheless, range cameras provide good initial estimates independently of whether the scene is textured or not, which is not the case with stereo matching algorithms. These considerations show that it is useful to combine the active-range and the passive-parallax approaches, in a *mixed* system. Such a system can overcome the limitations of both the active- and passive-range (stereo) approaches, when considered separately, and provides accurate and fast 3D reconstruction of a scene at high resolution, e.g., 1200×1600 pixels, as in fig. 5.1.

5.1.1 Related Work

The combination of a depth sensor with a color camera has been exploited in several applications such as object recognition [48, 108, 2], person awareness, gesture recognition [31], simultaneous localization and mapping (SLAM) [10, 64], robotized plant-growth measurement [1], etc. These methods mainly deal with the problem of noise in depth measurement, as examined in chapter 1, as well as with the low resolution of range data as compared to the color data. Also, most of these methods are limited to RGB-D, i.e., a *single* color image combined with a range sensor. Interestingly enough, the recently commercialized Kinect [39] camera falls in the RGB-D family of sensors. We believe that extending the RGB-D sensor model to RGB-D-RGB sensors is extremely promising and advantageous because, unlike the former type of sensor, the latter type can combine active depth measurement with stereoscopic matching and hence better deal with the problems mentioned above.

Stereo matching has been one of the most studied paradigms in computer vision. There are several papers, e.g., [99, 103] that overview existing techniques and that highlight recent progress in stereo matching and stereo reconstruction. While a detailed description of existing techniques is beyond the scope of this section, we note that algorithms based on greedy local search techniques are typically fast but frequently fail to reconstruct the poorly textured regions or ambiguous surfaces. Alternatively, global methods formulate the matching task as an optimization problem which leads the minimization of a Markov random field (MRF) energy function of the image similarity likelihood and a prior on the surface smoothness. These algorithms solve some of the aforementioned problems of local methods but are very complex and computationally expensive since optimizing an MRF-based energy function is an NP-hard problem in the general case.

(a) A ToF-stereo setup

(b) A high-resolution color image pair with the low-resolution ToF image shown in the upper-left corner of the left image at the true scale.

(c) The proposed method delivers a high-resolution depth map.

Fig. 5.1 (a) Two high-resolution color cameras (2.0MP at 30FPS) are combined with a single low-resolution time-of-flight camera (0.03MP at 30FPS). (b) The 144×177 ToF image (upper left corner) and two 1224×1624 color images are shown at the true scale. (c) The depth map obtained with our method. The technology used by both these camera types allows simultaneous range and photometric data acquisition with an extremely accurate temporal synchronization, which may not be the case with other types of range cameras such as the current version of Kinect.

A practical tradeoff between the local and the global methods in stereo is the seed-growing class of algorithms [12, 13, 14]. The correspondences are grown from a small set of initial correspondence seeds. Interestingly, they are not particularly sensitive to bad input seeds. They are significantly faster than the global approaches, but they have difficulties in presence of non textured surfaces; Moreover, in these cases they yield depth maps which are relatively sparse. Denser maps can be obtained by relaxing the matching threshold but this leads to erroneous growth, so there is a natural tradeoff between the accuracy and density of the solution. Some form of regularization is necessary in order to take full advantage of these methods.

Recently, external prior-based generative probabilistic models for stereo matching were proposed [43, 87] for reducing the matching ambiguities. The priors used were based on surface-triangulation obtained from an initially-matched distinctive interest points in the two color images. Again, in the absence of textured regions, such support points are only sparsely available, and are not reliable enough or are not available at all in some image regions, hence the priors are erroneous. Consequently, such prior-based methods produce artifacts where the priors win over the data, and the solution is biased towards such incorrect priors. This clearly shows the need for more accurate prior models. Wang et al. [113] integrate a regularization term based on the depth values of initially matched *ground control points* in a global energy minimization framework. The ground control points are gathered using an accurate laser scanner. The use of a laser scanner is tedious because it is difficult to operate and because it cannot provide depth measurements fast enough such that it can be used in a practical computer vision application.

ToF cameras are based on an active sensor principle[1] that allows 3D data acquisition at video frame rates, e.g., 30FPS as well as accurate synchronization with any number of color cameras[2]. A modulated infrared light is emitted from the camera's internal lighting source, is reflected by objects in the scene and eventually travels back to the sensor, where the time of flight between sensor and object is measured independently at each of the sensor's pixel by calculating the precise phase delay between the emitted and the detected waves. A complete depth map of the scene can thus be obtained using this sensor at the cost of very low spatial resolution and coarse depth accuracy (see chapter 1 for details).

The fusion of ToF data with stereo data has been recently studied. For example, [22] obtained a higher quality depth map, by a probabilistic ad-hoc fusion of ToF and stereo data. Work in [125] merges the depth probability distribution function obtained from ToF and stereo. However both these methods are meant for improvement over the initial data gathered with the ToF camera and the final depth-map result is still limited to the resolution of the ToF sensor. The method proposed in this chapter increases the resolution from 0.03MP to the full resolution of the color cameras being used, e.g., 2MP.

The problem of depth map up-sampling has been also addressed in the recent past. In [15] a noise-aware filter for adaptive multi-lateral up-sampling of ToF depth

---

[1] All experiments described in this chapter use the Mesa SR4000 camera [80].

[2] http://www.4dviews.com

maps is presented. The work described in [48, 90] extends the model of [25], and [48] demonstrates that the object detection accuracy can be significantly improved by combining a state-of-art 2D object detector with 3D depth cues. The approach deals with the problem of resolution mismatch between range and color data using an MRF-based super-resolution technique in order to infer the depth at every pixel. The proposed method is slow: It takes around 10 seconds to produce a 320×240 depth image. All of these methods are limited to depth-map up-sampling using only a single color image and do not exploit the added advantage offered by stereo matching, which can highly enhance the depth map both qualitatively and quantitatively. Recently, [36] proposed a method which combines ToF estimates with stereo in a semi-global matching framework. However, at pixels where ToF disparity estimates are available, the image similarity term is ignored. This make the method quite susceptible to errors in regions where ToF estimates are not precise, especially in textured regions where stereo itself is reliable.

5.1.2 Chapter Contributions

In this chapter we propose a novel method for incorporating range data within a robust seed-growing algorithm for stereoscopic matching [12]. A calibrated system composed of an active range sensor and a stereoscopic color-camera pair, as described in chapter 4 and [52], allows the range data to be aligned and then projected onto each one of the two images, thus providing an initial sparse set of point-to-point correspondences (seeds) between the two images. This initial seed-set is used in conjunction with the seed-growing algorithm proposed in [12]. The projected ToF points are used as the vertices of a mesh-based surface representation which, in turn, is used as a prior to regularize the image-based matching procedure. The novel probabilistic *fusion* model proposed here (between the mesh-based surface initialized from the sparse ToF data and the seed-growing stereo matching algorithm itself) combines the merits of the two 3D sensing methods (active and passive) and overcomes some of the limitations outlined above. Notice that the proposed fusion model can be incorporated within virtually any stereo algorithm that is based on energy minimization and which requires some form initialization. It is, however, particularly efficient and accurate when used in combination with match-propagation methods.

The remainder of this chapter is structured as follows: Section 5.2 describes the proposed range-stereo fusion algorithm. The growing algorithm is summarized in section 5.2.1. The processing of the ToF correspondence seeds is explained in section 5.2.2, and the sensor fusion based similarity statistic is described in section 5.2.3. Experimental results on a real dataset and evaluation of the method, are presented in section 5.3. Finally, section 5.4 draws some conclusions.

5.2 The Proposed ToF-Stereo Algorithm

As outlined above, the ToF camera provides a low-resolution depth map of a scene. This map can be projected onto the left and right images associated with the stereoscopic pair, using the projection matrices estimated by the calibration method described in chapter 4. Projecting a single 3D point (x, y, z) gathered by the ToF camera onto the *rectified* images provides us with a pair of corresponding points (u, v) and (u', v') with $v' = v$ in the respective images. Each element (u, u', v) denotes a point in the disparity space[3]. Hence, projecting all the points obtained with the ToF camera gives us a sparse set of 2D point correspondences. This set is termed as the set of initial support points or ToF *seeds*.

These initial support points are used in a variant of the seed-growing stereo algorithm [12, 14] which further grows them into a denser and higher resolution disparity map. The seed-growing stereo algorithms propagate the correspondences by searching in the small neighborhoods of the seed correspondences. Notice that this growing process limits the disparity space to be visited to only a small fraction, which makes the algorithm extremely efficient from a computational point of view. The limited neighborhood also gives a kind of implicit regularization, nevertheless the solution can be arbitrarily complex, since multiple seeds are provided.

The integration of range data within the seed-growing algorithm requires two major modifications: (1) The algorithm is using ToF seeds instead of the seeds obtained by matching distinctive image features, such as interest points, between the two images, and (2) the growing procedure is regularized using a similarity statistic which takes into account the photometric consistency as well as the depth likelihood based on disparity estimate by interpolating the rough triangulated ToF surface. This can be viewed as a prior cast over the disparity space.

5.2.1 The Growing Procedure

The growing algorithm is sketched in pseudo-code as algorithm 1. The input is a pair of rectified images (I_L, I_R), a set of *refined* ToF seeds $\mathscr{S}$ (see below), and a parameter τ which directly controls a trade-off between matching accuracy and matching density. The output is a disparity map D which relates pixel correspondences between the input images.

First, the algorithm computes the prior disparity map D_p by interpolating ToF seeds. Map D_p is of the same size as the input images and the output disparity map, Step 1. Then, a similarity statistic $simil(s|I_L, I_R, D_p)$ of the correspondence, which measures both the photometric consistency of the potential correspondence as well as its consistency with the prior, is computed for all seeds $s = (u, u', v) \in \mathscr{S}$, Step 2. Recall that the seed s stands for a pixel-to-pixel correspondence $(u, v) \leftrightarrow (u', v)$ between the left and the right images. For each seed, the algorithm searches other cor-

---

[3] The disparity space is a space of all potential correspondences [99].

Algorithm 1 Growing algorithm for ToF-stereo fusion

Require: Rectified images (I_L, I_R),
  initial correspondence seeds $\mathscr{S}$,
  image similarity threshold τ.

1: Compute the prior disparity map D_p by interpolating seeds $\mathscr{S}$.
2: Compute $\text{simil}(s|I_L, I_R, D_p)$ for every seed $s \in \mathscr{S}$.
3: Initialize an empty disparity map D of size I_L (and D_p).
4: **repeat**
5:   Draw seed $s \in \mathscr{S}$ of the best $\text{simil}(s|I_L, I_R, D_p)$ value.
6:   **for** each of the four best neighbors $i \in \{1, 2, 3, 4\}$
$$q_i^* = (u, u', v) = \underset{q \in \mathscr{N}_i(s)}{\text{argmax simil}}(q|I_L, I_R, D_p)$$
   do
7:     $c := \text{simil}(q_i^*|I_L, I_R, D_p)$
8:     **if** $c \geq \tau$ **and** pixels not matched yet **then**
9:       Update the seed queue $\mathscr{S} := \mathscr{S} \cup \{q_i^*\}$.
10:      Update the output map $D(u, v) = u - u'$.
11:    **end if**
12:   **end for**
13: **until** $\mathscr{S}$ is empty
14: **return** disparity map D.

---

respondences in the surroundings of the seeds by maximizing the similarity statistic. This is done in a 4-neighborhood $\{\mathscr{N}_1, \mathscr{N}_2, \mathscr{N}_3, \mathscr{N}_4\}$ of the pixel correspondence, such that in each respective direction (left, right, up, down) the algorithm searches the disparity in a range of ± 1 pixel from the disparity of the seed, Step 6. If the similarity statistic of a candidate exceeds the threshold value τ, then a new correspondence is found, Step 8. This new correspondence becomes itself a new seed, and the output disparity map D is updated accordingly. The process repeats until there are no more seeds to be grown.

The algorithm is robust to a fair percentage of wrong initial seeds. Indeed, since the seeds compete to be matched based on a best-first strategy, the wrong seeds typically have low score $\text{simil}(s)$ associated with them and therefore when they are evaluated in Step 5, it is likely that the involved pixels been already matched. For more details on the growing algorithm, we refer the reader to [14, 12].

5.2.2 ToF Seeds and Their Refinement

The original version of the seed-growing stereo algorithm [14] uses an initial set of seeds $\mathscr{S}$ obtained by detecting interest points in both images and matching them. Here, we propose to use ToF seeds. As already outlined, these seeds are obtained by projecting the low-resolution depth map associated with the ToF camera onto the high-resolution images. Likewise the case of interest points, this yields a sparse set of seeds, e.g., approximately 25,000 seeds in the case of the ToF camera used in our experiments. Nevertheless, one of the main advantages of the ToF seeds over

the interest points is that they are regularly distributed across the images regardless of the presence/absence of texture. This is not the case with interest points whose distribution strongly depends on texture as well as lighting conditions, etc. Regularly distributed seeds will provide a better coverage of the observed scene, i.e., even in the absence of textured areas.
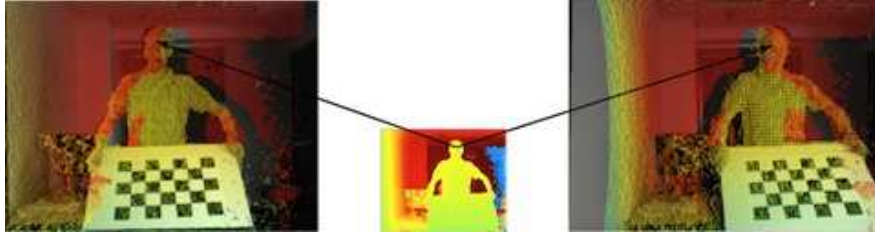

Fig. 5.2 This figure shows an example of the projection of the TOF points onto the left and right images. The projected points are color coded such that the color represents the disparity: cold colors correspond to large disparity values. Notice that there are many wrong correspondences on the computer monitor due to the screen reflectance and to artifacts along the occlusion boundaries.
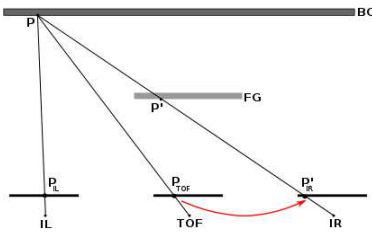

Fig. 5.3 The effect of occlusions. A TOF point P that belongs to a background (BG) objects is only observed in the left image (IL), while it is occluded by a foreground object (FG) and hence not seen in the right image (IR). When the TOF point P is projected onto the left and right images, an incorrect correspondence ($P_{IL} \leftrightarrow P'_{IR}$) is established.

However, TOF seeds are not always reliable. Some of the depth values associated with the TOF sensor are inaccurate. Moreover, whenever a TOF point is projected onto the left and onto the right images, it does not always yield a valid stereo match. There may be several sources of error which make the TOF seeds less reliable than one would have expected, as in fig. 5.2 and fig. 5.3. In detail:

1. *Imprecision due to the calibration process.* The transformations allowing to project the 3D TOF points onto the 2D images are obtained via a complex sensor calibration process, i.e., chapter 4. This introduces localization errors in the image planes of up to two pixels.
2. *Outliers due to the physical/geometric properties of the scene.* Range sensors are based on active light and on the assumption that the light beams travel from the

(a) Original set of seeds   (b) Refined set of seeds
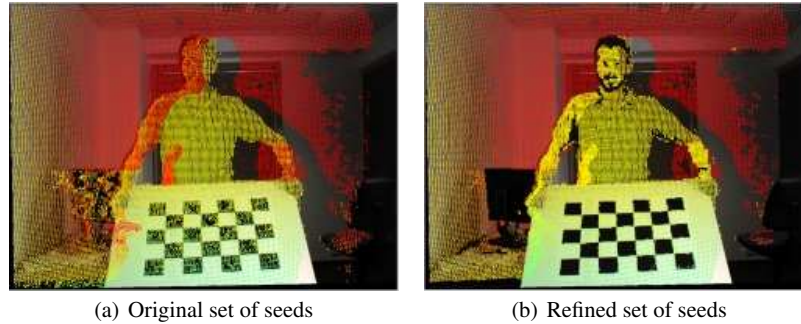
Fig. 5.4 An example of the effect of correcting the set of seeds on the basis that they should be regularly distributed.

sensor and back to it. There are a number of situations where the beam is lost, such as specular surfaces, absorbing surfaces (such as fabric), scattering surfaces (such as hair), slanted surfaces, bright surfaces (computer monitors), faraway surfaces (limited range), or when the beam travels in an unpredictable way, such a multiple reflections.

3. *The ToF camera and the 2D cameras observe the scene from slightly different points of view*. Therefore, it may occur that a 3D point that is present in the ToF data is only seen into the left or right image, as in fig. 5.3, or is not seen at all.

Therefore, a fair percentage of the ToF seeds are *outliers*. Although the seed-growing stereo matching algorithm is robust to the presence of outliers in the initial set of seeds, as already explained in section 5.2.1, we implemented a straightforward refinement step in order to detect and eliminate incorrect seed data, prior to applying alg. 1. Firstly, the seeds that lie in low-intensity (very dark) regions are discarded since the ToF data are not reliable in these cases. Secondly, in order to handle the background-to-foreground occlusion effect just outlined, we detect seeds which are not uniformly distributed across image regions. Indeed, projected 3D points lying on smooth frontoparallel surfaces form a regular image pattern of seeds, while projected 3D points that belong to a background surface and which project onto a foreground image region do not form a regular pattern, e.g., occlusion boundaries in fig. 5.4(a).

Non regular seed patterns are detected by counting the seed occupancy within small 5×5 pixel windows around every seed point in both images. If there is more than one seed point in a window, the seeds are classified as belonging to the background and hence they are discarded. A refined set of seeds is shown in fig. 5.4(b). The refinement procedure typically filters 10-15% of all seed points.

(a) Delaunay Triangulation on original seeds

(b) Delaunay Triangulation on refined seeds

(c) Prior obtained on original seeds

(d) Prior obtained on refined seeds
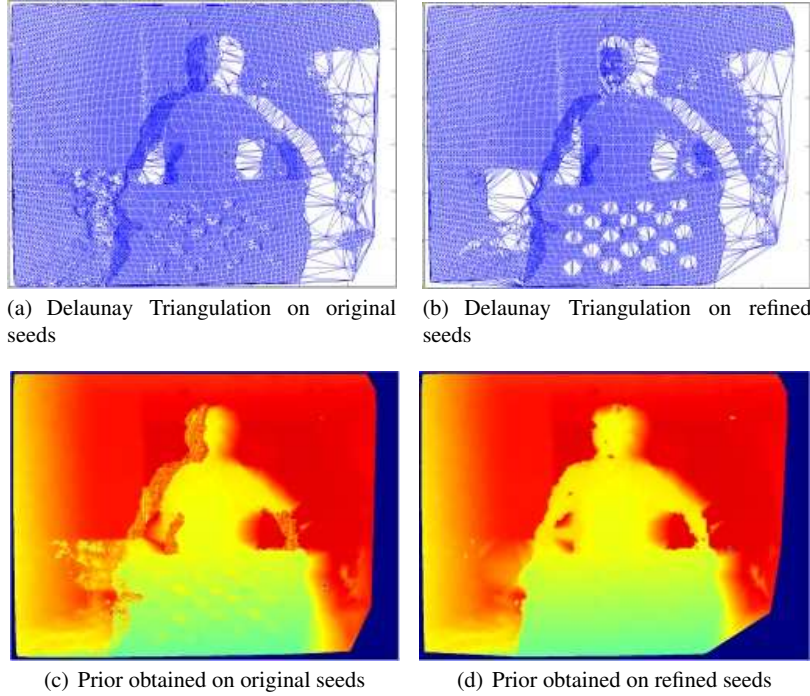
Fig. 5.5 Triangulation and prior disparity map D_p. These are shown using both raw seeds (a), (c) and refined seeds (b), (d). A positive impact of the refinement procedure is clearly visible.

5.2.3 Similarity Statistic Based on Sensor Fusion

The original seed-growing matching algorithm [14] uses Moravec's normalized cross correalation [85] (MNCC),

$$\text{simil}(s) = \text{MNCC}(w_L, w_R) = \frac{2\text{cov}(w_L, w_R)}{\text{var}(w_L) + \text{var}(w_R) + \varepsilon} \qquad (5.1)$$

as the similarity statistic to measure the photometric consistency of a correspondence $s : (u, v) \leftrightarrow (u', v)$. We denote by w_L and w_R the feature vectors which collect image intensities in small windows of size $n \times n$ pixels centered at (u, v) and $(u'v)$ in the left and right image respectively. The parameter ε prevents instability of the statistic in cases of low intensity variance. This is set as the machine floating point epsilon. The statistic has low response in textureless regions and therefore the growing algorithm does not propagate the correspondences across these regions. Since the ToF sensor can provide seeds without the presence of any texture, we propose a novel similarity statistic, $\text{simil}(s|I_L, I_R, D_p)$. This similarity measure uses a different score for photometric consistency as well as an initial high-resolution disparity map D_p, both incorporated into the Bayesian model explained in detail below.

The initial disparity map D_p is computed as follows. A 3D meshed surface is built from a 2D triangulation applied to the ToF image. The disparity map D_p is obtained via interpolation from this surface such that it has the same (high) resolution as of the left and right images. Figure 5.5(a) and 5.5(b) show the meshed surface projected onto the left high-resolution image and built from the ToF data, before and after the seed refinement step, which makes the D_p map more precise.

Let us now consider the task of finding an optimal high-resolution disparity map. For each correspondence $(u,v) \leftrightarrow (u',v)$ and associated disparity $d = u - u'$ we seek an optimal disparity d^* such that:

$$d^* = \underset{d}{\operatorname{argmax}} \, P(d|I_L,I_R,D_p). \tag{5.2}$$

By applying the Bayes' rule, neglecting constant terms, assuming that the distribution $P(d)$ is uniform in a local neighborhood where it is sought (Step. 6), and considering conditional independence $P(I_l,I_r,D|d) = P(I_L,I_R|d)P(D_p|d)$, we obtain:

$$d^* = \underset{d}{\operatorname{argmax}} \, P(I_L,I_R|d) \, P(D_p|d), \tag{5.3}$$

where the first term is the color-image likelihood and the second term is the range-sensor likelihood. We define the color-image and range-sensor likelihoods as:

$$
\begin{aligned}
P(I_L,I_R|d) &\propto \mathrm{EXPSSD}(w_L,w_R) \\
&= \exp\left(-\frac{\sum_{i=1}^{n \times n}(w_L(i) - w_R(i))^2}{\sigma_s^2 \sum_{i=1}^{n \times n}(w_L(i)^2 + w_R(i)^2)} \right),
\end{aligned}
\tag{5.4}
$$

and as:

$$P(D_p|d) \propto \exp\left(-\frac{(d - d_p)^2}{2\sigma_p^2} \right) \tag{5.5}$$

respectively, where σ_s are σ_p two normalization parameters. Therefore, the new similarity statistic becomes:

$$
\begin{aligned}
\mathrm{simil}(s|I_L,I_R,D_p) &= \mathrm{EPC}(w_L,w_R,D_p) \\
&= \exp\left(-\frac{\sum_{i=1}^{n \times n}(w_L(i) - w_R(i))^2}{\sigma_s^2 \sum_{i=1}^{n \times n}(w_L(i)^2 + w_R(i)^2)} - \frac{(d - d_p)^2}{2\sigma_p^2} \right).
\end{aligned}
\tag{5.6}
$$

Notice that the proposed image likelihood has a high response for correspondences associated with textureless regions. However, in such regions, all possible matches have similar image likelihoods. The proposed range-sensor likelihood regularizes the solution and forces it towards the one closest to the prior disparity map D_p. A tradeoff between these two terms can be obtained by tuning the parameters σ_s and σ_p. We refer to this similarity statistic as the *exponential prior correlation* (EPC) score.

5.3 Experiments

Our experimental setup comprises one Mesa Imaging SR4000 ToF camera [80] and a pair of high-resolution Point Grey[4] color cameras, as shown in fig. 5.1. The two color cameras are mounted on a rail with a baseline of about 49 cm and the ToF camera is approximately midway between them. All three optical axes are approximately parallel. The resolution of the ToF image is of 144×176 pixels and the color cameras have a resolution of 1224×1624 pixels. Recall that fig. 5.1(b) highlights the resolution differences between the ToF and color images. This camera system was calibrated using the alignment method of chapter 4.

In all our experiments, we set the parameters of the method as follows: Windows of 5×5 pixels were used for matching ($n = 5$), the matching threshold in alg. 1 is set to $\tau = 0.5$, the balance between the photometric and range sensor likelihoods is governed by two parameters in (5.6), which were set to $\sigma_s^2 = 0.1$ and to $\sigma_p^2 = 0.001$.

We show both qualitatively and quantitatively (using datasets with ground-truth) the benefits of the range sensor and an impact of particular variants of the proposed fusion model integrated in the growing algorithm. Namely, we compare results of (i) the original stereo algorithm [14] with MNCC correlation and Harris seeds (MNCC-Harris), (ii) the same algorithm with ToF seeds (MNCC-TOF), (iii) the algorithm which uses EXPSSD similarity statistic instead with both Harris (EXPSSD-Harris) and ToF seeds (EXPSSD-TOF), and (iv) the full sensor fusion model of the regularized growth (EPC). Finally small gaps of unassigned disparity in the disparity maps were filled by a primitive procedure which assigns median disparity in the 5×5 window around the gap (EPC - gaps filled). These small gaps usually occur in slanted surfaces, since alg. 1 in Step. 8 enforces one-to-one pixel matching. Nevertheless this way, they can be filled easily, if needed.

5.3.1 Real-Data Experiments

We captured two real-world datasets using the camera setup described above, SET-1 in fig. 5.6 and SET-2 in 5.7. Notice that in both of these examples the scene surfaces are weakly textured. Results shown as disparity maps are color-coded, such that warmer colors are further away from the cameras and unmatched pixels are dark blue.

In fig. 5.6(d), we can see that the original algorithm [14] has difficulties in weakly textured regions which results in large unmatched regions due to the MNCC statistic (5.1), and it produces several mismatches over repetitive structures on the background curtain, due to erroneous (mismatched) Harris seeds. In fig. 5.6(e), we can see that after replacing the sparse and somehow erratic Harris seeds with uniformly distributed (mostly correct) ToF seeds, the results have significantly been improved. There are no more mismatches on the background, but unmatched regions are still

---

[4] http://www.ptgrey.com/

(a) Left image   (b) ToF image (zoomed)   (c) Right image

(d) MNCC-Harris   (e) MNCC-TOF   (f) EXPSSD-Harris

(g) EXPSSD-TOF   (h) **EPC** (proposed)   (i) **EPC** (gaps filled)
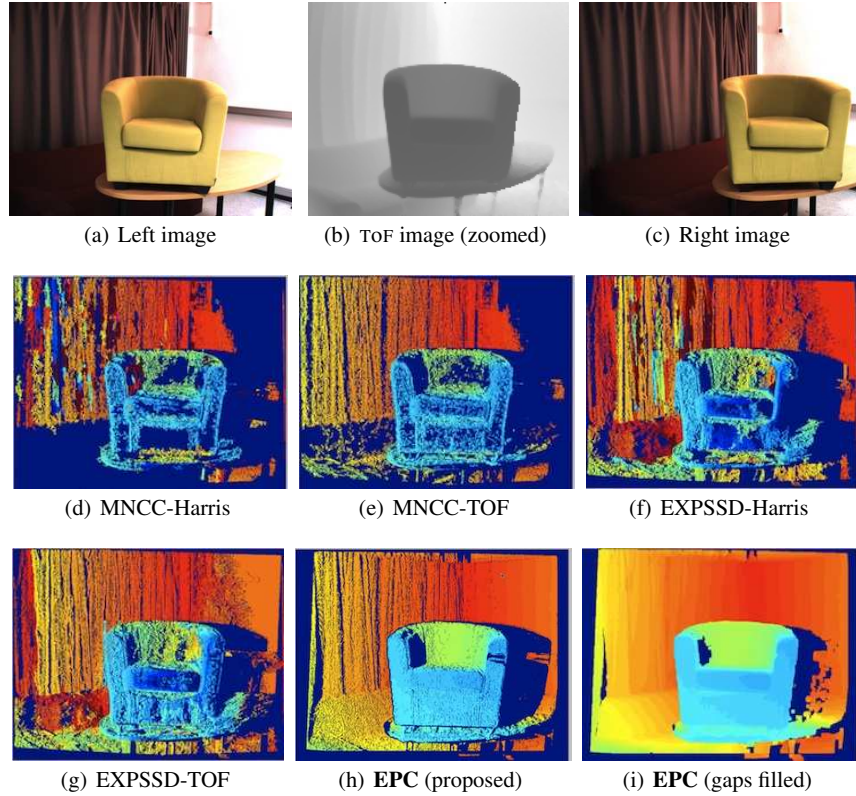
Fig. 5.6 SET-1: (a) left image, (b) ToF image and (c) right image. The ToF image has been zoomed at the resolution of the color images for visualization purposes. Results obtained (d) using the seed growing stereo algorithm [14] combining Harris seeds and MNCC statistic, (e) using ToF seeds and MNCC statistic , (f) using Harris seeds and EXPSSD statistic, (g) using ToF seeds with EXPSSD statistics. Results obtained with the proposed stereo-ToF fusion model using the EPC (exponential prior correlation) similarity statistic (h), and EPC after filling small gaps (i).

large. In fig. 5.6(f), the EXPSSD statistic (5.4) was used instead of MNCC which causes similar mismatches as in fig. 5.6(d), but unlike MNCC there are matches in textureless regions, nevertheless mostly erratic. The reason is that unlike MNCC statistic the EXPSSD statistic has high response in low textured regions. However, since all disparity candidates have equal (high) response inside such regions, the unregularized growth is random, and produces mismatches. The situation does not improve much using the ToF seeds, as shown in fig. 5.6(g). Significantly better results are finally shown in fig. 5.6(h) which uses the proposed EPC fusion model EPC from eqn. (5.6). The EPC statistic, unlike EXPSSD, has the additional regularizing range sensor likelihood term which guides the growth in ambiguous regions and attracts the solution towards the initial depth estimates of the ToF camera. Results are further refined by filling small gaps, as shown in fig. 5.6(i). Similar observations

(a) Left image   (b) ToF image (zoomed)   (c) Right image

(d) MNCC-Harris   (e) MNCC-TOF   (f) EXPSSD-Harris

(g) EXPSSD-TOF   (h) **EPC** (proposed)   (i) **EPC** (gaps filled)
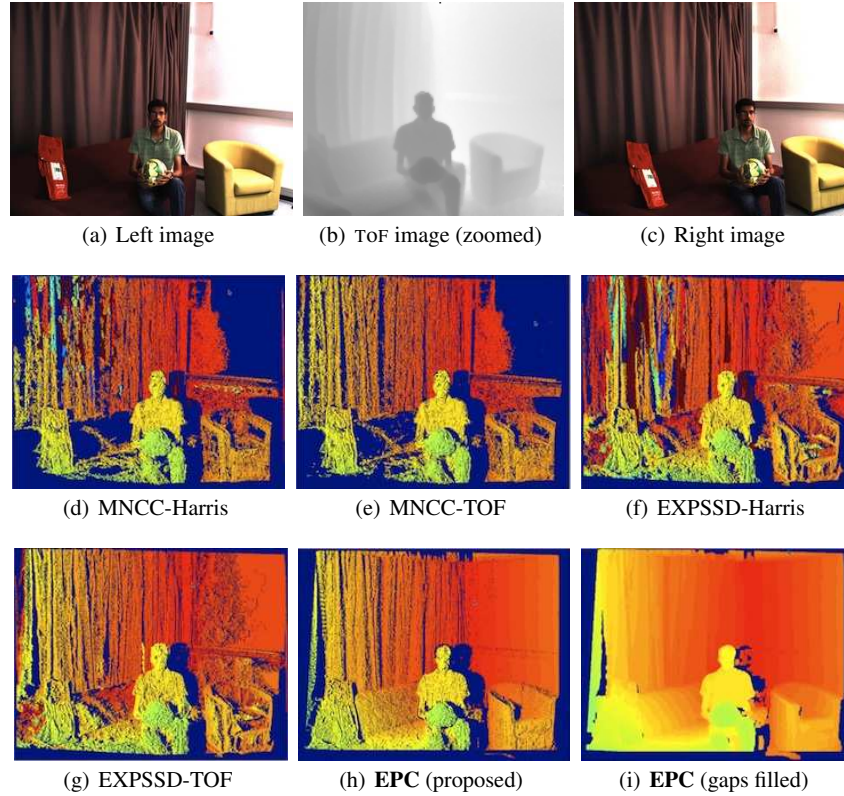
**Fig. 5.7** SET-2. Please refer to the caption of fig. 5.6 for explanations.

can be made in fig. 5.7. The proposed model clearly outperforms the other discussed approaches.

5.3.2 Comparison Between ToF Map and Estimated Disparity Map

For the proper analysis of a stereo matching algorithm it is important to inspect the reconstructed 3D surfaces. Indeed the visualization of the disparity/depth maps can sometimes be misleading. Surface reconstruction reveals fine details in the quality of the results. This is in order to qualitatively show the gain of the high-resolution depth map produced by the proposed algorithm with respect to the low-resolution depth map of the ToF sensor.

In order to provide a fair comparison, we show the reconstructed surfaces associated with the *dense* disparity maps D_p obtained after 2D triangulation of the ToF data points, fig. 5.8(a), as well as the reconstructed surfaces associated with the
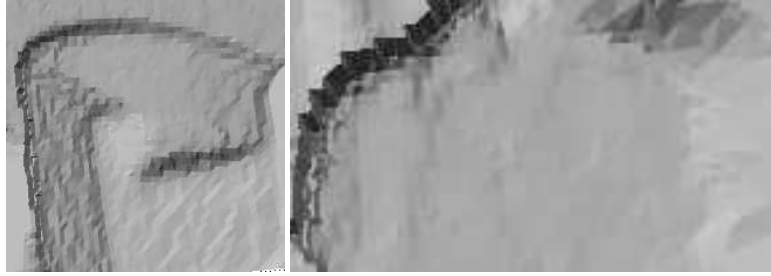
(a) Dense surface reconstruction using the disparity map D_p corresponding to a 2D triangulation of the ToF data points. Zoomed sofa chair (left) and zoomed T-shirt (right) from SET-2 in fig. 5.7(b).
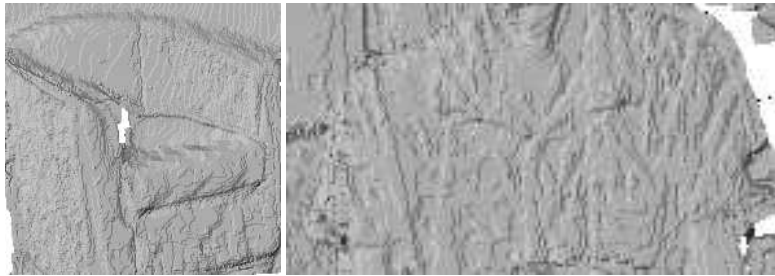
(b) Surface reconstruction using the proposed algorithm (EPC) shown on the same zoomed areas as above, i.e., fig. 5.7(i).

Fig. 5.8 The reconstructed surfaces are shown as relighted 3D meshes for (a) the prior disparity map D_p (2D triangulation on projected and refined ToF seeds), and (b) for the disparity map obtained using the proposed algorithm. Notice the fine surface details which were recovered by the proposed method.

disparity map obtained with the proposed method, fig. 5.8(b). Clearly, much more of the surface details are recovered by the proposed method. Notice precise object boundaries and fine details, like the cushion on the sofa chair and a collar of the T-shirt, which appear in fig. 5.8(b). This qualitatively corroborates the precision of the proposed method compared to the ToF data.

5.3.3 Ground-Truth Evaluation

To quantitatively demonstrate the validity of the proposed algorithm, we carried out an experiment on datasets with associated ground-truth results. Similarly to [22] we used the Middlebury dataset [99] and simulated the ToF camera by sampling the ground-truth disparity map.

The following results are based on the Middlebury-2006 dataset[5]. On purpose, we selected three challenging scenes with weakly textured surfaces: Lampshade-1, Monopoly, Plastic. The input images are of size 1330×1110 pixels. We took every 10th pixel in a regular grid to simulate the ToF camera. This gives us about 14k of ToF points, which is roughly the same ratio to color images as for the real sensors. We are aware that simulation ToF sensor this way is naive, since we do not simulate any noise or artifacts, but we believe that for validating the proposed method this is satisfactory.

Results are shown in fig. 5.9 and table 5.1. We show the left input image, results of the same algorithms as in the previous section with the real sensor, and the ground-truth disparity map. For each disparity, we compute the percentage of correctly matched pixels in non-occluded regions. This error statistic is computed as the number of pixels for which the estimated disparity differs from the ground-truth disparity by less than one pixel, divided by number of all pixels in non-occluded regions. Notice that unmatched pixels are considered as errors of the same kind as mismatches. This is in order to allow a strict but fair comparison between algorithms which deliver solutions of different densities. The quantitative evaluation confirms the previous observations regarding the real-world setup. The proposed algorithm, which uses the full sensor fusion model, significantly outperforms all other tested variants.

For the sake of completeness we also report error statistics for the prior disparity map D_p which is computed by interpolating ToF seeds, see step 1 of alg. 1. These are 92.9%, 92.1%, 96.0% for Lampshade-1, Monopoly, Plastic scene respectively. These results are already quite good, which means the interpolation we use to construct the prior disparity map is appropriate. These scenes are mostly piecewise planar, which the interpolation captures well. On the other hand, recall that in the real case, not all the seeds are correct due to various artifacts of the range data. Nevertheless in all three scenes, the proposed algorithm (EPC with gaps filled) was able to further improve the precision up to 96.4%, 95.3%, 98.2% for the respective scenes. This is again consistent with the experiments with the real ToF sensor, where higher surface details were recovered, see fig. 5.8.

Left image	MNCC-Harris	MNCC-TOF	EXPSSD-Harris	EXPSSD-TOF	EPC	EPC (gaps filled)
Lampshade-1	61.5%	64.3%	44.9%	49.5%	88.8%	96.4%
Monopoly	51.2%	53.4%	29.4%	32.1%	85.2%	95.3%
Plastic	25.2%	28.2%	13.5%	20.6%	88.7%	98.2%

Table 5.1 The error statistics (percentage of correctly matched pixels) associated with the tested algorithms and for three test image pairs from the Middlebury dataset.

---

[5] http://vision.middlebury.edu/stereo/data/scenes2006/

| Lampshade_1 | MNCC-Harris | MNCC-TOF | EXPSSD-Harris |
EXPSSD-TOF	**EPC**	**EPC** (gaps filled)	Ground-truth
Monopoly	MNCC-Harris	MNCC-TOF	EXPSSD-Harris
EXPSSD-TOF	**EPC**	**EPC** (gaps filled)	Ground-truth
Plastic	MNCC-Harris	MNCC-TOF	EXPSSD-Harris
EXPSSD-TOF	**EPC**	**EPC** (gaps filled)	Ground-truth
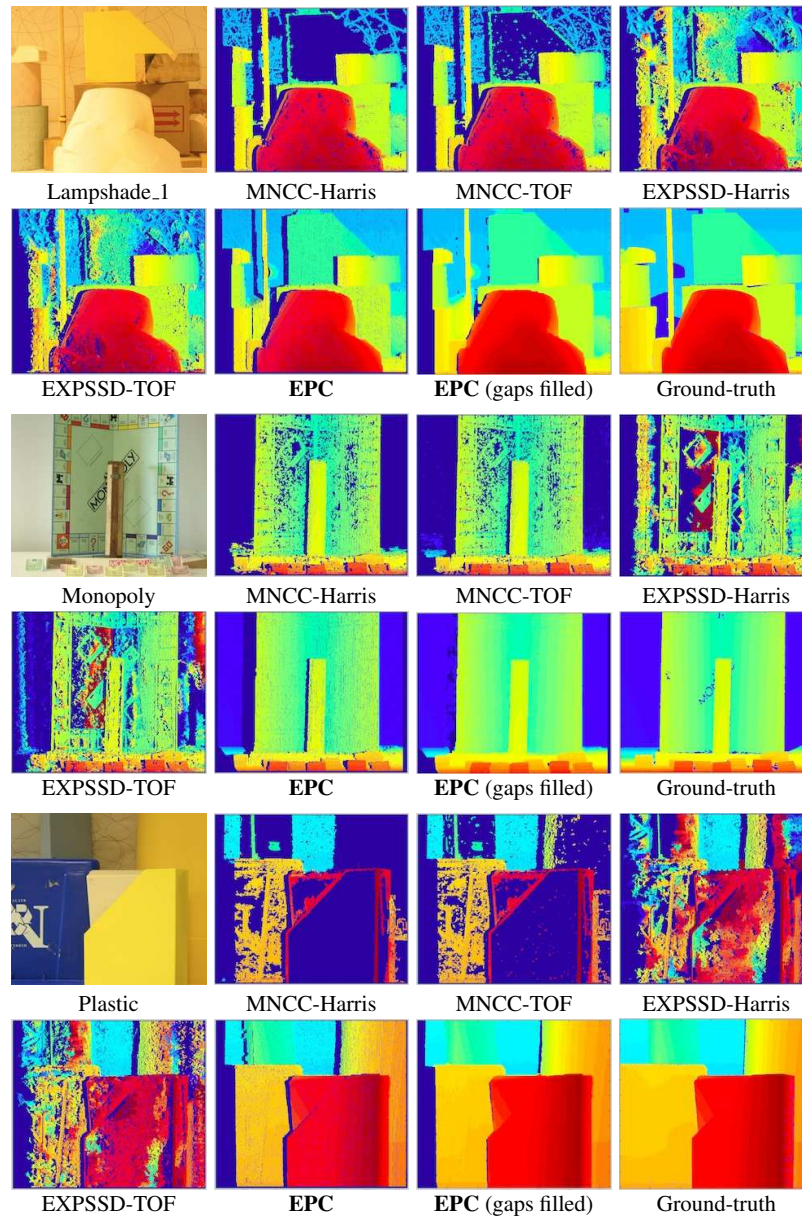
Fig. 5.9 Middlebury dataset. Left-right and top-bottom: the left images, results obtained with the same algorithms as in fig. 5.6 and 5.7, and the ground-truth disparity maps. This evaluation shows that the combination of the proposed seed-growing stereo algorithm with a prior disparity map, obtained from a sparse and regularly distributed set of 3D points, yields excellent dense matching results.

5.3.4 Computational Costs

The original growing algorithm [14] has low computational complexity due to intrinsic search space reduction. Assuming the input stereo images are of size $n \times n$ pixels, the algorithm has the complexity of $\mathcal{O}(n^2)$, while any exhaustive algorithm has the complexity at least $\mathcal{O}(n^3)$ as noted in [13]. The factor n^3 is the size of the search space in which the correspondences are sought, i.e. the disparity space. The growing algorithm does not compute similarity statistics of all possible correspondences, but efficiently traces out components of high similarity score around the seeds. This low complexity is beneficial especially for high resolution imagery, which allows precise surface reconstruction.

The proposed algorithm with all presented modifications does not represent any significant extra cost. Triangulation of ToF seeds and the prior disparity map computation is not very costly, and nor is computation of the new EPC statistic (instead of MNCC).

For our experiments, we use an "academic", i.e., a combined Matlab/C implementation which takes approximately 5 seconds on two million pixel color images. An efficient implementation of the seed-growing algorithm [14] which runs in real-time on a standard CPU was recently proposed [26]. This indicates that a real-time implementation of the proposed algorithm is feasible. Indeed, the modification of the growing algorithm and integration with the ToF data does not bring any significant extra computational costs. The algorithmic complexity remains the same, since we have only slightly modified the similarity score used inside the growing procedure. It is true that prior to the growing process, the ToF data must be triangulated. Nevertheless, this can be done extremely efficiently using computer graphics techniques and associated software libraries.

5.4 Conclusions

We have proposed a novel correspondence growing algorithm, performing fusion of a range sensor and a pair of passive color cameras, to obtain an accurate and dense 3D reconstruction of a given scene. The proposed algorithm is robust, and performs well on both textured and textureless surfaces, as well as on ambiguous repetitive patterns. The algorithm exploits the strengths of the ToF sensor and those of stereo matching between color cameras, in order to compensate for their individual weaknesses. The algorithm has shown promising results on difficult real-world data, as well as on challenging standard datasets which quantitatively corroborates its favourable properties. Together with the strong potential for real-time performance that has been discussed, the algorithm would be practically very useful in many computer vision and robotic applications.

References

1. G. Alenyà, B. Dellen, and C. Torras. 3d modelling of leaves from color and tof data for robotized plant measuring. In *Proc. ICRA*, pages 3408–3414, 2011.
2. M. Attamimi, A. Mizutani, T. Nakamura, T. Nagai, K. Funakoshi, and M. Nakano. Real-time 3D visual sensor for robust object recognition. In *IROS*, pages 4560–4565, 2010.
3. B. Bartczak and R. Koch. Dense depth maps from low resolution time-of-flight depth and high resolution color views. In *Proc. Int. Symp. on Visual Computing (ISVC)*, pages 228–239, 2009.
4. C. Beder, B. Bartczak, and R. Koch. A comparison of PMD-cameras and stereo-vision for the task of surface reconstruction using patchlets. In *Proc. CVPR*, pages 1–8, 2007.
5. C. Beder, I. Schiller, and R. Koch. Photoconsistent relative pose estimation between a PMD 2D3D-camera and multiple intensity cameras. In *Proc. Symp. of the German Association for Pattern Recognition (DAGM)*, pages 264–273, 2008.
6. J. Bilmes. A Gentle Tutorial of the EM Algorithm and its Application to Parameter Estimation for Gaussian Mixture and Hidden Markov Models. Technical Report TR-97-021, U.C. Berkeley, 1998.
7. A. Bleiweiss and M. Werman. Fusing time-of-flight depth and color for real-time segmentation and tracking. In *Proc. DAGM Workshop on Dynamic 3D Imaging*, pages 58–69, 2009.
8. Y. Boykov, O. Veksler, and R. Zabih. Fast approximate energy minimization via graph cuts. *IEEE Trans. PAMI*, 23(11):1222–1239, 2001.
9. G. Bradski and A. Kaehler. *Learning OpenCV*. O'Reilly, 2008.
10. V. Castañeda, D. Mateus, and N. Navab. SLAM combining ToF and high-resolution cameras. In *IEEE Workshkop on Motion and Video Computing*, 2011.
11. V. Castañeda, D. Mateus, and N. Navab. Stereo time-of-flight. In *Proc. ICCV*, pages 1684–1691, 2011.
12. J. Cech, J. Matas, and M. Perdoch. Efficient sequential correspondence selection by cosegmentation. *IEEE Trans. PAMI*, 32(9):1568–1581, 2010.
13. J. Cech, J. Sanchez-Riera, and R. Horaud. Scene flow estimation by growing correspondence seeds. In *Proc. CVPR*, pages 3129–3136, 2011.
14. J. Čech and R. Šára. Efficient sampling of disparity space for fast and accurate matching. In *In Proc. BenCOS Workshop, CVPR*, 2007.
15. D. Chan, H. Buisman, C. Theobalt, and S. Thrun. A noise-aware filter for real-time depth upsampling. In *ECCV Workshop on Multi-camera and Multi-modal Sensor Fusion Algorithms and Applications*, 2008.
16. T. Chen, H. P. A. Lensch, C. Fuchs, and H. P. Seidel. Polarization and phase-shifting for 3D scanning of translucent objects. *Proc. CVPR*, pages 1–8, 2007.
17. O. Choi and S. Lee. Wide range stereo time-of-flight camera. In *Proc. ICIP*, 2012.
18. O. Choi, H. Lim, B. Kang, Y. Kim, K. Lee, J. Kim, and C. Kim. Range unfolding for time-of-flight depth cameras. *Proc. ICIP*, pages 4189–4192, 2010.

19. A. Criminisi, P. Perez, and K. Toyama. Region filling and object removal by exemplar-based image inpainting. *IEEE Trans. Image Processing*, 13(9):1200–1212, 2004.

20. G. Csurka, D. Demirdjian, and R. Horaud. Finding the collineation between two projective reconstructions. *Computer Vision and Image Understanding*, 75(3):260–268, 1999.

21. B. Curless and M. Levoy. A volumetric method for building complex models from range images. *Proc. SIGGRAPH '96*, pages 303–312, 1996.

22. C. Dal Mutto, P. Zanuttigh, and G. M. Cortelazzo. A probabilistic approach to ToF and stereo data fusion. In *3DPVT*, May 2010.

23. A. Datta, K. Jun-Sik, and T. Kanade. Accurate camera calibration using iterative refinement of control points. In *Workshop on Visual Surveillance, Proc. ICCV 2009*, pages 1201–1208, 2009.

24. A. de la Escalera and J. Armingol. Automatic Chessboard Detection for Intrinsic and Extrinsic Camera Parameter Calibration. *Sensors*, 10:2027–2044, 2010.

25. J. Diebel and S. Thrun. An application of Markov random fields to range sensing. In *Proc. NIPS*, 2005.

26. M. Dobias and R. Sára. Real-time global prediction for temporally stable stereo. In *Proc. ICCV Workshops*, pages 704–707, 2011.

27. J. Dolson, J. Baek, C. Plagemann, and S. Thrun. Fusion of time-of-flight depth and stereo for high accuracy depth maps. *Proc. CVPR*, pages 1–8, 2008.

28. J. Dolson, J. Baek, C. Plagemann, and S. Thrun. Upsampling range data in dynamic environments. *Proc. CVPR*, pages 1141–1148, 2010.

29. D. Droeschel, D. Holz, and S. Behnke. Multifrequency phase unwrapping for time-of-flight cameras. In *IEEE/RSJ International Conference on Intelligent Robots and Systems*, 2010.

30. D. Droeschel, D. Holz, and S. Behnke. Probabilistic phase unwrapping for time-of-flight cameras. In *Joint 41st International Symposium on Robotics and 6th German Conference on Robotics*, 2010.

31. D. Droeschel, J. Stückler, D. Holz, and S. Behnke. Towards joint attention for a domestic service robot - person awareness and gesture recognition using time-of-flight cameras. In *Proc. ICRA*, pages 1205–1210, 2011.

32. H. Du, T. Oggier, F. Lustenberger, and E. Charbon. A virtual keyboard based on true-3d optical ranging. In *Proc. BMVC'05*, pages 220–229, 2005.

33. J. M. Dubois and H. Hügli. Fusion of time-of-flight camera point clouds. In *ECCV Workshop on Multi-Camera and Multi-modal Sensor Fusion Algorithms and Applications*, 2008.

34. T. Edeler, K. Ohliger, S. Hussmann, and A. Mertins. Time-of-flight depth image denoising using prior noise information. *ICSP*, pages 119–122, 2010.

35. D. Fălie and V. Buzuloiu. Wide range time of flight camera for outdoor surveillance. In *Microwaves, Radar and Remote Sensing Symposium*, 2008.

36. J. Fischer, G. Arbeiter, and A. Verl. Combination of time-of-flight depth and stereo using semiglobal optimization. In *Proc. ICRA*, pages 3548–3553, 2011.

37. S. Foix, G. Alenya, and C. Torras. Lock-in time-of-flight (ToF) cameras: A survey. *IEEE Sensors Journal*, 11(9):1917–1926, 2011.

38. W. Förstner. Uncertainty and projective geometry. In E. Bayro-Corrochano, editor, *Handbook of Geometric Computing*, pages 493–534. Springer, 2005.

39. B. Freedman, A. Shpunt, M. Machline, and Y. Arieli. Depth mapping using projected patterns, 2012.

40. B. J. Frey, R. Koetter, and N. Petrovic. Very loopy belief propagation for unwrapping phase images. In *Advances in Neural Information Processing Systems*, 2001.

41. S. Fuchs. Multipath interference compensation in time-of-flight camera images. In *Proc. ICPR*, pages 3583–3586, 2010.

42. S. Fuchs and G. Hirzinger. Extrinsic and depth calibration of ToF-cameras. *Proc. CVPR*, pages 1–6, 2008.

43. A. Geiger, M. Roser, and R. Urtasun. Efficient large-scale stereo matching. In *Proc. ACCV*, pages 25–38, 2010.

44. D. C. Ghiglia and L. A. Romero. Robust two-dimensional weighted and unweighted phase unwrapping that uses fast transforms and iterative methods. *Journal of Optical Society of America A*, 11(1):107–117, 1994.

45. S. B. Göktürk, H. Yalcin, and C. Bamji. A time-of-flight depth sensor—system description, issues and solutions. In *Proc. CVPR Workshops*, 2004.

46. R. M. Goldstein, H. A. Zebker, and C. L. Werner. Satellite radar interferometry: two-dimensional phase unwrapping. *Radio Science*, 23:713–720, 1988.

47. D. Gonzalez-Aguilera, J. Gomez-Lahoz, and P. Rodriguez-Gonzalvez. An automatic approach for radial lens distortion correction from a single image. *IEEE Sensors*, 11(4):956–965, 2011.

48. S. Gould, P. Baumstarck, M. Quigley, A. Y. Ng, and D. Koller. Integrating visual and range data for robotic object detection. In *Proc. ECCV Workshops*, 2008.

49. G. Granlund. In search of a general picture processing operator. *Computer Graphics and Image Processing*, 8:155–173, 1978.

50. M. Gupta, A. Agrawal, A. Veeraraghavan, and S. G. Narasimhan. Structured light 3d scanning under global illumination. *Proc. CVPR*, 2011.

51. U. Hahne and M. Alexa. Depth imaging by combining time-of-flight and on-demand stereo. In *Proc. DAGM Workshop on Dynamic 3D Imaging*, pages 70–83, 2009.

52. M. Hansard, R. Horaud, M. Amat, and S. Lee. Projective Alignment of Range and Parallax Data. In *Proc. CVPR*, pages 3089–3096, 2011.

53. C. Harris and M. Stephens. A combined corner and edge detector. In *Proc. 4th Alvey Vision Conference*, pages 147–151, 1988.

54. R. Hartley and P. Sturm. Triangulation. *Computer Vision and Image Understanding*, 68(2):146–157, 1997.

55. R. Hartley and A. Zisserman. *Multiple View Geometry in Computer Vision*. Cambridge University Press, 2000.

56. M. Hebert and E. Krotkov. 3D measurements from imaging laser radars: How good are they? *Image and Vision Computing*, 10(3):170–178, 1992.

57. P. Henry, M. Krainin, E. Herbst, X. Ren, and D. Fox. Rgbd mapping: Using depth cameras for dense 3d modeling of indoor environments. *In RGB-D: Advanced Reasoning with Depth Cameras Workshop in conjunction with RSS*, 2010.

58. B. Horn, H. Hilden, and S. Negahdaripour. Closed-form solution of absolute orientation using orthonormal matrices. *J. Optical Society of America A*, 5(7):1127–1135, 1988.

59. B. Huhle, S. Fleck, and A. Schilling. Integrating 3D time-of-flight camera data and high resolution images for 3DTV applications. In *Proc. 3DTV*, pages 1–4, 2007.

60. B. Huhle, T. Schairer, P. Jenke, and W. Strasser. Robust non-local denoising of colored depth data. *Proc. CVPR Workshops*, pages 1–7, 2008.

61. S. Hussmann, A. Hermanski, and T. Edeler. Real-time motion artifact suppression in tof camera systems. *IEEE Trans. on Instrumentation and Measurement*, 60(5):1682–1690, 2011.

62. J. Illingworth and J. Kittler. A survey of the Hough transform. *Computer Vision, Graphics and Image Processing*, 44:87–116, 1988.

63. C. Jakowatz Jr., D. Wahl, P. Eichel, D. Ghiglia, and P. Thompson. *Spotlight-mode Synthetic Aperture Radar: A signal processing approach*. Kluwer Academic Publishers, Boston, MA, 1996.

64. I. Jebari, S. Bazeille, E. Battesti, H. Tekaya, M. Klein, A. Tapus, D. Filliat, C. Meyer, Sio-Hoi, Ieng, R. Benosman, E. Cizeron, J.-C. Mamanna, and B. Pothier. Multi-sensor semantic mapping and exploration of indoor environments. In *TePRA*, pages 151 –156, 2011.

65. B. Jutzi. Investigation on ambiguity unwrapping of range images. In *International Archives of Photogrammetry and Remote Sensing Workshop on Laserscanning*, 2009.

66. Y. Kanazawa and K. Kanatani. Reliability of Plane Fitting by Range Sensing. In *Proc. ICRA*, pages 2037–2042, 1995.

67. B. Kang, S. Kim, S. Lee, K. Lee, J. Kim, and C. Kim. Harmonic distortion free distance estimation in tof camera. In *SPIE EI*, 2011.

68. K. Khoshelham. Accuracy analysis of kinect depth data. *Proc. ISPRS Workshop on Laser Scanning*, 2011.

69. Y. Kim, D. Chan, C. Theobalt, and S. Thrun. Design and calibration of a multi-view TOF sensor fusion system. In *Proc. CVPR Workshop on time-of-flight Camera based Computer Vision*, 2008.

70. R. Koch, I. Schiller, B. Bartczak, F. Kellner, and K. Köser. MixIn3D: 3D mixed reality with ToF-camera. In *Proc. DAGM Workshop on dynamic 3D imaging*, pages 126–141, 2009.

71. A. Kolb, E. Barth, R. Koch, and R. Larsen. Time-of-flight cameras in computer graphics. *Computer Graphics Forum*, 29(1):141–159, 2010.

72. L. Krüger, C. Wöhler, A. Würz-Wessel, and F. Stein. In-factory calibration of multiocular camera systems. In *SPIE Photonics Europe*, pages 126–137, 2004.

73. S. Lee, B. Kang, J. D. K. Kim, and C.-Y. Kim. Motion blur-free time-of-flight range sensor. In *Proc. SPIE EI*, 2012.

74. S. Lee, H. Shim, J. D. K. Kim, and C.-Y. Kim. Tof depth image motion blur detection using 3d blur shape models. In *Proc. SPIE EI*, 2012.

75. Z. Liang and P. Lauterbur. *Principles of Magnetic Resonance Imaging: A Signal Processing Perspective*. Wiley-IEEE Press, 1999.

76. M. Lindner and A. Kolb. Compensation of motion artifacts for time-of-flight cameras. In *Dynamic 3D Imaging*, volume 5742 of *Lecture Notes in Computer Science*, pages 16–27. Springer, 2009.

77. M. Lindner, A. Kolb, and T. Ringbeck. New insights into the calibration of tof-sensors. *Proc. CVPR Workshops*, pages 1–5, 2008.

78. M. Lindner, I. Schiller, A. Kolb, and R. Koch. Time-of-flight sensor calibration for accurate range sensing . *Computer Vision and Image Understanding*, 114(12):1318–1328, 2010.

79. O. Lottner, A. Sluiter, K. Hartmann, and W. Weihs. Movement artefacts in range images of time-of-flight cameras. In *International Symposium on Signals, Circuits and Systems (ISSCS)*, volume 1, pages 1–4, 2007.

80. Mesa Imaging AG. `http://www.mesa-imaging.ch`.

81. S. Matyunin, D. Vatolin, Y. Berdnikov, and M. Smirnov. Temporal filtering for depth maps generated by kinect depth camera. *Proc. 3DTV*, pages 1–4, 2011.

82. S. May, B. Werner, H. Surmann, and K. Pervolz. 3d time-of-flight cameras for mobile robotics. In *Proc. IEEE/RSJ Conf. on Intelligent Robots and Systems*, pages 790–795, 2006.

83. S. H. McClure, M. J. Cree, A. A. Dorrington, and A. D. Payne. Resolving depth-measurement ambiguity with commercially available range imaging cameras. In *Image Processing: Machine Vision Applications III*, 2010.

84. F. Meyer. Topographic distance and watershed lines. *Signal Processing*, 38(1):113–125, 1994.

85. H. P. Moravec. Toward automatic visual obstacle avoidance. In *ICAI*, pages 584–94, 1977.

86. J. Mure-Dubois and H. Hugli. Real-time scattering compensation for time-of-flight camera. In *CVS*, 2007.

87. R. A. Newcombe and A. J. Davison. Live dense reconstruction with a single moving camera. In *Proc. CVPR*, pages 1498–1505, 2010.

88. R. A. Newcombe, S. Izadi, O. Hilliges, D. Molyneaux, D. Kim, A. J. Davison, P. Kohli, J. Shotton, S. Hodges, and A. Fitzgibbon. Kinectfusion: Real-time dense surface mapping and tracking. *IEEE ISMAR*, pages 1–8, 2011.

89. Ş. Oprişescu, D. Fălie, M. Ciuc, and V. Buzuloiu. Measurements with ToF cameras and their necessary corrections. In *IEEE International Symposium on Signals, Circuits & Systems*, 2007.

90. J. Park, H. Kim, Y.-W. Tai, M.-S. Brown, and I. S. Kweon. High quality depth map upsampling for 3D-TOF cameras. In *Proc. ICCV*, 2011.

91. K. Pathak, N. Vaskevicius, and A. Birk. Revisiting uncertainty analysis for optimum planes extracted from 3D range sensor point-clouds. In *Proc. ICRA*, pages 1631–1636, 2009.

92. A. D. Payne, A. P. P. Jongenelen, A. A. Dorrington, M. J. Cree, and D. A. Carnegie. Multiple frequency range imaging to remove measurment ambiguity. In *9th Conference on Optical 3-D Measurement Techniques*, 2009.

93. J. Poppinga and A. Birk. A novel approach to efficient error correction for the swissranger time-of-flight 3d camera. In *RoboCup 2008: Robot Soccer World Cup XII*, 2008.

94. W. H. Press, S. A. Teukolsky, W. T. Vetterling, and B. P. Flannery. *Numerical Recipes in C*. Cambridge University Press, 2nd edition, 1992.

95. M. Reynolds, J. Dobos, L. Peel, T. Weyrich, and G. Brostow. Capturing time-of-flight data with confidence. In *Proc. CVPR*, pages 945–952, 2011.

96. C. Rother, V. Kolmogorov, and A. Blake. "GrabCut"—interactive foreground extraction using iterated graph cuts. In *International Conference and Exhibition on Computer Graphics and Interactive Techniques*, 2004.

97. F. Ryden, H. Chizeck, S. N. Kosari, H. King, and B. Hannaford. Using kinect and a haptic interface for implementation of real-time virtual fixtures. *In RGB-D: Advanced Reasoning with Depth Cameras Workshop in conjunction with RSS*, 2010.

98. T. Schamm, M. Strand, T. Gumpp, R. Kohlhaas, J. Zollner, and R. Dillmann. Vision and tof-based driving assistance for a personal transporter. In *Proc. ICAR 2009*, pages 1–6, 2009.

99. D. Scharstein and R. Szeliski. A taxonomy and evaluation of dense two-frame stereo correspondence algorithms. *International Journal of Computer Vision*, 47:7–42, 2002.

100. D. Scharstein and R. Szeliski. High-accuracy stereo depth maps using structured light. *Proc. CVPR*, 2003.

101. I. Schiller, C. Beder, and R. Koch. Calibration of a PMD camera using a planar calibration object together with a multi-camera setup. In *Int. Arch. Soc. Photogrammetry, Remote Sensing and Spatial Information Sciences XXI*, pages 297–302, 2008.

102. S. Schuon, C. Theobalt, J. Davis, and S. Thrun. High-quality scanning using time-of-flight depth superresolution. *Proc. CVPR Workshops*, pages 1–7, 2008.

103. S. Seitz, B. Curless, J. Diebel, D. Scharstein, and R. Szeliski. A comparison and evaluation of multi-view stereo reconstruction algorithms. *Proc. CVPR*, pages 519–528, 2006.

104. H. Shim, R. Adels, J. Kim, S. Rhee, T. Rhee, C. Kim, J. Sim, and M. Gross. Time-of-flight sensor and color camera calibration for multi-view acquisition. *The Visual Computer*, 2011.

105. J. Shotton, A. Fitzgibbon, M. Cook, and A. Blake. Real-time human pose recognition in parts from single depth images. *Proc. CVPR*, 2011.

106. J. Smisek, M. Jancosek, and T. Pajdla. 3d with kinect. In *Proc. ICCV Workshops*, pages 1154–1160, 2011.

107. S. Soutschek, J. Penne, J. Hornegger, and J. Kornhuber. 3-d gesture-based scene navigation in medical imaging applications using time-of-flight cameras. In *Proc. CVPR 2008 Workshops*, pages 1–6, 2008.

108. J. Stückler and S. Behnke. Combining depth and color cues for scale- and viewpoint-invariant object segmentation and recognition using random forests. In *Proc. IROS*, pages 4566–4571, 2010.

109. Y.-W. Tai, N. Kong, S. Lin, and S. Y. Shin. Coded exposure imaging for projective motion deblurring. In *Proc. CVPR*, pages 2408–2415, 2010.

110. T. Tuytelaars, M. Proesmans, and L. V. Gool. The Cascaded Hough Transform as Support for Grouping and Finding Vanishing Points and Lines. In *Proc. International Workshop on Algebraic Frames for the Perception-Action Cycle*, pages 278–289, 1997.

111. A. Verri and V. Torre. Absolute depth estimate in stereopsis. *J. Optical Society of America A*, 3(3):297–299, 1986.

112. C. Wang, H. Tanahasi, H. Hirayu, Y. Niwa, and K. Yamamoto. Comparison of local plane fitting methods for range data. In *Proc. CVPR*, pages 663–669, 2001.

113. L. Wang and R. Yang. Global stereo matching leveraged by sparse ground control points. In *Proc. CVPR*, pages 3033–3040, 2011.

114. Z. Wang, W. Wu, X. Xu, and D. Xue. Recognition and location of the internal corners of planar checkerboard calibration pattern image. *Applied Mathematics and Computation*, 185(2):894–906, 2007.

115. O. Whyte, J. Sivic, A. Zisserman, and J. Ponce. Non-uniform deblurring for shaken images. In *Proc. CVPR*, pages 491–498, 2010.

116. J. Wu, Y. Zhou, H. Yu, and Z. Zhang. Improved 3D depth image estimation algorithm for visual camera. In *Proc. International Congress on Image and Signal Processing*, 2009.

117. Q. Yang, R. Yang, J. Davis, and D. Nister. Spatial-depth super resolution for range images. *Proc. CVPR*, pages 1–8, 2007.

118. D. Yeo, E. ul Haq, J. Kim, M. Baig, and H. Shin. Adaptive bilateral filtering for noise removal in depth upsampling. *ISOCC*, pages 36–39, 2011.

119. F. Yuan, A. Swadzba, R. Philippsen, O. Engin, M. Hanheide, and S. Wachsmuth. Laser-based navigation enhanced with 3d time-of-flight data. In *Proce ICRA '09*, pages 2844–2850, 2009.

120. H. Zeng, X. Deng, and Z. Hu. A new normalized method on line-based homography estimation. *Pattern Recognition Letters*, 29:1236–1244, 2008.

121. L. Zhang, A. Deshpande, and X. Chen. Denoising vs. deblurring: Hdr imaging techniques using moving cameras. In *Proc. CVPR*, pages 522–529, 2010.

122. Q. Zhang and R. Pless. Extrinsic calibration of a camera and laser range finder (improves camera calibration). In *Proc. Int. Conf. on Intelligent Robots and Systems*, pages 2301–2306, 2004.

123. Z. Zhang. Flexible camera calibration by viewing a plane from unknown orientations. *Proc. ICCV*, 1999.

124. Z. Zhang. A flexible new technique for camera calibration. *IEEE Trans. PAMI*, 22(11):1330–1334, 2000.

125. J. Zhu, L. Wang, R. G. Yang, and J. Davis. Fusion of time-of-flight depth and stereo for high accuracy depth maps. In *Proc. CVPR*, pages 1–8, 2008.